On the Climate Dependence of Subgrid-Scale Parameterizations

Dissertation
zur Erlangung des Doktorgrades
der Naturwissenschaften

vorgelegt beim Fachbereich Geowissenschaften / Geographie
der Johann Wolfgang Goethe-Universität
in Frankfurt am Main

von

Martin Pieroth
aus Bensheim

Frankfurt 2019

D 30

vom Fachbereich Geowissenschaften / Geographie der

Johann Wolfgang Goethe-Universität als Dissertation angenommen.

Dekan:	Prof. Dr. Georg Rümpker
Gutachter:	Prof. Dr. Ulrich Achatz Institut für Atmosphäre und Umwelt Johann Wolfgang Goethe-Universität Frankfurt am Main
	Prof. Dr. Andrey Gritsun Institute of Numerical Mathematics Russian Academy of Sciences Moskau

Datum der Disputation:

Zusammenfassung

Wetter- und Klimamodelle enthalten viele Subgitterskalen (SGS-) Parametrisierungen. Diese beschreiben Prozesse, welche nicht explizit durch die Modelle berechnet werden können. Dennoch spielen die SGS-Prozesse eine große Rolle für die von den Modellen aufgelöste Strömung. Dabei sind SGS-Schließungen keine geschlossenen Gleichungen, sondern enthalten üblicherweise Parameter, deren Werte nicht durch theoretische Überlegungen bestimmt werden können. So sind beispielsweise die Aerosolverteilung, die Wurzellänge in Bodenmodellen oder die Quellschicht (engl.: *launch level*) von parametrisierten Schwerewellen freie Parameter.

Zur Bestimmung dieser empirischen Parameter werden Daten aus Beobachtungen oder hochauflösenden Modellläufen genutzt. Anhand dieser Daten werden die Parameter angepasst (d.h. getunt), sodass das Modell mit der entsprechenden SGS-Schließung die Referenz möglichst genau reproduziert. Dabei spielt das Tuning in der Modellentwicklung eine entscheidende Rolle. Erst die Anpassung der empirischen Parameter ermöglicht es den nationalen Wetterdiensten regelmäßig qualitativ hochwertige Wettervorhersagen zu treffen. Andererseits birgt das Tuning auch ein Problem, beispielsweise bei Klimaprojektionen. Die Parameter sind auf das beobachtete Klima eingestellt. Es ist aber nicht zwangsläufig gegeben, dass zukünftige oder vergangene Klimata mit dem gleichen Satz Parameter bestmöglich beschrieben werden können.

Vor diesem Hintergrund werden in der vorliegenden Dissertation zwei Fragestellungen behandelt:

1. Ist es möglich eine Klimaabhängigkeit in den Tuningparameter von SGS-Schließungen einzuführen?
2. Können Parametrisierungen entwickelt werden, welche gegenüber einem gestörten Klima robust sind?

Der erste Teil der Dissertation beschäftigt sich mit Tuningparametern in SGS-Schließungen. Dabei wird das Fluktuations-Dissipations Theorem (FDT) genutzt, um eine Klimaabhängigkeit in empirischen Parametern einzuführen. Das FDT basiert auf einer linearen Theorie, welche die Fluktuationen eines Systems um dessen statistischen stationären Zustand (engl.: *steady state*) mit dem Verhalten bei kleiner äußeren Störung (dem Response) in Verbindung setzt. Dies ermöglicht es, die Änderung der Statistik des betrachteten Systems bei gegebenem anomalen Antrieb abzuschätzen. Falls die empirischen Parameter derart getunt wurden, dass diese mathematisch rigoros von der Statistik des Systems abhängen, so kann die Abschätzung des FDTs verwendet werden, um die Tuningparameter an den Antrieb anzupassen. Hierzu wird die einfachste Form des FDT, das sogenannte quasi-Gaußsche FDT (qG-FDT), verwendet.

Der Ansatz wurde in einem quasigeostrophischen Dreischichtenmodell (QG3LM) untersucht, welches als Referenz für die numerischen Experimente dient. Daneben wurde ein semiempirisches Modell (SEM) konstruiert, basierend auf den führenden Varianzmustern [empirische orthogonale Funktionen (EOFs)] des QG3LM. Zudem enthält das SEM eine rein datengetriebene SGS-Parametrisierung, gegeben durch entweder eine einfache lineare Funktion ($\mathrm{SEM_{det}}$) oder einen Ornstein-Uhlenbeck Prozess (OU-Prozess; $\mathrm{SEM_{stoch}}$). Beide Parametrisierungen wurden objektiv durch Minimierung des Residuumfehlers bzw. Anwendung der Maximum-Likelihood Methode getunt. Als externer Antrieb wurde eine lokale Heizung in den mittleren Breiten sowie ein globaler Antrieb, repräsentiert durch je eine der fünf führenden EOFs, betrachtet. Während im ungestörten Fall beide SEMs sowohl qualitativ als auch quantitativ das QG3LM reproduzieren, so zeigen sie einen falschen Response auf die externen Antriebe. Dieser Fehler konnte direkt auf ein inkorrektes Tuning zurückgeführt werden.

Für beide externe Antriebe ist das qG-FDT in der Lage die Änderungen der ersten und zweiten statistischen Momente abzuschätzen. Erwartungsgemäß zeigten hierbei die zweiten Momente einen systematisch höheren Fehler. Um die Nützlichkeit der qG-FDT-Abschätzungen zu bewerten, wurde der Response von drei Modellen untersucht: das a priori SEM (apr-SEM; unveränderte Schließung), das a posteriori SEM (apo-SEM; perfekt getunte Parametrisierung) und das qG-FDT SEM (FDT-SEM; Schließungsparameter mittels des qG-FDT aktualisiert). Dabei kann das apr-SEM als die gängige Praxis von Klimaprojektionen angesehen werden, in der das Modell zwar gestört, aber die Tuningparameter normalerweise nicht angepasst werden.

Die Modelle wurden mit Hinblick auf den Response im Mittelwert und Kovarianz der Stromfunktion untersucht. Dabei zeigte sich ein ähnliches Bild für beide

Antriebsterme und Schließungen. Generell wies das FDT-SEM eine systematisch bessere Übereinstimmung mit dem QG3LM auf als das apr-SEM. Jedoch lieferten alle SEMs mit EOF-Abbrüchen kleiner 200 EOFs für den Response der Kovarianz keine brauchbaren Ergebnisse (der relative Amplitudenfehler lag bei allen Modellen über 100%). In diesen Fällen reichten die einfachen Parametrisierungen nicht aus, um die SGS-Prozesse ausreichend zu beschreiben. Andererseits ist das FDT-SEM, aufgrund der Kombination der linearen qG-FDT-Abschätzung mit dem nichtlinearen SEM, für hinreichend große EOF-Abbrüche in der Lage die direkte Anwendung des qG-FDT-Response-Operators zu schlagen. Dies ermöglicht dem FDT-SEM eine Abschätzung des Responses im Mittelwert und Kovarianz der Stromfunktion, selbst wenn der Response nichtlinear ist.

Neben den Anomalieexperimenten wurde auch die Annahme der Gaußität im qG-FDT untersucht, durch Verwendung des genaueren Short-Time/qG-FDT (ST/qG-FDT-) Algorithmus. Dieser umgeht die Annahme einer gaußverteilten Wahrscheinlichkeitsdichtefunktion und liefert daher grundsätzlich präziserere Abschätzungen als das qG-FDT. Allerdings zeigt sich in der Abschätzung des Responses der statistischen Momente keine signifikante Verbesserung gegenüber dem qG-FDT. Daher scheint das vergleichsweise einfache qG-FDT auszureichen, um Tuningparameter sinnvoll an externe Antriebe anzupassen.

Der zweite Teil der Dissertation beschäftigt sich mit SGS-Parametrisierungen basierend auf ersten Prinzipien. Eine solche Schließung sollte allein von den Modellvariablen und –gleichungen abhängen und wenig bis keine Tuningparameter beinhalten. Hierfür wurde die Methode der stochastischen Modenreduktion (SMR) untersucht, welche die Konstruktion einer, weitestgehend auf ersten Prinzipien basierenden, Parametrisierung ermöglicht. Die SMR geht davon aus, dass der Zustandsvektor des Systems in eine langsame und schnelle Variable mit zwei unterschiedlichen charakteristischen Zeitskalen zerlegt werden kann. Zudem wird angenommen, dass der schnellste Term durch einen Gaußprozess (in dieser Arbeit ein OU-Prozess) approximiert werden kann. Sind diese Bedingungen erfüllt, dann ermöglicht die SMR, im Limit einer unendlichen Skalenseparation, die Konstruktion eines reduzierten stochastischen Modells (RSM), welches nur die langsame Variable beschreibt. Im RSM wird der Effekt der schnellen Variable durch eine stochastische Parametrisierung beschrieben, welche analytisch berechnet werden kann und von den Modellgleichungen abhängt. Abgesehen vom Tunen des OU-Prozesses verwendet die SMR dabei keine empirischen Parameter.

Bei der Anwendung der klassischen SMR ergibt sich allerdings ein kleineres konzeptionelles Problem. Die Substitution des schnellsten Terms durch einen OU-Prozess führt effektiv zu einer Energiequelle bzw. –senke im System. Die Energiefluktuation ist unbedenklich, sodass selbst lange Integrationen stabil bleiben. Dennoch suggeriert die Energiefluktuation eine Kopplung des QG3LM mit einem Energiereservoir. Daher wurde in dieser Arbeit das QG3LM in drei Variablen zerlegt: eine langsame, eine schnelle und eine versteckte Variable. Diese sind durch die führenden, die direkt darauffolgenden und die restlichen EOFs definiert, da die Zeitskala der Autokorrelation eine gute Übereinstimmung mit der erklärten Varianz der EOFs zeigte. Die versteckte Variable wurde durch eine lineare Schließung (analog zum SEM$_{\mathrm{det}}$) beschrieben. Der verbleibende nicht-parametrisierte Anteil der versteckten Variable stellt dann das Energiereservoir dar, mit dem der OU-Prozess gekoppelt ist und welcher die Energiefluktuationen in den explizit beschriebenen Variablen erklären kann. Dies führt zu zusätzlichen Tuningparameter in der Schließung. Wie allerdings im ersten Teil gezeigt, sollte es möglich sein diese mit dem FDT zu behandeln.

Für den ungestörten Fall lieferte das RSM qualitativ und quantitativ ähnliche Ergebnisse wie das SEM. Dieses Resultat scheint dabei weitestgehend unabhängig von der Wahl der langsamen und schnellen Variable zu sein. Allerdings ist davon auszugehen, dass für zu viele EOFs als langsame Variable die Annahme einer Skalenseparation verletzt wird. Die, mit der Literatur verglichen, relativ gute Leistung des RSM ist primär auf die zusätzliche Empirik durch die versteckten Variable zurückzuführen. Dennoch hat die analytische Schließung der SMR einen signifikanten Einfluss auf das RSM.

Zur Untersuchung der Fähigkeit des RSMs auf externe Antriebe zu reagieren, wurde das Modell mit der lokalen Heizung gestört. Dabei wurden zwei Antriebsarten betrachtet: die Heizung wirkte entweder auf alle Skalen (d.h. auf die langsame und schnelle Variable) oder nur auf SGS-Variable (d.h. die schnelle Variable). Im Vergleich zum ersten Teil der Dissertation wurde hierbei die Amplitude der Heizung verstärkt, sodass der Response des QG3LM signifikant größer ist, als der Bias des ungestörten RSMs. Es wurden fünf verschiedene Modelle untersucht: das a priori RSM (apr-RSM; unveränderte empirische Parameter, aber Anpassung der Schließung folgend der SMR), a posteriori RSM (apo-RSM; wie apr-RSM, aber mit perfekt getunten empirischen Parametern), qG-FDT RSM (FDT-RSM; wie apo-RSM, aber Tuningparameter mittels qG-FDT aktualisiert) und die analogen a priori SEM (apr-SEM) und qG-FDT SEM (FDT-SEM).

Beide Antriebsarten sind zu stark, um das lineare qG-FDT anwenden zu können: sowohl das FDT-RSM als auch das FDT-SEM produzierten unrealistische Ergebnisse oder sind instabil. Für schwächere Antriebe (die gleiche Amplitude wie im ersten Teil) konnte das qG-FDT die empirischen Parameter erfolgreich anpassen. Dabei lieferte das FDT-RSM eine ähnliche Leistung wie das apo-RSM. Unabhängig davon zeigten das apr-RSM und apo-RSM systematisch bessere Ergebnisse als das apr-SEM, selbst für die verstärken Antriebe. Dennoch sind die Amplitudenfehler im Response der RSMs im Schnitt größer als 100%, insbesondere in der Kovarianz der Stromfunktion. Ferner konnte keine systematische Verbesserung des apo-RSM gegenüber dem apr-RSM festgestellt werden, teilweise ist der Response des apo-RSM sogar schlechter. Für Anomalieexperimente unter idealisierten Bedingung (d.h. Eliminierung des Einflusses der empirischen Parameter) lieferte das RSM einen Response in der mittleren Stromfunktion und der Kovarianz der Stromfunktion, welcher sehr gut mit der Referenz übereinstimmt. Unter Berücksichtigung der Ergebnisse vom ersten Teil dieser Arbeit deutet dies darauf hin, dass das betrachtete RSM insgesamt zu niedrigdimensional ist, um es im Kontext von externen Antrieben abschließend zu evaluieren.

Alles in allem konnte gezeigt werden, dass das FDT prinzipiell in der Lage ist, sinnvolle Änderungen der Tuningparameter zu liefern und somit eine Klimaabhängigkeit einzuführen. Ferner wurde die SMR als eine Methode identifiziert, welche in der Tat auf ersten Prinzipien basiert: das RSM ist in der Lage automatisch auf externe Antriebe zu reagieren, ohne dass ein erneutes Tuning erforderlich ist. Allerdings konnte dies bislang nur für idealisierte Fälle gezeigt werden. Dennoch ermutigen die in dieser Arbeit präsentierten Ergebnisse, dass dies für höherdimensionale RSMs auch möglich sein sollte.

Abstract

State-of-the-art climate models contain, to a significant degree, empirical components. In particular, subgrid-scale (SGS) parameterizations are usually highly tuned against observations or high-resolution model data. While this enables the models to minimize the error during hindcasts, it is not guaranteed that it yields a benefit for climate projections because of climate change. In this thesis the Fluctuation-Dissipation theorem (FDT) is used to update the statistics of the system in the presence of an external forcing. If the empirical parameters are tuned objectively to the data (i.e., they depend on the statistics of the data), then they might be updated with the FDT. This ansatz is tested within a framework of a semi-empirical model (SEM) based on the leading variance patterns of a quasi-geostrophic three-layer model (QG3LM) and supplemented by a purely data-driven parameterization. We show that the FDT is able to successfully update the tuning parameters of the data-driven SGS closure, resulting in a systematic improvement in model performance in comparison to an untreated SEM. Ideally, SGS parameterizations should contain little to no tuning parameters. Thus, complementary to the FDT approach we investigate a stochastic SGS closure constrained by first principles that is calculated using the stochastic mode reduction (SMR). The SMR allows for an analytic derivation of the SGS closure from the model equations while requiring only minimal tuning. We successfully apply the SMR to the QG3LM and construct the reduced stochastic model (RSM). Furthermore, we show that the RSM is more robust against an external forcing than the SEM. Additionally, we find that, under appropriate conditions, the FDT is able to update the empirical parts of the RSM. Yet, only for the response in mean streamfunction the RSM provides useful results, while the response in covariance of the streamfunction is incorrect for most cases. Nevertheless, we obtain a remarkably accurate response in both moments for the RSM in an idealized setting. In combination with the results of the FDT study this indicates that the considered RSM is too low dimensional and encourages us to investigate the response of larger RSMs in the future.

Disclaimer

Parts of the following scientific results are published in Pieroth et al. (2018) (©American Meteorological Society. Used with Permission). In particular, some of the figures and tables are taken from this article. In those cases, the copyright has been stated in the figure/table caption. Additionally, some small text phrases are reused in this thesis. In order to increase the readability, the respective sentences are not highlighted within the text, but the copyright is stated only in this disclaimer.

Contents

Part I Dealing with Empirical Parameters in SGS Parameterizations

---

Part II SGS Parameterizations based on First Principle

Chapter 1

Introduction

1.1 Motivation

The climate system in general and the atmosphere in particular are multiscale systems. As such, they contain a wide range of temporal (seconds to millennia) and spatial (µm to 10 000 km) scales that interact with each other. An example for the scale interaction is the ice-albedo feedback (Peixoto and Oort 1992). Simply put, an increase/decrease in global mean temperature (global effect) decreases/increases the ice coverage of Earth and thus also the albedo (regional effect). In return, this leads to less/more reflection of incoming solar radiation (local effect), which eventually results in increased/decreased global mean temperature (global effect).

This scale interaction makes the simulation of the climate quite challenging. Because of the limited computational power and the discretization of the governing equations, a general circulation model (GCM; or climate model) can only resolve a part of the important scales explicitly. The remaining scales have to be described approximately by so-called subgrid-scale (SGS) parameterizations. Ideally, such an SGS closure is based on physics. However, some SGS processes are poorly understood (e.g., microphysics in clouds), and even if the SGS closure is based on physics, eventually it has to be expressed in terms of the resolved fields of the GCM. Consequently, the parameterizations are not closed equations but usually contain parameters whose value are not determined by theory. For example, climate models usually have a prescribed aerosol climatology (e.g., Stevens et al. 2013), but also small-scale features such as the root depth in soil models (e.g., Doms et al. 2011, pp. 99-129) or the launch level of parameterized gravity waves are free parameters (e.g., Hines 1997).

The empirical parameters are obtained by tuning against either observations or high-resolution model data. In principle, there exist two approaches for the tuning. First, the tuned parameters can be determined by trial and error. In this approach the parameters are changed manually until an optimum is found (e.g., Franzke and Majda 2006; Mauritsen et al. 2012). Even though this approach is relatively often used, the tuning is somewhat ambiguous and it is not guaranteed that a global optimum is found. More mathematically rigorous alternatives are the minimization of an error function (e.g., Achatz and Branstator 1999) or the application of the Maximum-Likelihood method (Honerkamp 1994).

Because of the significant amount of empirical parameters present in GCMs and climate models (e.g., Doms et al. 2011) the tuning is a crucial step in the model development (e.g., Reinert et al. 2019, pp. 3-6; Mauritsen et al. 2012). In fact, only the tuning allows the weather services to regularly generate skillful weather predictions for the next couple of days. However, tuning is not only necessary for numerical weather prediction but also in the context of climate modeling. There it is used to remove unrealistic climate drifts from the climate models, mainly by adjusting parameters connected with cloud physics (Mauritsen et al. 2012).

Nevertheless, tuning can also be harmful. When we tune parameterizations against data we introduce a data dependence in the empirical components. Hence, if the statistics of the system change because of modified external influences (e.g., forcings, boundary conditions) the original tuning parameters might no longer be useful. Rockel and Geyer (2008) illustrate this for the regional climate model COSMO-CLM (Fig. 1.1). They tuned the regional climate model for central Europe but used the same model setup also for other regions on Earth. For the quantification of the model performance the amount of precipitation of the COSMO-CLM is compared to a global data set. For Europe the model works quite well with a low bias and RMSE, and a high pattern correlation (Fig. 1.1, top). Nevertheless, using, for example, the same model setup for South America results in an overall worse performance (Fig. 1.1, bottom).

Other examples of modified external influences of the system beyond regional

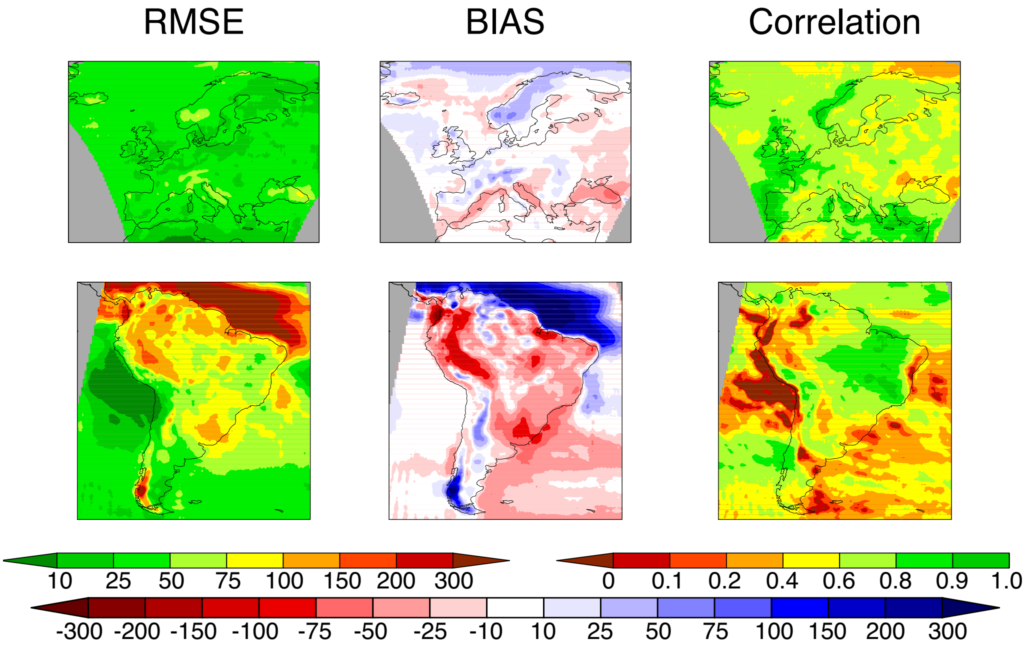

Figure 1.1: RMSE, bias, and correlation between the COSMO-CLM and a global data set of precipitation for the time period 2000-2004. (Top) European domain; (bottom) South America domain. Units are given in mm month^{-1} (adapted from Rockel and Geyer 2008).

climate models are a change in the radiation budget (Mauritsen et al. 2012), replacement of one or more parameterizations, a change in model resolution (Schättler et al. 2018), or the simulation of another planet's atmosphere. In each case (at least some part of) the empirical parameters have to be retuned, otherwise the respective model is unable to perform with the same quality.

The same issue arises for climate projections. The anthropogenic influence on Earth's climate has a drastic impact on, among others, the global mean temperature, sea level, precipitation patterns, or atmospheric phenomena such as ENSO, which cause flooding of islands and coastal regions and influence agriculture as well as other vital infrastructure (Field et al. 2014). However, the lack of observations of the future climate and the insufficient observational records from the past deny the validation of the climate response predicted by the models. Yet, there are indications in the literature that the tuning parameters have a significant effect on climate projections. For instance, Schirber et al. (2015) tune different gravity wave parameterization schemes (i.e., they differ, for example, in the propagation scheme, gravity-wave source, launch level, and horizontal wavelength) successfully to simulate the quasi-biennial oscillation with a GCM. However, in a climate-change experiment the response of the quasi-biennial oscillation experiences a strong dependence on the chosen scheme.

This effect is even more pronounced for low-order models with purely data-driven parameterizations. For example, Achatz and Branstator (1999) and Achatz and Opsteegh (2003b) create low-order models based on empirical orthogonal functions (EOFs) of two different GCMs. Furthermore, the reduced models are equipped with a purely data-driven linear SGS parameterization, to account for the unresolved scales resulting from of the EOF truncation. The low-order models successfully capture the characteristic of the respective GCM dynamics (e.g., averaged transient eddy fluxes and the statistics of the first and second moment of the streamfunction). They fail, however, in capturing the correct response of the GCMs in the presence of a local anomalous heating in the tropics.

Given the fact that state-of-the-art models used for climate projections (e.g., the models of CMIP5 and CMIP3, Flato et al. 2013) contain hundreds of empirical parameters, we require an approach that takes the data dependence of the tuning parameters into account. Achatz et al. (2013) propose to use the Fluctuation-Dissipation theorem (FDT) for this purpose. The FDT is based on a linear theory that connects suitable correlation functions with the response of a perturbed system. This allows the estimation of the perturbed statistics caused by a sufficiently small external forcing or small change in model parameters (Risken 1984). The theorem has a long history in equilibrium statistical mechanics, where it can be used to study macroscopic quantities by analyzing correlation functions, dating back to Einstein's work on Brownian motion (Einstein 1905; Marconi et al. 2008). However, a generalized FDT holds also for a larger class of systems with chaotic dynamics, such as the climate (see Marconi et al. 2008, for a recent review).

Originally Leith (1975, 1978) proposed using the FDT for the estimation of the climate response. Since then it has been shown that the FDT is able to provide a useful estimation of the linear response for simple GCMs (Gritsun and Branstator 2007; Gritsun et al. 2008; Ring and Plumb 2008) and even coupled atmosphere-ocean GCMs (Gritsun and Branstator 2016). Nevertheless, even for small external forcings the response can be quite nonlinear (Pieroth et al. 2018). Still, the linear estimations of the FDT may be used in combination with a nonlinear model to obtain skillful estimations of the climate response (Achatz et al. 2013; Pieroth et al. 2018).

Achatz et al. (2013) were the first to see the potential of the FDT to introduce a climate dependence in empirical parameters of SGS closures. If the empirical parameters are tuned objectively (i.e., they depend on the statistics of the data), the linear estimations of the change in the statistics provided by the FDT may be used to update the empirical parameters. Achatz et al. (2013) tested this ansatz on the barotropic vorticity equation on the sphere. The FDT approach worked reasonable well, however, only a part of the tuning parameters could be updated, because of the poorly fulfilled constraints of the theorem. The FDT requires a system in equilibrium with a differentiable probability density function (PDF). In particular, the latter condition is violated in systems with deterministic chaos. Adding suitable random noise to the system smooths the PDF and solves this issue (Zeeman 1988). Indeed, Pieroth et al. (2018) could successfully update their data-driven closure with the FDT for a quasigeostrophic three-layer model (QG3LM). Even though the QG3LM is still a deterministic system, it contains already sufficiently fast processes which act similarly to an explicit noise.

The FDT approach reportedly works, yet it can only be seen as a temporary solution. In the long run climate models should contain little to no tuning parameters. Therefore, SGS parameterizations based on first principles (i.e., directly obtained from model equations with little to none empirical tuning) should be used. One approach is a closure based on the maximum entropy principle (Verkley and Severijns 2014). This SGS parameterization requires no tuning and has been applied successfully to a two-dimensional flow (Verkley et al. 2016). Furthermore, Wouters and Lucarini (2012) proposed a closure based on response theory that relies on weak coupling between the resolved and SGS processes, respectively (Wouters et al. 2016; Demaeyer and Vannitsem 2017).

Alternatively, the stochastic mode reduction (SMR; Majda et al. 2001, 2003) can be applied to a system with a strict scale separation, which, in principle, makes it suitable for the atmosphere and the climate. In the SMR the nonlinear self-interaction of the SGS processes is approximated by an empirical Ornstein-

Uhlenbeck process (OU-process). In return, this OU-process can then be used to derive an SGS parameterization explicitly from the model equations. Even though there is still some tuning involved, this analytically derived closure should be more robust to climate change than traditional SGS parameterizations.

Parameterizations based on first principles certainly circumvent the problem of tuning parameters. However, such closures are still in development and not used operationally. State-of-the-art GCMs and climate models still rely on heavily tuned SGS parameterizations. Thus, in this thesis we want to address two research questions:

1. Can we introduce a climate dependence in empirical parameters of SGS parameterizations?
2. Does the SMR provide a parameterization that is robust with respect to a perturbed model climate?

Therefore, this thesis consists of two parts. First we show that in principle the FDT is able to introduce a useful climate dependence of the tuning parameters (i.e., models with an updated SGS closure perform systematically better in a perturbed climate than models with a fixed closure). Hence, the FDT might offer a method to deal with existing tuning parameters in state-of-the-art GCMs. Secondly, we consider the SMR approach and show that, since it is constrained by first principles, the resulting closure is able to react to an external forcing. Since there is still a remaining empirical part involved we treat that with the FDT to improve the result.

1.2 Structure

The thesis is structured as follows. In part I we investigate the application of the FDT as an approach to introduce a climate dependence on empirical parameters of SGS parameterizations. First, we derive the general form of the FDT in chapter 2. Furthermore, we introduce the approximated quasi-Gaussian FDT and the more sophisticated blended Short-Time/quasi-Gaussian FDT. In chapter 3 the models used in this thesis are presented. This includes the QG3LM and a low-order semi-empirical model with a purely data-driven closure that serves as a testbed of the

FDT ansatz. Chapter 4 describes the climate dependence in the empirical tuning parameters by the FDT. The corresponding numerical experiments are presented in chapter 5.

Part II contains the construction of an SGS parameterization based on first principles using the SMR. The latter is presented in chapter 6 where we derive a reduced equation for the slow variable. In chapter 7 we apply the SMR to the QG3LM. The analytic and numerical results are given in chapter 8. First we analyze the performance of the reduced stochastic model (RSM). Furthermore, we test the robustness of the SMR closure with respect to a perturbed model climate. In addition, we go beyond the classical SMR and construct a RSM that includes explicitly the nonlinear self-interaction of the fast variable. Finally, we conclude this thesis in chapter 9.

1.3 Notation

Let $\mathbf{a}, \mathbf{b} \in \mathbb{R}^N$ and $\mathsf{A}, \mathsf{B} \in \mathbb{R}^{N \times N}$ be arbitrary vectors and matrices, respectively. The scalar product (inner product) is then defined by

$$\mathbf{a} \cdot \mathbf{b} = \langle \mathbf{a}, \mathbf{b} \rangle = \sum_i^N a_i b_i \equiv a_i b_i \,, \tag{1.1}$$

where in the last step (and from now onward) we applied Einstein's summation convention. In contrast, the inner product of two matrices (Frobenius product) is denoted by

$$\mathsf{A} : \mathsf{B} = \mathrm{tr}(\mathsf{A}^{\mathrm{T}} \mathsf{B}) = \mathsf{A}_{ij} \mathsf{B}_{ij} \,, \tag{1.2}$$

where $\mathrm{tr}(\cdot)$ is the trace of a matrix. Moreover, the outer product of two vectors $\mathbf{a} \otimes \mathbf{b} \in \mathbb{R}^{N \times N}$ defines a matrix, which is given by

$$\mathbf{a} \otimes \mathbf{b} = \mathbf{a} \mathbf{b}^{\mathrm{T}} \,. \tag{1.3}$$

Let ∇_z and $\nabla_z \cdot$ be the gradient and divergence with respect to variable $\mathbf{z} \in \mathbb{R}^N$. Then we have for an arbitrary, sufficiently differentiable scalar field $\phi(\mathbf{z}) \in \mathbb{R}$ and vector field $\mathbf{v}(\mathbf{z}) \in \mathbb{R}^N$, as well as for a matrix valued function $\mathsf{A}(\mathbf{z}) \in \mathbb{R}^{N \times N}$

$$(\nabla_z \phi)_i = \frac{\partial \phi}{\partial z_i} \qquad (\nabla_z \mathbf{v})_{ij} = \frac{\partial v_i}{\partial z_j} \tag{1.4}$$

$$\nabla_z \cdot \mathbf{v} = \frac{\partial v_i}{\partial z_i} \qquad (\nabla_z \cdot \mathsf{A})_i = \frac{\partial \mathsf{A}_{ij}}{\partial z_j} \,. \tag{1.5}$$

Moreover, we write the Laplacian and the Hessian as

$$\Delta_z \phi = \nabla_z \cdot \nabla_z \phi \qquad (\nabla_z \nabla_z \phi)_{ij} = \frac{\partial^2 \phi}{\partial z_i \partial z_j} \,. \tag{1.6}$$

For a given PDF $\rho(\mathbf{z})$ [conditional PDF $\rho(\mathbf{z}, t | \mathbf{z}_0, 0)$] and an arbitrary function

$f(\mathbf{z})$ we write the expectation value as

$$\mathbb{E}\left[f(\mathbf{z})\right] = \int \rho(\mathbf{z}) f(\mathbf{z}) \mathrm{d}^N\mathbf{z} \tag{1.7}$$

$$\mathbb{E}\left[f(\mathbf{z},t)|\mathbf{z}(0)=\mathbf{z}_0)\right] = \int \rho(\mathbf{z},t|\mathbf{z}_0,0) f(\mathbf{z}) \mathrm{d}^N\mathbf{z}\,. \tag{1.8}$$

Furthermore, we assume ergodicity, which allows us to approximate the expectation value by a time average. Thus, for a sufficiently long discrete time series $\{f_1(\mathbf{z}), f_2(\mathbf{z}), \ldots, f_{N_t}(\mathbf{z})\}$ we may write (1.7) as

$$\mathbb{E}\left[f(\mathbf{z})\right] \simeq \langle f(\mathbf{z})\rangle = \frac{1}{N_t}\sum_{n=1}^{N_t} f_n(\mathbf{z})\,. \tag{1.9}$$

Lastly, we indicate deviations from the time average by primes:

$$\mathbf{z}' = \mathbf{z} - \langle \mathbf{z} \rangle\,. \tag{1.10}$$

Part I

Dealing with Empirical Parameters in Subgrid-Scale Parameterizations

Chapter 2

Fluctuation-Dissipation Theorem

To understand the Fluctuation-Dissipation theorem (FDT) conceptually let us consider a system in statistical steady state (i.e., the system is in steady state if we average over a suitable time interval). The physical quantities of such a system are not at rest but are constantly fluctuating. Mathematically the fluctuations are described by correlation functions between the quantities in question. On the other hand, an external forcing or change in model parameters drives the system away from its statistical steady state. If the perturbation is sufficiently small (i.e., we do not trigger any tipping points), the model will return to its statistical steady state when the forcing is switched off. This can be described by a linear response function that expresses the decay of expectation values from their steady-state values. The similarity to the fluctuations allows a connection between the response function and the correlation function: the FDT (Risken 1984).

Since the theorem is based on correlation functions, no knowledge about the governing equations is required. Nevertheless, there are several constraints, which have to be fulfilled. The system must be in statistical equilibrium and needs a time-invariant, differentiable probability density function (PDF). While it is possible to extend the theory to time-periodic cases (Majda and Wang 2010; Gritsun 2010) and to nonequilibrium systems (Lucarini and Sarno 2011; Ragone et al. 2016), the differentiability of the PDF is violated in systems experiencing deterministic chaos. The attractor of such systems is usually fractal. Nevertheless, the differentiability can be ensured by adding a suitable noise term that smooths the PDF (Zeeman

1988). In practice we assume that the smallest scales of the model are sufficiently irregular and thus smooth the PDF.

Leith (1975, 1978) was the first to propose estimating the climate response with the FDT. Since then the theorem has been applied to various idealized climate models (e.g., Bell 1980; North et al. 1993; Gritsoun and Dymnikov 1999; Gershgorin and Majda 2010; Achatz et al. 2013; Fuchs et al. 2015; Lutsko et al. 2015; Pieroth et al. 2018), simple GCMs (Gritsun and Branstator 2007; Gritsun et al. 2008; Ring and Plumb 2008), and even coupled atmosphere-ocean GCMs (Gritsun and Branstator 2016). However, these studies show a mixed performance of the FDT, for reasons that remain unclear. Firstly, the different forcings and models deny a direct comparison of the studies. Secondly, it is possible that the forcings project onto a stable direction of the attractor, resulting in a response that is not covered by the fluctuations of the unperturbed model (Gritsun and Lucarini 2017). Another possibility could be the nonnormality of the FDT-response operator that might lead to strong interactions between resolved and unresolved EOFs, which cannot be captured by a response operator in an EOF subspace (Hassanzadeh and Kuang 2016). Furthermore, the quality of the response operator also depends on the length of the data used for its construction (Gottwald et al. 2016). In particular, for the climate sensitivity Kirk-Davidoff (2008) shows that the available temperature observations are insufficient for a robust estimate.

In addition to this “external” error sources the theory itself includes approximations. The general form of the FDT cannot be applied to realistic cases since it requires the differentiation of the (usually unknown) PDF. Thus, commonly the so-called quasi-Gaussian FDT (qG-FDT; Bell 1980; Majda et al. 2005) is used where the unknown equilibrium PDF is assumed to be Gaussian. This assumption may be relaxed by use of a nonparametric kernel method (Cooper and Haynes 2011). Furthermore, the differentiation of the PDF can be avoided altogether with the blended short-time/quasi-Gaussian FDT (ST/qG-FDT) of Abramov and Majda (2007, 2008, 2009). Instead this algorithm utilizes a tangent linear model to construct the response operator. In comparison to the simple qG-FDT, these methods produce superior results, however, they are also computationally more expensive. Thus, in this thesis we focus on the simple qG-FDT and compare its results with the ST/qG-FDT for selected cases.

2.1 The general Fluctuation-Dissipation Theorem

Let us approximate the atmosphere by a finite-dimensional state vector $\mathbf{x} \in \mathbb{R}^N$. Furthermore, we assume that the (unresolved) smallest-scale processes are sufficiently irregular to describe the atmosphere by an autonomous[1] Itô stochastic differential equation (Itô-SDE):

$$\begin{aligned} \mathrm{d}\mathbf{x} &= \mathbf{G}(\mathbf{x})\mathrm{d}t && (2.1)\\ &\approx \mathbf{f}(\mathbf{x})\mathrm{d}t + \boldsymbol{\sigma}(\mathbf{x})\mathrm{d}\mathbf{W}\,, && (2.2) \end{aligned}$$

where $\mathbf{G}(\mathbf{x}) \in \mathbb{R}^N$ is the original system that is approximated by a deterministic part $\mathbf{f} \in \mathbb{R}^N$, a diffusion tensor $\boldsymbol{\sigma} \in \mathbb{R}^{N\times N}$, and a Wiener increment $\mathrm{d}\mathbf{W} \in \mathbb{R}^N$.

This Itô-SDE has a corresponding forward Fokker-Planck equation (FPE; Gardiner 2009) for the PDF $p(\mathbf{x}, t|\mathbf{x}_0, t_0)$ of the system given by

$$\partial_t p(\mathbf{x}, t|\mathbf{x}_0, t_0) = -\nabla_x \cdot [\mathbf{f}(\mathbf{x}) p(\mathbf{x}, t|\mathbf{x}_0, t_0)] + \frac{1}{2}\nabla_x\nabla_x : \left[\boldsymbol{\sigma}(\mathbf{x})\boldsymbol{\sigma}^{\mathrm{T}}(\mathbf{x}) p(\mathbf{x}, t|\mathbf{x}_0, t_0)\right] \,. \tag{2.3}$$

For simplicity we suppress the condition of the PDF and set $p(\mathbf{x}, t) \equiv p(\mathbf{x}, t|\mathbf{x}_0, t_0)$ from now on. The introduction of the partial differential operator L_x allows us to write (2.3) as

$$\partial_t p(\mathbf{x}, t) \equiv \mathsf{L}_x p(\mathbf{x}, t)\,. \tag{2.4}$$

The formal solution of (2.4) reads

$$p(\mathbf{x}, t) = e^{\mathsf{L}_x t} p(\mathbf{x}, 0)\,, \tag{2.5}$$

where $p(\mathbf{x}, 0)$ is the initial condition.

---

[1] Autonomy of the Itô-SDE is not required for the general and the quasi-Gaussian FDT, respectively. However, it is necessary for the derivation of the ST-FDT.

Consider a small deterministic perturbation

$$\mathbf{f}(\mathbf{x}) \longrightarrow \mathbf{f}(\mathbf{x}) + \delta\tilde{\mathbf{f}}(\mathbf{x}, t)\,, \tag{2.6}$$

with $\delta\tilde{\mathbf{f}}(\mathbf{x}, t) = 0$, $\forall t \leq 0$. This perturbation induces also a change in the PDF, given by

$$p(\mathbf{x}, t) \longrightarrow p(\mathbf{x}, t) + \delta p(\mathbf{x}, t)\,, \tag{2.7}$$

which we assume to be small (i.e., $\delta p(\mathbf{x}, t) \ll p(\mathbf{x}, t)$) as well. Insertion in (2.3) leads to

$$\begin{aligned} \partial_t[p(\mathbf{x}, t) + \delta p(\mathbf{x}, t)] &= -\nabla_x \cdot \Big\{ \big[\mathbf{f}(\mathbf{x}, t) + \delta\tilde{\mathbf{f}}(\mathbf{x}, t)\big]\big[p(\mathbf{x}, t) + \delta p(\mathbf{x}, t)\big] \Big\} \\ &\quad + \frac{1}{2}\nabla_x\nabla_x : \big\{ \boldsymbol{\sigma}(\mathbf{x})\boldsymbol{\sigma}^{\mathrm{T}}(\mathbf{x})\big[p(\mathbf{x}, t) + \delta p(\mathbf{x}, t)\big] \big\} \qquad (2.8) \\ \partial_t p(\mathbf{x}, t) + \partial_t \delta p(\mathbf{x}, t) &= \mathbf{L}_x p(\mathbf{x}, t) + \mathbf{L}_x \delta p(\mathbf{x}, t) - \nabla_x \cdot \big[\delta\tilde{\mathbf{f}}(\mathbf{x}, t) p(\mathbf{x}, t)\big] \\ &\quad - \nabla_x \cdot \big[\delta\tilde{\mathbf{f}}(\mathbf{x}, t)\delta p(\mathbf{x}, t)\big]\,. \qquad (2.9) \end{aligned}$$

Since the perturbations are small, the last term can be neglected. Furthermore, using (2.4), the FPE of the perturbed PDF reads

$$\partial_t \delta p(\mathbf{x}, t) = \mathbf{L}_x \delta p(\mathbf{x}, t) + \tilde{\mathbf{L}}_x^{\text{pert.}}(\mathbf{x}, t) p(\mathbf{x}, t)\,, \tag{2.10}$$

where the perturbed FPE operator is given by

$$\tilde{\mathbf{L}}_x^{\text{pert.}}(\mathbf{x}, t) = -\nabla_x \cdot \delta\tilde{\mathbf{f}}(\mathbf{x}, t) p(\mathbf{x}, t)\,. \tag{2.11}$$

Assuming that the unperturbed system is in equilibrium [i.e., $p(\mathbf{x}, t) = \rho(\mathbf{x})$, where $\rho(\mathbf{x})$ is the invariant measure] so that

$$\mathbf{L}_x \rho(\mathbf{x}) = 0\,, \tag{2.12}$$

allows us to write the formal solution of (2.11) as

$$\delta p(\mathbf{x},t) = \int_0^t e^{\mathsf{L}_x (t-s)} \tilde{\mathsf{L}}_x^{\text{pert.}}(\mathbf{x},s)\rho(\mathbf{x})\mathrm{d}s\,, \tag{2.13}$$

because $\tilde{\mathsf{L}}_x^{\text{pert.}}(\mathbf{x},0) = 0$, since we have $\delta\tilde{\mathbf{f}}(\mathbf{x},t) = 0$, $\forall t \leq 0$ (Risken 1984).

Let $h(\mathbf{x})$ be an arbitrary observable (i.e., either a scalar, vector, or matrix-valued function, respectively), depending on the state vector of the system. Then the perturbed expectation value is given by

$$\delta\mathbb{E}[h](t) = \int h(\mathbf{x})\delta p(\mathbf{x},t)\mathrm{d}^N\mathbf{x} \tag{2.14}$$

$$= \int h(\mathbf{x}) \int_0^t e^{\mathsf{L}_x (t-s)} \tilde{\mathsf{L}}_x^{\text{pert.}}(\mathbf{x},s)\rho(\mathbf{x})\mathrm{d}s\mathrm{d}^N\mathbf{x}\,. \tag{2.15}$$

Furthermore, let us assume that the deterministic perturbation $\delta\tilde{\mathbf{f}}(\mathbf{x},t)$ in (2.6) depends multiplicatively on time (no Einstein's summation convention):

$$\delta\tilde{f}_i(\mathbf{x},t) = \delta f_i(\mathbf{x})w_i(t)\,. \tag{2.16}$$

From this follows

$$\tilde{\mathsf{L}}_x^{\text{pert.}}(\mathbf{x},t) = -\partial_{x_i}\delta f_i(\mathbf{x})w_i(t) \equiv \mathsf{L}_x^{\text{pert.}}(\mathbf{x})\mathbf{w}(t) \tag{2.17}$$

(Risken 1984). Thus, with the substitution $\tau = t - s$ we may write (2.15) as

$$\delta\mathbb{E}[h](t) = \int_0^t \mathsf{R}(h,\tau)\mathbf{w}(t-\tau)\mathrm{d}\tau\,, \tag{2.18}$$

where the response operator is given by

$$\mathsf{R}(h,t) = \int h(\mathbf{x})e^{\mathsf{L}_x t}\mathsf{L}_x^{\text{pert.}}(\mathbf{x})\rho(\mathbf{x})\mathrm{d}^N\mathbf{x}\,. \tag{2.19}$$

For further evaluation of the response operator we consider a general cross correlation

$$\mathbb{E}[h(\mathbf{x}[t+\tau])g(\mathbf{x}[t])] = \int \mathrm{d}^N\mathbf{x}h(\mathbf{x}) \int \mathrm{d}^N\mathbf{y}p(\mathbf{x},t+\tau|\mathbf{y},t)\rho(\mathbf{y})g(\mathbf{y})\,, \tag{2.20}$$

where $g(\mathbf{x})$ is an arbitrary integrable function. Obviously we have

$$p(\mathbf{x},t+\tau|\mathbf{y},t) = e^{\mathsf{L}_x\tau}\delta(\mathbf{x}-\mathbf{y})\,. \tag{2.21}$$

Thus, (2.20) can be written as

$$\mathbb{E}[h(\mathbf{x}[t+\tau])g(\mathbf{x}[t])] = \int \mathrm{d}^N\mathbf{x}h(\mathbf{x}) \int \mathrm{d}^N\mathbf{y}e^{\mathsf{L}_x\tau}\delta(\mathbf{x}-\mathbf{y})\rho(\mathbf{y})g(\mathbf{y}) \tag{2.22}$$

$$= \int \mathrm{d}^N\mathbf{x}h(\mathbf{x})e^{\mathsf{L}_x\tau}[g(\mathbf{x})\rho(\mathbf{x})]\,. \tag{2.23}$$

Comparison with the response operator (2.19) leads to

$$\mathbf{R}(h,t) = \mathbb{E}\left[h(\mathbf{x}[t+\tau])\left(\frac{1}{\rho(\mathbf{x})}\mathsf{L}_x^{\mathrm{pert.}}(\mathbf{x})\{\rho(\mathbf{x})\}\right)_{\mathbf{x}=\mathbf{x}(t)}\right]\,. \tag{2.24}$$

Finally, substituting the perturbed Fokker-Planck operator results in the general form of the FDT (Risken 1984):

$$\delta\mathbb{E}[h](t) = -\int_0^t \mathbb{E}\left[h(\mathbf{x}[t+\tau])\left(\frac{1}{\rho(\mathbf{x})}\partial_{x_i}\{\delta f_i(\mathbf{x})\rho(\mathbf{x})\}\right)_{\mathbf{x}=\mathbf{x}(t)} w_i(t-\tau)\right]\mathrm{d}\tau\,. \tag{2.25}$$

For the remainder of this thesis we consider an anomalous forcing that is independent of space and time (i.e., $\delta\tilde{\mathbf{f}}(\mathbf{x},t) = \delta\mathbf{f} = \mathit{const.}$). With this assumption (2.25) simplifies to

$$\delta\mathbb{E}[h](t) = -\int_0^t \mathbb{E}\left[h(\mathbf{x}[t+\tau])\left(\frac{\nabla_x\rho(\mathbf{x})}{\rho(\mathbf{x})}\right)_{\mathbf{x}=\mathbf{x}(t)}\right]\mathrm{d}\tau\cdot\delta\mathbf{f}\,. \tag{2.26}$$

Consequently, we restrict our investigation on what Risken (1984) called Step-Response function or Excitation function.

2.2 Quasi-Gaussian Fluctuation-Dissipation Theorem

While the general form of the FDT (2.26) is certainly elegant and compact, it has one fundamental disadvantage: the exact form of the invariant measure has to be known. However, in general (and in particularly in the case of the atmosphere) the equilibrium PDF of the system is unknown. Consequently, it is impossible to use (2.26), and thus further assumptions have to be made.

The simplest approximation of the general FDT results in the qG-FDT. Here we assume that, because of the central limit theorem, the stationary PDF can be approximated by a Gaussian distribution:

$$\rho(\mathbf{x}) = \frac{1}{\sqrt{\det[2\pi\mathbf{\Sigma}(0)]}} \exp\left[-\frac{1}{2}\mathbf{x}'^{\mathrm{T}}\mathbf{\Sigma}^{-1}(0)\mathbf{x}'\right] , \tag{2.27}$$

where $\mathbf{\Sigma}(\tau) = \mathbb{E}[\mathbf{x}'(\tau)\mathbf{x}'^{\mathrm{T}}(0)]$ is the τ-lag cross-covariance matrix and the mean and variance of (2.27) is taken from data (i.e., sampled from the unknown stationary PDF hence the name quasi-Gaussian). Thus follows

$$\nabla\rho(\mathbf{x}) = -\rho(\mathbf{x})\mathbf{x}'^{\mathrm{T}}\mathbf{\Sigma}^{-1}(0) , \tag{2.28}$$

since $\mathbf{\Sigma}(0)$ is symmetric. Hence, (2.26) may be written as

$$\delta\mathbb{E}[h](t) = -\int_0^t \mathbb{E}\left[h(\mathbf{x}[t+\tau])\left(-\mathbf{x}'^{\mathrm{T}}\mathbf{\Sigma}^{-1}[0]\right)_{\mathbf{x}=\mathbf{x}(t)}\right]\mathrm{d}\tau\delta\mathbf{f} \tag{2.29}$$

$$= \int_0^t \mathbb{E}\left[h(\mathbf{x}[t+\tau])\mathbf{x}'^{\mathrm{T}}(t)\right]\mathbf{\Sigma}^{-1}(0)\mathrm{d}\tau\delta\mathbf{f} . \tag{2.30}$$

The calculation of this simple cross-correlation is significantly easier and faster compared to the general FDT. In particular, when using efficient algorithms such as the Cooper-Hanyes algorithm (Lutsko et al. 2015) to solve the lag integral (see appendix A.1). This makes the qG-FDT the most commonly used form of the FDT.

2.3 Short-Time Fluctuation-Dissipation Theorem

While the qG-FDT is computationally cheap and simple, it still makes the strong assumption of a Gaussian distributed PDF of the system. Even though the mean and variance of the true (unknown) PDF is used, this approximation introduces potentially high errors (e.g., if the underlying PDF is bimodal). Abramov and Majda (2007) introduced for deterministic systems an alternative ansatz known as the Short-Time FDT (ST-FDT). They rearrange the response operator and thus eliminate the dependence on the PDF of the system. In this section we derive this ST-FDT and discuss its strengths and weaknesses.

Starting from (2.18) with a constant anomalous forcing, we note that this integral can be seen as a scalar product

$$\delta\mathbb{E}[h](t) = \int\int_0^t h(\mathbf{x}) e^{\mathsf{L}_x\tau}\mathsf{L}_x^{\text{pert.}}\rho(\mathbf{x})\mathrm{d}\tau\mathrm{d}^N\mathbf{x} \tag{2.31}$$

$$\equiv \int_0^t \left\langle h(\mathbf{x}), e^{\mathsf{L}_x\tau}\mathsf{L}_x^{\text{pert.}}\rho(\mathbf{x})\right\rangle \mathrm{d}\tau\,. \tag{2.32}$$

Thus, we may write

$$\delta\mathbb{E}[h](t) = \int_0^t \left\langle \mathsf{L}_x^{\text{pert.}\dagger} e^{\mathsf{L}_x^\dagger\tau} h(\mathbf{x}), \rho(\mathbf{x})\right\rangle \mathrm{d}\tau$$

$$\equiv \int\int_0^t \left\{\mathsf{L}_x^{\text{pert.}\dagger} e^{\mathsf{L}_x^\dagger\tau} h(\mathbf{x})\right\}\rho(\mathbf{x})\mathrm{d}\tau\mathrm{d}^N\mathbf{x}\,, \tag{2.33}$$

where $\mathsf{L}_x^\dagger$ and $\mathsf{L}_x^{\text{pert.}\dagger}$ are the adjoint operators given by

$$\mathsf{L}_x^\dagger = \mathbf{G}\cdot\nabla \tag{2.34a}$$

$$\mathsf{L}_x^{\text{pert.}\dagger} = \delta\mathbf{f}^{\mathrm{T}}\nabla\,. \tag{2.34b}$$

Alternatively, (2.33) can be obtained by integrating (2.18) by parts (Abramov and Majda 2008).

Next Abramov and Majda (2008) define an auxiliary function $\mathcal{H} : [\mathbb{R} \times \mathbb{R}^N] \to \mathbb{R}^\bullet$ (where $\bullet$ depends on the dimension of h), given by

$$\mathcal{H}(t, \mathbf{x}) = h(\mathbf{X}[-t, \mathbf{x}]) = h(\mathbf{x}_0)\,, \tag{2.35}$$

with the solution operator $\mathbf{X}(t, \mathbf{x}_0) = \mathbf{x}(t)$ and an initial condition $\mathbf{x}_0$. No time dependence arises on the right-hand side in (2.35), since the considered system (2.1) is autonomous. Consequently, the time derivative vanishes and we have

$$0 = \frac{d\mathcal{H}}{dt} = \frac{\partial \mathcal{H}}{\partial t} + \mathsf{L}_x^\dagger \mathcal{H}\,, \tag{2.36}$$

as can be easily shown using the chain rule. The formal solution of this partial differential equation reads

$$\mathcal{H}(t, \mathbf{x}) = e^{-\mathsf{L}_x^\dagger t} \mathcal{H}(0, \mathbf{x}). \tag{2.37}$$

Furthermore, if we substitute t with $-t$ and use (2.35) once more, we can write (2.37) as

$$e^{\mathsf{L}_x^\dagger t} h(\mathbf{x}) = h(\mathbf{X}[t, \mathbf{x}])\,. \tag{2.38}$$

Using this identity in (2.33) we have

$$\delta\mathbb{E}[h](t) = \int\limits_0^t \mathbb{E}\left[\mathsf{L}_x^{\text{pert.}\dagger} h(\mathbf{X}[\tau, \mathbf{x}])\right] \mathrm{d}\tau\,, \tag{2.39}$$

where we replaced the integral over the PDF with the expectation value. Substituting the adjoint perturbed Fokker-Planck operator (2.34b) yields

$$\delta\mathbb{E}[h](t) = \int\limits_0^t \mathbb{E}\left[\delta\mathbf{f}^{\mathrm{T}} \nabla_{\mathbf{x}} h(\mathbf{X}[\tau, \mathbf{x}])\right] \mathrm{d}\tau\,, \tag{2.40}$$

where the index of $\nabla_{\mathbf{x}}$ indicates that the derivative acts on the argument of the solution operator. The nonlocal derivative $\nabla_{\mathbf{x}} h(\mathbf{X}[\tau, \mathbf{x}])$ can be calculated with the tangent linear model (see appendix A.2)

$$\mathbf{T}^{\tau}_{\mathbf{x}(t)} = \mathbb{T}\exp\left(\int\limits_{t}^{t+\tau} \nabla\mathbf{G}(\mathbf{x}[s])\mathrm{d}s\right) , \tag{2.41}$$

where $\mathbb{T}$ is the time-order operator and $\mathbf{T}^{\tau}_{\mathbf{x}(t)} \in \mathbb{R}^{N\times N}$ is integrated from $\mathbf{x}(t)$ to time τ. Thus, the ST-FDT response reads

$$\delta\mathbb{E}[h](t) = \int\limits_{0}^{t} \mathbb{E}\left[\delta\mathbf{f}^{\mathrm{T}}\nabla h(\mathbf{x}[t+\tau])\mathbf{T}^{\tau}_{\mathbf{x}(t)}\right]\mathrm{d}\tau\,, \tag{2.42}$$

where the tangent linear model can be calculated by

$$\frac{\mathrm{d}\mathbf{T}^{\tau}_{\mathbf{x}(t)}}{\mathrm{d}t} = \nabla\mathbf{G}[\mathbf{x}(t+\tau)]\mathbf{T}^{\tau}_{\mathbf{x}(t)}\,. \tag{2.43}$$

In contrast to the general FDT, the ST-FDT does no longer depend explicitly on the PDF. Therefore, the resulting response is in general more accurate than that of the qG-FDT, since the assumption of Gaussianity is dropped. However, the price for the higher accuracy is the need of the tangent linear model, which is computationally expensive. Abramov and Majda (2008) provide an algorithm for the calculation of (2.43) based on the QR-decomposition. Moreover, Abramov and Majda (2009) introduces a tangent linear model with a reduced rank, which further reduces the computational effort, although at the expense of accuracy. If the gradient of the system (2.1) can be calculated explicitly, the tangent linear model can be obtained by the algorithm of Baiesi and Maes (2013). However, this algorithm gets quite expensive for large systems. Consequently, it is not applicable in this thesis.

Regardless of the computational method the tangent linear model suffers from inherent instability. This renders the ST-FDT useless for long lead times. To counter the instability Abramov and Majda (2007) propose a combination of the qG-FDT and the ST-FDT response operators. The equilibrium response (i.e.,

$t \longrightarrow \infty$) of this so-called blended ST/qG-FDT reads as follows:

$$\delta\mathbb{E}[h] = \int\limits_{0}^{\tau_*} \mathbb{E}\left[\delta\mathbf{f}^{\mathrm{T}}\nabla h(\mathbf{x}[t+\tau])\mathsf{\mathbf{T}}^{\tau}_{\mathbf{x}(t)}\right] \mathrm{d}\tau + \int\limits_{\tau_*}^{\infty} \mathbb{E}\Big[h(\mathbf{x}[t+\tau])\mathbf{x}'^{\mathrm{T}}(t)\Big]\, \boldsymbol{\Sigma}^{-1}(0)\mathrm{d}\tau\delta\mathbf{f}\,, \tag{2.44}$$

where τ_* is the integration time up to which the tangent linear model is still stable. This blended algorithm utilizes the superior accuracy of the ST-FDT for the short lead time and combines it with the traditional qG-FDT for longer integration times. Even though the blending is done in a rather crude way, Abramov and Majda (2007, 2008, 2009) have shown that the blended ST/qG-FDT has better skill than the qG-FDT. However, the ambiguous choice of τ_* and the ad-hoc blending limit the robustness of this method.

Chapter 3

Models

In this chapter we introduce the reference model used to address the research questions of this thesis. Furthermore, we construct a low-order model based on a limited number of variance patterns that is additionally equipped with a purely data-driven parameterization. This reduced model serves then as a testbed of the FDT approach to introduce a climate dependence on tuning parameters of SGS closures.

3.1 Quasigeostrophic Three-Layer Model

This thesis uses the quasigeostrophic three-layer model (QG3LM) of Marshall and Molteni (1993) as a toy model of the atmosphere. The model is governed by the potential vorticity equation on the sphere, given by

$$\frac{\partial q_i}{\partial t} = -J(\Psi_i, q_i) + D_i(\Psi_{i-1}, \Psi_i, \Psi_{i+1}) + S_i \tag{3.1a}$$

$$q_i = \nabla^2 \Psi_i + \eta_i + f\left(1 + \delta_{i,3}\frac{h}{H}\right) \,, \tag{3.1b}$$

on the pressure levels at 200 hPa, 500 hPa and 800 hPa, denoted by the index $i = 1, 2, 3$, respectively. Here $\mathbf{q}$ denotes the potential vorticity, $\boldsymbol{\Psi}$ is the streamfunction, and $J(\cdot,\cdot)$ is the standard Jacobian operator. Furthermore, $\mathbf{D}$ represents temperature relaxation, Ekman friction, and hyperdiffusion, $\boldsymbol{\eta}$ denotes the stretching vorticity, f is the Coriolis parameter, and h/H is a normalized orography (cf.

Marshall and Molteni 1993). The constant vorticity forcing **S** is based on 10 northern hemispheric winter of ECMWF reanalysis data (Liu and Opsteegh 1995), which enables the model to simulate a realistic climatology.

The QG3LM uses a triangular spectral discretization of T21, leading to $N = 1449$ degrees of freedom. The time integration is done using a Leapfrog scheme with a time step of $\Delta t = 1/36$ days. For all following results a daily model output is used. Additionally, in all simulations the first 10 000 days are discarded to eliminate potential spinup effects.

Let $\mathbf{x} \in \mathbb{R}^N$ be the state vector as defined in (D.1). Then we can write the QG3LM shortly as

$$\frac{\mathrm{d}\mathbf{x}}{\mathrm{d}t} = \mathbf{G}(\mathbf{x})\,, \tag{3.2}$$

where $\mathbf{G}(\cdot)$ summarizes the right-hand side of (3.1a).

3.2 Semi-Empirical Model

We construct the semi-empirical low-order model (SEM) by projecting the QG3LM onto its EOFs (Preisendorfer 1988). In particular, the deviation of the state vector $\mathbf{x}'$ (1.10) is projected onto the leading M ($M < N$) EOFs:

$$\mathbf{x} = \langle \mathbf{x} \rangle + \mathbf{x}' \tag{3.3}$$

$$= \langle \mathbf{x} \rangle + a_k(t) e_k + \boldsymbol{\epsilon}(t) \tag{3.4}$$

$$= \langle \mathbf{x} \rangle + \mathbf{E}\mathbf{a}(t) + \boldsymbol{\epsilon}(t)\,, \tag{3.5}$$

where $\mathbf{a} \in \mathbb{R}^M$ is the so-called principle component vector[1], $\mathbf{E} \in \mathbb{R}^{N \times M}$ consists of the leading M EOFs $\mathbf{e} \in \mathbb{R}^N$ as columns, and $\boldsymbol{\epsilon} \in \mathbb{R}^N$ is the time-dependent truncation error.

The EOFs are defined by the eigenvalue problem (no Einstein's summation

---

[1] In the mathematical literature the EOF decomposition is called Principle Component Analysis.

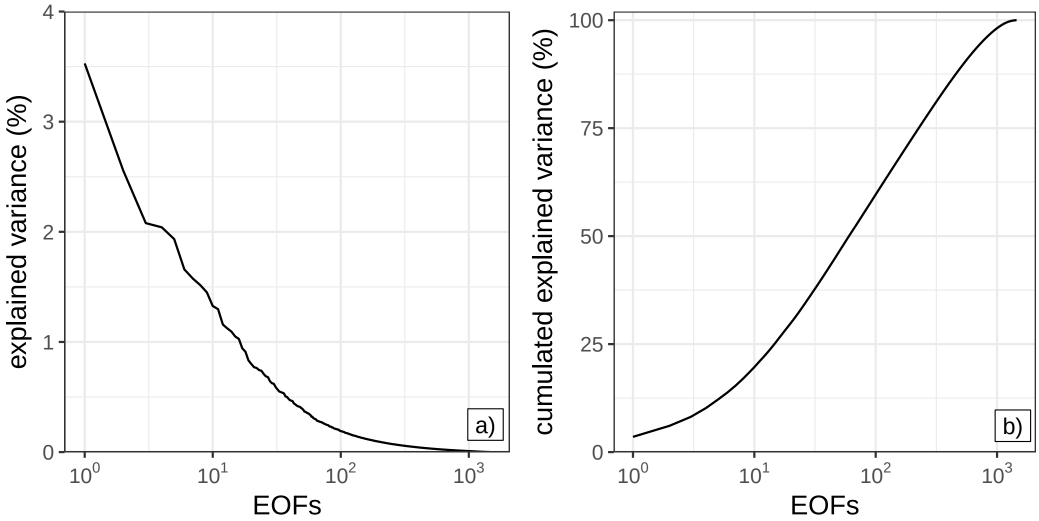

Figure 3.1: (a) Explained variance and (b) cumulative explained variance of the EOFs obtained from a 100 000 day time series of the QG3LM.

convention)

$$\left\langle \mathbf{x}'\mathbf{x}'^{\mathrm{T}} \right\rangle \mathsf{\mathbf{M}}\mathbf{e}_k = \lambda_k \mathbf{e}_k \,, \tag{3.6}$$

where the eigenvalue λ_k denotes the variance of the QG3LM explained by the kth EOF and $\mathsf{\mathbf{M}}$ is the total energy metric of Ehrendorfer (2000). The exact formulation of $\mathsf{\mathbf{M}}$ is given in appendix D.

Figure 3.1 shows the explained variance (Fig. 3.1a) and cumulative explained variance (Fig. 3.1b) of the EOFs, respectively, obtained by a 100 000 day integration of the QG3LM. Roughly 540 EOFs are necessary to explain 90% of the time series. This flatness of the spectrum is typical when applying an energy metric to data unfiltered in time (e.g., Achatz and Branstator 1999; Achatz and Opsteegh 2003a).

Applying the EOF decomposition (3.5) to the QG3LM (3.2) results in

$$\frac{\mathrm{d}\mathbf{a}}{\mathrm{d}t} = \mathsf{\mathbf{E}}^{\mathrm{T}}\mathsf{\mathbf{M}}\mathbf{G}\left(\langle \mathbf{x} \rangle + \mathsf{\mathbf{E}}\mathbf{a}\right) + \mathbf{s}(\mathbf{a}, \mathbf{x}) \,, \tag{3.7}$$

where the SGS tendency error $\mathbf{s}$ stems from the truncation within $\mathbf{G}(\cdot)$. To account for the SGS error, a suitable parameterization $\mathbf{p}(\mathbf{a})$ is required, which allows us to write the SEM as

$$\frac{\mathrm{d}\mathbf{a}}{\mathrm{d}t} = \tilde{\mathbf{G}}(\mathbf{a}) + \mathbf{p}(\mathbf{a}) + \boldsymbol{\epsilon}_p(\mathbf{a}, \mathbf{x}) \,, \tag{3.8}$$

where $\tilde{\mathbf{G}}(\mathbf{a}) = \mathbf{E}^{\mathrm{T}}\mathbf{M}\mathbf{G}(\langle \mathbf{x} \rangle + \mathbf{E}\mathbf{a})$ and $\boldsymbol{\epsilon}_p$ describes the error of the parameterization [i.e., $\boldsymbol{\epsilon}_p(\mathbf{a}, \mathbf{x}) = \mathbf{s}(\mathbf{a}, \mathbf{x}) - \mathbf{p}(\mathbf{a})$]. We choose a simple linear deterministic closure (Achatz and Branstator 1999; Achatz and Opsteegh 2003a) given by

$$\mathbf{p}_{\mathrm{det}}(\mathbf{a}) = \mathbf{r} + \mathbf{L}\mathbf{a} \,, \tag{3.9}$$

where $\mathbf{r} \in \mathbb{R}^M$ and $\mathbf{L} \in \mathbb{R}^{M \times M}$ are constant. The optimal closure parameters

$$\mathbf{L} = \langle \mathbf{s}'\mathbf{a}'^{\mathrm{T}} \rangle \langle \mathbf{a}'\mathbf{a}'^{\mathrm{T}} \rangle^{-1} \tag{3.10a}$$

$$\mathbf{r} = \langle \mathbf{s} \rangle - \mathbf{L}\langle \mathbf{a} \rangle \,, \tag{3.10b}$$

are obtained by minimizing $\langle \|\boldsymbol{\epsilon}_p\|^2 \rangle$ (appendix B.1), and the SGS tendency error is approximated by centered differences in time (B.3).

Furthermore, we consider a stochastic parameterization given by an OU-process

$$\mathbf{p}_{\mathrm{stoch}}(\mathbf{a}) = \mathbf{r} + \mathbf{L}\mathbf{a} + \boldsymbol{\Sigma}\dot{\mathbf{W}} \,, \tag{3.11}$$

where $\boldsymbol{\Sigma} \in \mathbb{R}^{M \times M}$ is diagonal and $\dot{\mathbf{W}}\mathrm{d}t = \mathrm{d}\mathbf{W} \in \mathbb{R}^M$ denotes a Wiener increment. The optimal closure parameters are estimated using the Maximum-Likelihood method (Honerkamp 1994). We obtain for the deterministic part exactly the same equations as (3.10), whereas the optimal noise amplitude is given by

$$\boldsymbol{\Sigma}_{ii} = \sqrt{2\Delta t \left\langle \left[s_i - (r_i + \sum_k \mathbf{L}_{ik} a_k) \right]^2 \right\rangle} \,, \tag{3.12}$$

(see appendix B.2). Thus, we write for the remainder of this thesis the SEM as

$$\frac{\mathrm{d}\mathbf{a}}{\mathrm{d}t} = \tilde{\mathbf{G}}(\mathbf{a}) + \mathbf{r} + \mathbf{L}\mathbf{a} + \boldsymbol{\Sigma}\dot{\mathbf{W}} \,, \tag{3.13}$$

where in the case of the deterministic closure $\boldsymbol{\Sigma} = 0$ (SEM$_{\mathrm{det}}$) and for the stochastic

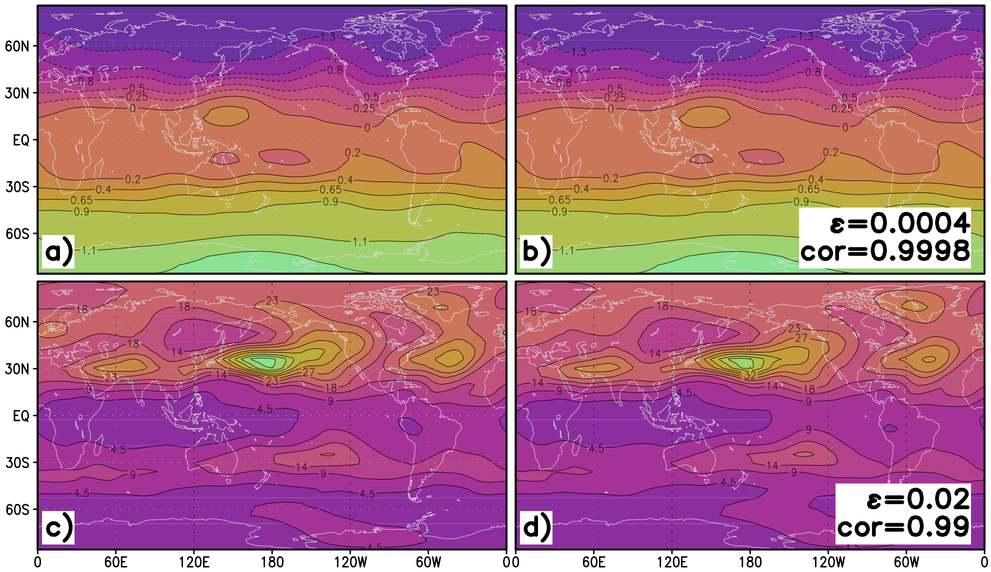

Figure 3.2: (a),(b) Mean streamfunction ($10^8\,\mathrm{m}^2\,\mathrm{s}^{-1}$) and (c),(d) covariance of streamfunction ($10^{13}\,\mathrm{m}^4\,\mathrm{s}^{-2}$) at 200 hPa. (a),(c) The result of the QG3LM projected onto the first 500 EOFs; (b),(d) the result of the 500 EOF $\mathrm{SEM}_{\mathrm{det}}$. The variable ε denotes the relative error in (5.1) and "cor" is the pattern correlation calculated between the $\mathrm{SEM}_{\mathrm{det}}$ and the QG3LM, respectively. Note that the color shading is adjusted and the same units are used for each row (Pieroth et al. 2018, ©American Meteorological Society. Used with permission).

parameterization $\mathbf{\Sigma}$ ($\mathrm{SEM}_{\mathrm{stoch}}$) is given by (3.12).

In general, such semi-empirical low-order models tend to overestimate the variance (Achatz and Branstator 1999; Achatz and Opsteegh 2003a). To counter this, we adjust the hyperdiffusion by changing the diffusion time scale τ_H (see Marshall and Molteni 1993) to minimize the relative error [see (5.1) in section 5.1] of the variance between the QG3LM and the SEM. The numerical values for both parameterizations are given in Table 3.1.

Figure 3.2 shows the mean (top) and covariance of the streamfunction (bottom), respectively, of the 500 EOF $\mathrm{SEM}_{\mathrm{det}}$ (Figs. 3.2b and 3.2d) in comparison to the QG3LM (Figs. 3.2a and 3.2c). Both models are evaluated at 200 hPa, since for the anomaly experiments the strongest response is evident in this layer. In addition, the QG3LM has been projected on the first 500 EOFs to allow a fair comparison. In general, the parameterization works quite well: The mean is vir-

Table 3.1: Adjusted diffusion time scale (days) that is used in the SEM. The original value is $\tau_H = 2$ days. (Pieroth et al. 2018, ©American Meteorological Society. Used with permission).

number of EOFs	SEM$_{\text{det}}$ τ_H	SEM$_{\text{stoch}}$ τ_H
20	1.0	0.4
50	1.3	0.6
100	1.2	0.6
200	1.9	1.1
500	2.6	2.2

tually identical[2], and in the covariance only small differences in the amplitude are visible. For smaller EOF truncations and the SEM$_{\text{stoch}}$ the results are qualitatively the same (not shown).

---

[2] This is to be expected, since for an unforced case the EOFs have per definition no mean. Thus, both figures show essentially $\langle \mathbf{x} \rangle$ of (3.5).

Chapter 4

Climate-Dependent Subgrid-Scale Parameterization

4.1 Anomalous Forcings

In the following we introduce the external forcings used to perturb the models. Additionally, we specify the anomalous SEM and explain the role of the FDT to update the tuning parameters of the SGS closure.

4.1.1 Local Forcing

The SEM reproduces the QG3LM qualitatively and quantitatively. However, so far we only considered an unperturbed setting. For a final evaluation of the SEM performance we have to perturb the system. For this we consider a time-independent local forcing that simulates the effect of a sea-surface temperature anomaly caused by a change in the oceanic circulation (Branstator and Haupt 1998; Achatz and Branstator 1999; Achatz and Opsteegh 2003b; Achatz et al. 2013).

In terms of a quasigeostrophic potential vorticity forcing this anomalous heating

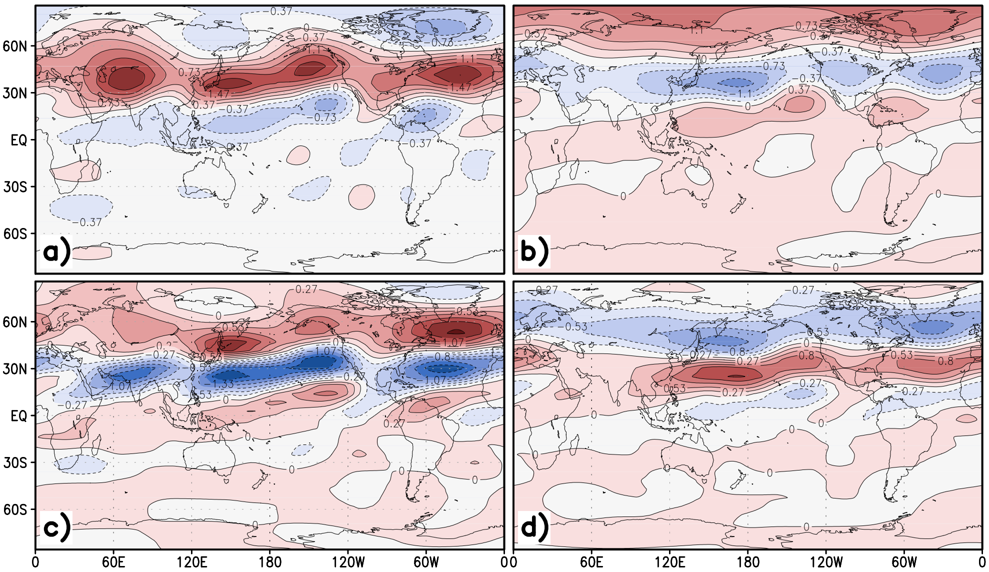

Figure 4.1: Response of the QG3LM at 200 hPa resulting from the local anomalous forcing at $\lambda_c = 60°$ in (a) mean streamfunction ($10^6\,\mathrm{m}^2\,\mathrm{s}^{-1}$) and (c) zonal wind ($\mathrm{m\,s}^{-1}$). (b),(d) The response caused by the global anomalous forcing using the first EOF. The color shading is adjusted and the same units are used for each row (Pieroth et al. 2018, ©American Meteorological Society. Used with permission).

reads

$$\delta S_i = -\frac{AR\Delta p}{f_0}\left[(1-\delta_{i,3})\frac{\sin\left(\frac{\pi p_{i+\frac{1}{2}}}{p_s}\right)}{r^2_{i+\frac{1}{2}}p_{i+\frac{1}{2}}} - (1-\delta_{i,1})\frac{\sin\left(\frac{\pi p_{i-\frac{1}{2}}}{p_s}\right)}{r^2_{i-\frac{1}{2}}p_{i-\frac{1}{2}}}\right] \times \cos^2\left(\frac{\lambda-\lambda_c}{\Delta\lambda}\right)\cos^2\left(\frac{\phi-\phi_c}{\Delta\phi}\right), \tag{4.1}$$

where the amplitude $A = 1.25$ K day^{-1}, R denotes the universal gas constant, $\Delta p = 300\,\mathrm{hPa}$ is the pressure difference of the respective layers, $p_s = 1000\,\mathrm{hPa}$ denotes the surface pressure, $f_0 = 2\sin(45°)$ is the Coriolis parameter, and λ_c, ϕ_c is the position at which the anomalous forcing is centered. Furthermore, $\Delta\lambda = \Delta\phi = 20°$ denotes the extension of the forcing (i.e., for $\phi \notin [\phi_c - \Delta\phi/2, \phi_c + \Delta\phi/2]$ and $\lambda \notin [\lambda_c - \Delta\lambda/2, \lambda_c + \Delta\lambda/2]$ $\delta\mathbf{S}$ is set to zero). The pressure between the layers is given by $p_{1\frac{1}{2}} = 350\,\mathrm{hPa}$ and $p_{2\frac{1}{2}} = 650\,\mathrm{hPa}$. Finally, r denotes the Rossby radius of deformation (see Marshall and Molteni 1993, for the numerical values).

In accordance to Achatz et al. (2013) we place the anomalous forcing in the extratropics, since the equatorial region of the QG3LM exhibits only a relatively small variance. Consequently, any forcing placed there would be poorly resolved by the EOFs. Therefore, we fix the latitute at $\phi_c = 45°$ and vary the longitude position by $\lambda_c = \{0°, 30°, \ldots, 330°\}$. Strictly speaking this violates our physical interpretation of the forcing as a heating coming from the ocean, because the QG3LM has a crude representation of orography (Marshall and Molteni 1993). Nevertheless, since the QG3LM is an atmosphere-only model it makes no difference where the forcing is placed.

The left column of Fig. 4.1 shows the steady-state response of the QG3LM at 200 hPa, caused by an anomalous forcing placed at $\lambda_c = 60°$ and calculated from a time series of 6×10^6 days. The forcing has been projected onto the first 20 EOFs. Fig. 4.1a shows the response of the mean streamfunction, Fig. 4.1c that of the mean zonal wind. The peak wind speeds of about $2\,\mathrm{m\,s^{-1}}$ are comparable to what is the expected response of the climate because of the anthropogenic influence (Lorenz and DeWeaver 2007).

4.1.2 Global Forcing

It is quite an approximation to simulate a climate change by a localized heat source in the extratropics. Intuitively we would expect a global forcing due to the climate change. Therefore, to drop the locality and thus be more realistic, we additionally consider a global anomalous forcing. In particular, we construct a dynamic forcing given by individual EOFs multiplied by suitable factors:

$$\delta\mathbf{f} = \varepsilon_k \mathbf{e}_k \,, \tag{4.2}$$

where $\varepsilon_k > 0$ with $k = 1, 2, \ldots, 5$. The ε_k are chosen in a way that the turbulent kinetic energy $\mathbf{x}'^{\mathrm{T}}\mathbf{M}\mathbf{x}'$ of the response is comparable to the response caused by the local forcing ($E_{\mathrm{turb}} \approx 470\,\mathrm{TJ\,kg^{-1}}$). Their exact values are given in Table 4.1.

Figures 4.1b and 4.1d show, as a representative example, the response of the global anomalous forcing using EOF 1. The response is similar to the one of the local forcing (Figs. 4.1a and 4.1c). However, the amplitude is weaker with maximum mean zonal wind speeds of about $1.5\,\mathrm{m\,s^{-1}}$.

Table 4.1: Constant factors used for the calculation of the global anomalous forcing. The values are given in units of $4\Omega^2$, where $\Omega = 2\pi$ day^{-1} (Pieroth et al. 2018, ©American Meteorological Society. Used with permission).

ε_1	ε_2	ε_3	ε_4	ε_5
$\frac{1}{\sqrt{45}} \cdot 10^{-5}$	$\frac{1}{\sqrt{10}} \cdot 10^{-5}$	$\frac{1}{\sqrt{3}} \cdot 10^{-5}$	$\frac{1}{2} \cdot 10^{-5}$	$\frac{1}{\sqrt{2}} \cdot 10^{-5}$

4.2 Anomalous Semi-Empirical Model

The simplest approach to incorporate the anomalous forcing in the semi-empirical low-order model is the so-called a priori SEM (apr-SEM; i.e., the naïve SEM):

$$\frac{\mathrm{d}\mathbf{a}}{\mathrm{d}t} = \tilde{\mathbf{G}}(\mathbf{a}) + \mathbf{r} + \mathsf{L}\mathbf{a} + \mathbf{\Sigma}\dot{\mathbf{W}} + \delta\mathbf{f}, \tag{4.3}$$

where $\delta\mathbf{f}$ is either given by $\delta\mathbf{f} = \mathsf{E}_{20}^{\mathrm{T}}\mathsf{M}\delta\mathbf{S}$ (where E_{20} denotes the projection on the first 20 EOFs) in case of the local anomalous forcing or by (4.2) for the global anomalous forcing. However, the apr-SEM fails to reproduce a correct response, as can be seen on the example of the local anomalous forcing at $\lambda_c = 270°$ (Fig. 5.2b). The 500 apr-SEM has minima over the oceans which are too weak, while the position of the maximum response is shifted to the west and is too pronounced in comparison to the true response (Fig. 5.2a). This incorrect response is caused by the empirical closure being tuned to the unperturbed case (Achatz et al. 2013; Pieroth et al. 2018).

The actual forced SEM should read

$$\frac{\mathrm{d}\mathbf{a}}{\mathrm{d}t} = \tilde{\mathbf{G}}(\mathbf{a}) + \mathbf{r} + \delta\mathbf{r} + (\mathsf{L} + \delta\mathsf{L})\mathbf{a} + (\mathbf{\Sigma} + \delta\mathbf{\Sigma})\dot{\mathbf{W}} + \delta\mathbf{f}\,, \tag{4.4}$$

where $\delta\mathbf{r}, \delta\mathsf{L}$ and $\delta\mathbf{\Sigma}$ are the changes in the SGS parameterization caused by the forcing. The updated parameters are given by

$$\mathsf{L} + \delta\mathsf{L} = \left(\langle \mathbf{s}'\mathbf{a}'^{\mathrm{T}} \rangle + \delta\langle \mathbf{s}'\mathbf{a}'^{\mathrm{T}} \rangle\right) \left(\langle \mathbf{a}'\mathbf{a}'^{\mathrm{T}} \rangle + \delta\langle \mathbf{a}'\mathbf{a}'^{\mathrm{T}} \rangle\right)^{-1} \tag{4.5a}$$

$$\mathbf{r} + \delta\mathbf{r} = \langle \mathbf{s} \rangle + \delta\langle \mathbf{s} \rangle - (\mathsf{L} + \delta\mathsf{L})\left(\langle \mathbf{a} \rangle + \delta\langle \mathbf{a} \rangle\right) \tag{4.5b}$$

$$
\begin{aligned}
&\boldsymbol{\Sigma}_{ii} + \delta\boldsymbol{\Sigma}_{ii} = \\
&\quad \sqrt{2\Delta t}\Bigg([\langle s_i^2\rangle + \delta\langle s_i^2\rangle] + \sum_{k,j} \left(\mathsf{L}_{ik} + \delta\mathsf{L}_{ik}\right)\left(\mathsf{L}_{ij} + \delta\mathsf{L}_{ij}\right)\left(\langle a_k a_j\rangle + \delta\langle a_k a_j\rangle\right) \\
&\qquad - 2\left[\left(r_i + \delta r_i\right)\left(\langle s_i\rangle + \delta\langle s_i\rangle\right) + \sum_{k} \left(\mathsf{L}_{ik} + \delta\mathsf{L}_{ik}\right)\left(\langle s_i a_k\rangle + \delta\langle s_i a_k\rangle\right)\right] \\
&\qquad + \left(r_i + \delta r_i\right)^2 + 2\sum_{k} \left(\mathsf{L}_{ik} + \delta\mathsf{L}_{ik}\right)\left(r_i + \delta r_i\right)\left(\langle a_k\rangle + \delta\langle a_k\rangle\right)\Bigg)^{\frac{1}{2}} , \qquad (4.5c)
\end{aligned}
$$

where $\delta\langle \mathbf{s}'\mathbf{a}'^{\mathrm{T}}\rangle = \delta\langle \mathbf{s}\mathbf{a}^{\mathrm{T}}\rangle - \delta\langle \mathbf{s}\rangle\delta\langle \mathbf{a}\rangle^{\mathrm{T}}$ and $\delta\langle \mathbf{a}'\mathbf{a}'^{\mathrm{T}}\rangle = \delta\langle \mathbf{a}\mathbf{a}^{\mathrm{T}}\rangle - \delta\langle \mathbf{a}\rangle\delta\langle \mathbf{a}\rangle^{\mathrm{T}}$. Therefore, if the changes in the statistical moments (i.e., $\delta\langle \mathbf{a}\rangle, \delta\langle \mathbf{s}\rangle, \delta\langle s_i^2\rangle, \delta\langle \mathbf{a}\mathbf{a}^{\mathrm{T}}\rangle$, and $\delta\langle \mathbf{s}\mathbf{a}^{\mathrm{T}}\rangle$) are known, it would be easy to update the empirical parameters of the SGS closure.

The changes in the statistical moments can be obtained by a time series of the perturbed reference model. Obviously, the response of the resulting a posteriori SEM (apo-SEM; Fig. 5.2c) is significantly improved compared to the apr-SEM (Fig. 5.2b). Nevertheless, running a high-dimensional reference model each time when conducting sensitivity studies defies the purpose of low-order modeling.

For realistic climate projections it is impossible to compute the true response. Thus, usually the tuning parameters are kept constant. However, we propose using the qG-FDT (2.30) to estimate the required response of the statistical moments (Achatz et al. 2013; Pieroth et al. 2018). In particular, if the model is forced by $\delta\mathbf{f} = const.$, we approximate $\delta\langle \mathbf{s}\rangle$ by

$$
\delta\langle \mathbf{s}\rangle = \int_0^\infty \left\langle \mathbf{s}(\mathbf{a}[t+\tau])\mathbf{a}'^{\mathrm{T}}(t)\right\rangle \boldsymbol{\Sigma}^{-1}(0)\mathrm{d}\tau\delta\mathbf{f}\,. \qquad (4.6)
$$

The change of the remaining statistical moments (i.e., $\delta\langle \mathbf{a}\rangle, \delta\langle s_i^2\rangle, \delta\langle \mathbf{a}\mathbf{a}^{\mathrm{T}}\rangle$, and $\delta\langle \mathbf{s}\mathbf{a}^{\mathrm{T}}\rangle$) can be estimated analogously. In return, these estimations are then used to update the tuning parameters (4.5). Of course, this estimation will not be perfect because of the limitations of the theorem. Nevertheless, we expect to see a positive effect under appropriate conditions.

Chapter 5

Results

The results are structured as follows. First we introduce the experimental setup. Afterwards, we conduct the anomaly experiments with both the local and global external forcing, respectively. Furthermore, we investigate the performance of the $\text{SEM}_{\text{stoch}}$ and the superior ST/qG-FDT algorithm. Most of the results presented in this section are published in Pieroth et al. (2018).

5.1 Setup

In the following simulations we consider a local anomalous forcing and a global anomalous forcing, which are both presented in section 4.1. The former uses 12 different forcing positions, while the latter considers one of the first five EOFs as forcing patterns. In each integration the first 10 000 days have been discarded to eliminate potential spinup effects. Furthermore, we are focusing the investigation on the 200 hPa layer, since there the strongest response is visible. The results are quantified by a relative error in EOF space given by

$$\varepsilon(\mathbf{a},\mathbf{b}) = \frac{\| \mathbf{a} - \mathbf{b} \|^2}{\| \mathbf{a} \| \| \mathbf{b} \|} \qquad \text{and} \qquad \varepsilon(\mathsf{A},\mathsf{B}) = \frac{\| \mathsf{A} - \mathsf{B} \|^2}{\| \mathsf{A} \| \| \mathsf{B} \|}, \tag{5.1}$$

where the norm $\| \cdot \|$ is either the 2-norm (for $\mathbf{a}, \mathbf{b} \in \mathbb{R}^M$) or the Frobenius norm (for $\mathsf{A}, \mathsf{B} \in \mathbb{R}^{M \times M}$).

For the FDT experiments we consider four different SEM configurations:

- apr-SEM: Using the original (a priori) parameterization of the unforced case (4.3). This simulates the state-of-the-art case of using a GCM for sensitivity studies without retuning any empirical parameters.
- apo-SEM: Using the perfect (a posteriori) parameterization by retuning the empirical parameters to the perturbed time series (impossible in realistic settings).
- FDT-SEM: Updating the parameterization with the help of the qG-FDT.
- rFDT-SEM: Updating the parameterization with the help of the rqG-FDT of Achatz et al. (2013) (i.e., ignoring the second order moment updates).

Each model uses a time series of length 6×10^6 days. Strictly speaking, this huge amount of data is not necessary (see discussion in section 5.2), however, we want to avoid sampling errors and potential spurious linear-response effects (Gottwald et al. 2016). Furthermore, we restrict our investigation on five different EOF truncations, given by 20 (30% explained variance), 50 (46%), 100 (60%), 200 (73%), and 500 (89%) EOFs, respectively.

The experiments are conducted for both the $\mathrm{SEM}_{\mathrm{det}}$ and $\mathrm{SEM}_{\mathrm{stoch}}$. As it turns out, the qG-FDT predicted correction of the noise amplitude $\delta\mathbf{\Sigma}$ is not useful for the local anomalous forcing. We could set $\delta\mathbf{\Sigma} = 0$, however, this would potentially mask the positive (or negative) effect of the update of the remaining empirical parameters of the SGS closure. Thus, for the local anomalous forcing we restrict our investigation only on the $\mathrm{SEM}_{\mathrm{det}}$.

5.2 Numerical Experiments

5.2.1 Local Anomalous Forcing

Figure 5.1a shows for different EOF truncations a boxplot of relative error between the qG-FDT and the a posteriori statistical moments required for the calculation of the SEM's SGS closure (3.10) and (3.12), respectively. Obviously, the qG-FDT is unable to estimate $\delta\langle s_i^2\rangle$ correctly, regardless of the EOF truncation. In particular, for the 500 EOF case the median of relative error reaches $\mathcal{O}(1)$. Furthermore,

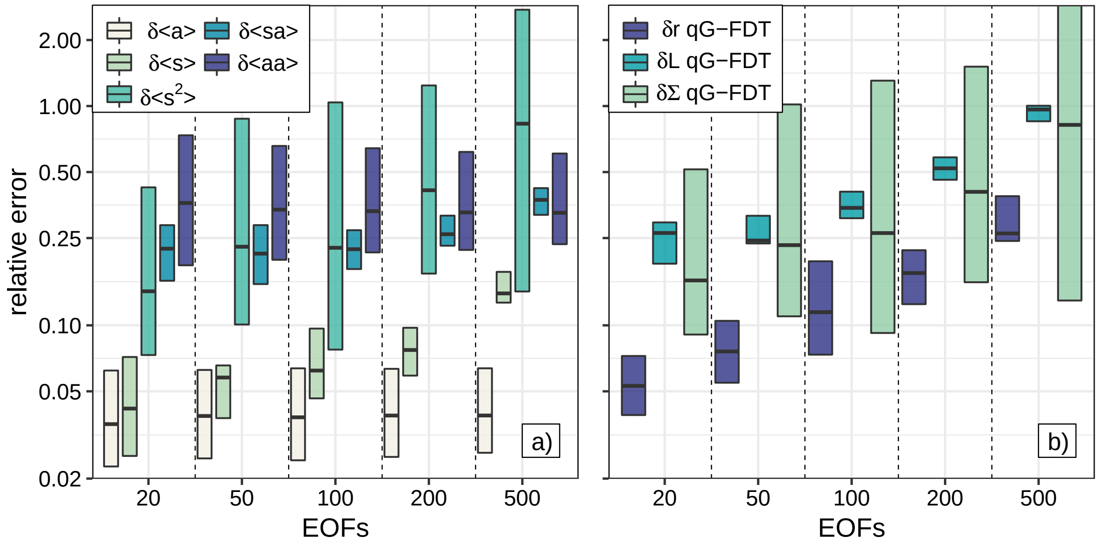

Figure 5.1: Boxplot of (a) the relative error between the qG-FDT and the true response of the moments and (b) a posteriori closure corrections to the local anomalous forcing, against the number of EOFs. The statistics for the boxplot come from the different forcing positions $\lambda_c \in \{0°, 30°, \dots, 330°\}$. The median is given by the horizontal black line and the colored area denotes the interquartile range (25th–75th percentiles; Pieroth et al. 2018, ©American Meteorological Society. Used with permission).

this moment experiences a significant spread. Yet, the first moments (i.e., $\delta\langle\mathbf{a}\rangle$ and $\delta\langle\mathbf{s}\rangle$) are remarkably well estimated with an average median of about $\varepsilon \approx 0.05$. In contrast, the second moments (i.e., $\delta\langle\mathbf{aa}^{\mathrm{T}}\rangle$ and $\delta\langle\mathbf{sa}^{\mathrm{T}}\rangle$) show a systematically higher relative error of $\varepsilon \approx 0.25$. Moreover, we see a trend in the moments containing the SGS error (i.e. $\delta\langle\mathbf{s}\rangle, \delta\langle s_i^2\rangle$, and $\delta\langle\mathbf{sa}^{\mathrm{T}}\rangle$) with increasing errors for higher EOF truncations. This trend directly translates into the closure corrections (Fig. 5.1b). Overall, the estimation of $\delta\mathbf{r}$ has the lowest errors ranging from $\varepsilon = 0.05$ to $\varepsilon = 0.25$. In contrast, the errors of $\delta\mathsf{L}$ are significantly higher with $\varepsilon = 0.25$ to $\varepsilon = 1$. However, the spread of $\delta\mathsf{L}$ is considerably lower than that of $\delta\mathbf{r}$. This result is unsurprising given the fact that $\delta\mathsf{L}$ is directly dependent on the second moments and $\delta\mathbf{r}$ depends on $\delta\mathsf{L}$ (4.5). For the same reason the incorrect estimation of $\delta\langle s_i^2\rangle$ renders $\delta\boldsymbol{\Sigma}$ useless.

For the evaluation of the closure corrections obtained by the qG-FDT we first consider, as an example, a 500 EOF SEM$_{\mathrm{det}}$, perturbed by a local anomalous

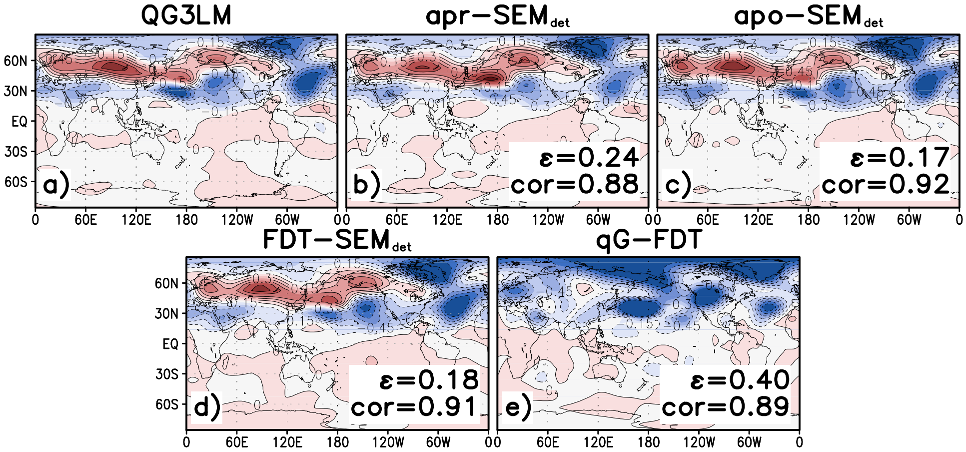

Figure 5.2: Response in covariance of streamfunction ($10^{13}\,\mathrm{m}^4\,\mathrm{s}^{-2}$) at 200 hPa resulting from a local anomalous forcing located at $\lambda_c = 270°$. (a) The response of the QG3LM projected onto 500 EOFs. The response of the 500 EOF (b) apr-SEM$_{\mathrm{det}}$, (c) apo-SEM$_{\mathrm{det}}$, and (d) FDT-SEM$_{\mathrm{det}}$. (e) For comparison the direct qG-FDT estimation of the response in covariance of streamfunction is given. The variable ε denotes the relative error in (5.1) and "cor" is the pattern correlation calculated between the low-order model and the QG3LM, respectively (Pieroth et al. 2018, ©American Meteorological Society. Used with permission).

forcing at $\lambda_c = 270°$. Figure 5.2 shows the response in covariance of streamfunction for the QG3LM (Fig. 5.2a), various SEM$_{\mathrm{det}}$ (Figs. 5.2b-d), and the direct qG-FDT estimation using the response operator for var(Ψ) (Fig. 5.2e). The QG3LM experiences multiple minima over the oceans and a large minimum over Greenland. Additionally, we observe a band of maxima at roughly 50°N spanning nearly the whole globe with a local maximum over Asia. In contrast, for the apr-SEM$_{\mathrm{det}}$ (Fig. 5.2b) the amplitudes of the minima over the oceans are too weak while the minimum over Greenland is too strong. Furthermore, the local maximum is shifted to the Pacific Ocean. Consequently, the relative error reads $\varepsilon = 0.24$ and the correlation is below 90%. Most of these deficits are directly linked to incorrect tuning: the relative error decreases to $\varepsilon = 0.18$ for the apo-SEM$_{\mathrm{det}}$ (Fig. 5.2c). In particular, the minima over the oceans have a more realistic amplitude and the position of the local maximum over Asia is well captured. However, the amplitude of the minimum over Greenland is even worse than that of the apr-SEM$_{\mathrm{det}}$. Similar results are obtained by the FDT-SEM$_{\mathrm{det}}$ (Fig. 5.2d), which is

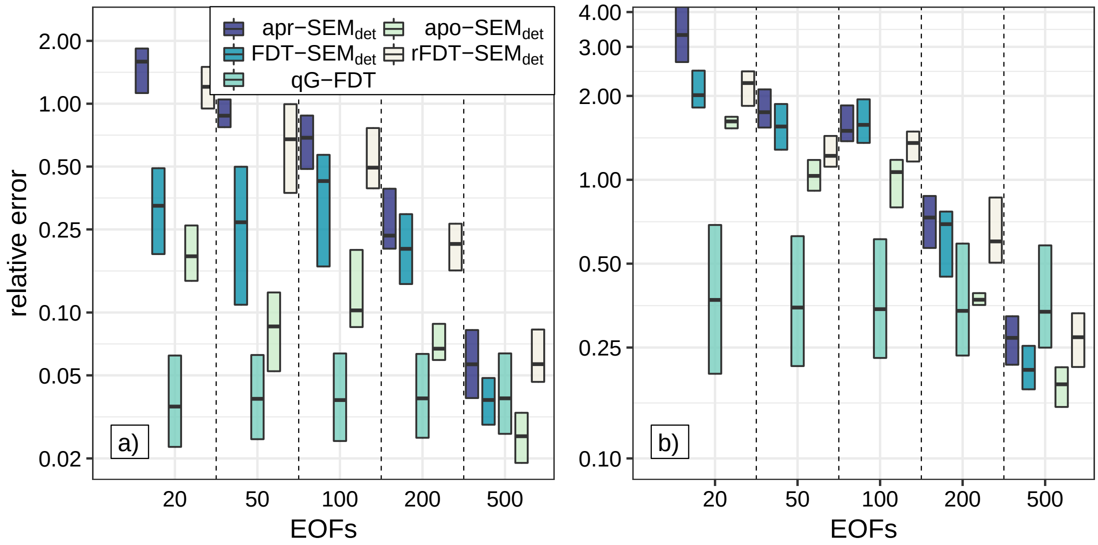

Figure 5.3: Boxplot of the relative error of the response of (a) the first moment and (b) covariance of streamfunction between the SEM$_{\text{det}}$ with adjusted closures and the QG3LM with local anomalous forcing against the number of EOFs. For comparison also the direct qG-FDT estimation of the respective moment is plotted. The statistics for the boxplot come from the different forcing positions $\lambda_c \in \{0°, 30°, \dots, 330°\}$ (Pieroth et al. 2018, ©American Meteorological Society. Used with permission).

also visible by the nearly identical relative error of $\varepsilon = 0.17$. On the other hand, the direct qG-FDT estimation of the response of covariance of streamfunction fails completely. While the pattern of the response is captured quite well ($cor = 0.89$), the amplitude is orders of magnitudes too high. In addition, the direct qG-FDT response shows only a negative response throughout the northern hemisphere resulting in a relative error of $\varepsilon = 0.40$. Similar results are obtained for the response in mean streamfunction (not shown).

Figure 5.3 shows the summarizing evaluation of the FDT-SEM$_{\text{det}}$ for all forcing positions and EOF truncations. In particular, Fig. 5.3 shows the boxplot of relative error of the various SEM$_{\text{det}}$ for the response in mean streamfunction (Fig. 5.3a) and the response in covariance of streamfunction (Fig. 5.3b). In addition to the models in the example case above we are also considering the rFDT-SEM$_{\text{det}}$, which is the originally proposed ansatz of Achatz et al. (2013). In principle, we see the same behavior as described in the detailed example, for all EOF truncations

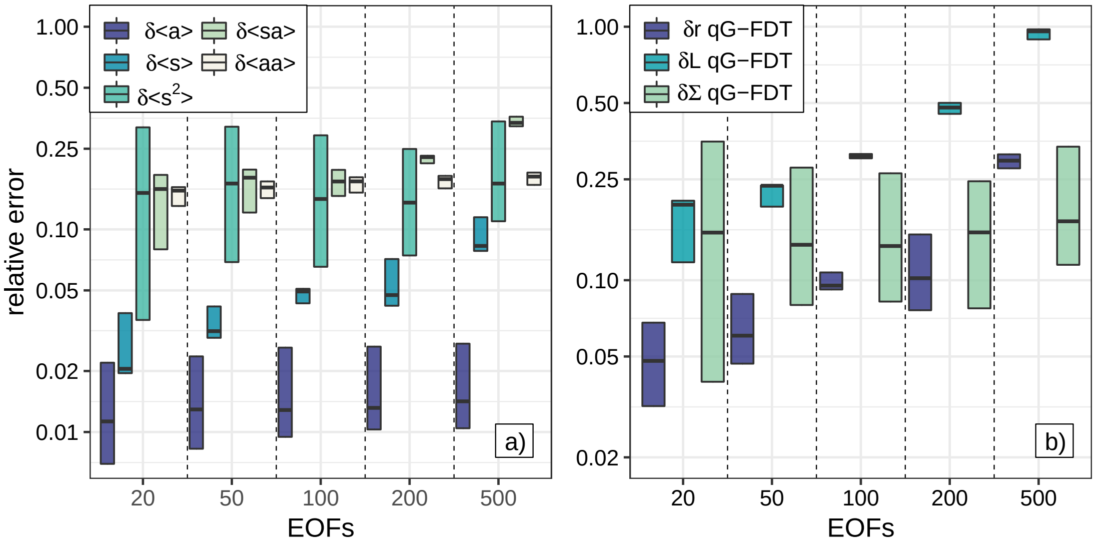

Figure 5.4: As in Fig. 5.1, but for the global anomalous forcings represented by EOFs $\mathbf{e}_k$ with $k \in \{1, 2, \ldots, 5\}$. For comparison with the local anomalous forcing case, the results are shown as a boxplot (Pieroth et al. 2018, ©American Meteorological Society. Used with permission).

and forcing cases: the FDT-SEM$_{\mathrm{det}}$ outperforms the apr-SEM$_{\mathrm{det}}$. The rFDT-SEM$_{\mathrm{det}}$, on the other hand, provides only a slight improvement over the a priori SEM$_{\mathrm{det}}$ for the response in mean streamfunction (Fig. 5.3a). For the response in covariance of streamfunction (Fig. 5.3b) the rFDT-SEM$_{\mathrm{det}}$ produces comparable results to the FDT-SEM$_{\mathrm{det}}$ for the 20 EOF, 50 EOF, and 100 EOF case, but does a poorer job for the higher EOF truncations. Furthermore, for both mean and covariance of streamfunction the direct application of the qG-FDT operator outperforms all SEM$_{\mathrm{det}}$ (including the apo-SEM$_{\mathrm{det}}$) for all EOF truncations smaller 200 EOF.

5.2.2 Global Anomalous Forcing

Figure 5.4 shows the performance of the qG-FDT for the case of the global anomalous forcing. The major results of the local anomalous forcing case are reproduced. In particular, $\delta\langle s_i^2\rangle$ still experiences the highest spread. Yet, the overall quality of the qG-FDT estimations (Fig. 5.4a) are significantly improved. The median of the highest error among all moments and all EOF truncations is at $\varepsilon \approx 0.3$. On the

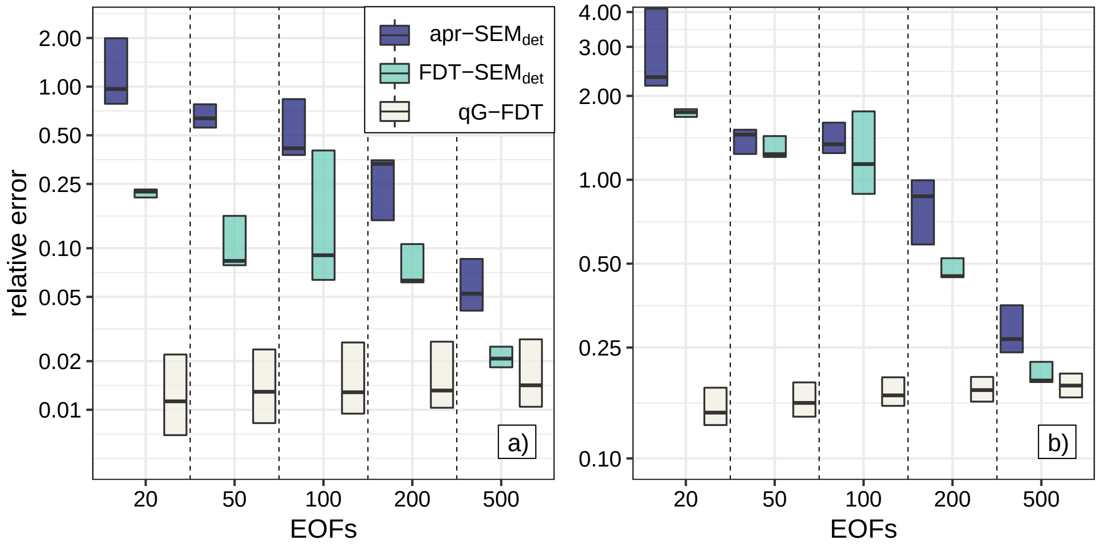

Figure 5.5: As in Fig. 5.3, but for the global anomalous forcings represented by EOFs $\mathbf{e}_k$ with $k \in \{1, 2, \ldots, 5\}$. For comparison with the local anomalous forcing case, the results are shown as a boxplot (Pieroth et al. 2018, ©American Meteorological Society. Used with permission).

other hand, the resulting closure corrections (Fig. 5.4b) are seemingly identical to that of the local anomalous forcing case (Fig. 5.1b). The only exception being $\delta\boldsymbol{\Sigma}$ which has on average a median of $\varepsilon \approx 0.2$, because of the skillful $\delta\langle s_i^2\rangle$ estimation. On close inspection we see that the quality of the estimation of $\delta\langle \mathbf{s}\mathbf{a}^{\mathrm{T}}\rangle$ for both the local anomalous forcing (Fig. 5.1a) and the global anomalous forcing (Fig. 5.4a) is nearly identical. This indicates that the closure corrections are highly sensitive towards this specific moment.

Consequently, for the global anomalous forcing the performance of the FDT-SEM$_{\mathrm{det}}$ (Fig. 5.5) is somewhat similar to the case of the local anomalous forcing (Fig. 5.3). Not only qualitatively but also quantitatively the result for both the response in mean streamfunction (Fig. 5.5a) and covariance of streamfunction (Fig. 5.5b) is quite similar. We notice, however, that the spread of all SEM$_{\mathrm{det}}$ and the direct application of the qG-FDT response operator is considerably reduced in the case of the global anomalous forcing. This might be a consequence of the reduced number of forcing cases, which are less than half compared to the local anomalous forcing.

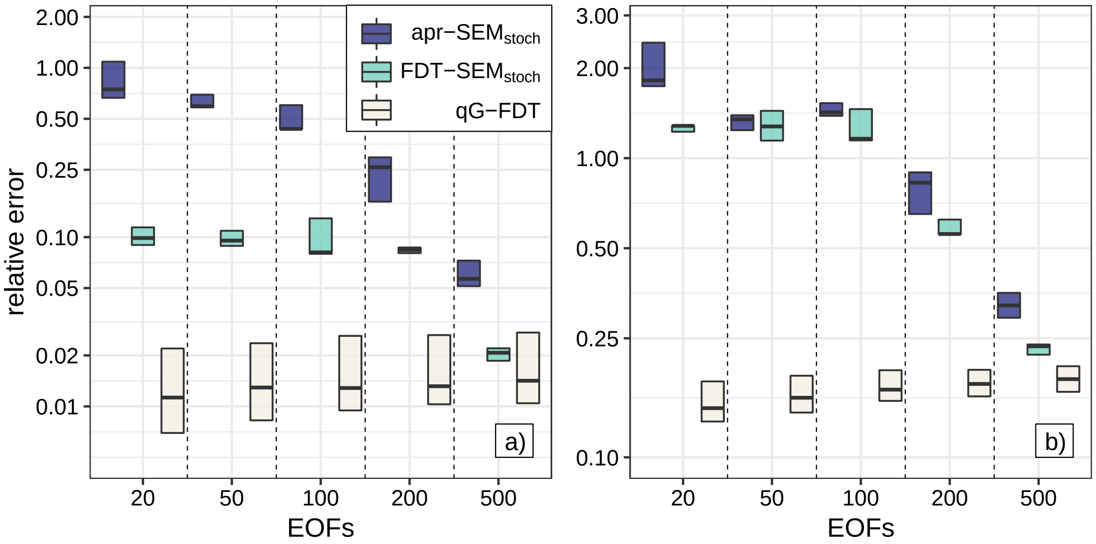

Figure 5.6: As in Fig. 5.5, but for the SEM$_{\text{stoch}}$ (Pieroth et al. 2018, ©American Meteorological Society. Used with permission).

Because of the skillful estimations of $\delta\boldsymbol{\Sigma}$ we are able to investigate the FDT-SEM$_{\text{stoch}}$ in the global anomalous forcing case. In Fig. 5.6 the equivalent evaluation as in Fig. 5.5 is shown, however, for SEM$_{\text{stoch}}$. In principle, the previous results are supported: the qG-FDT is able to successfully update the empirical parameters of the SGS closure such that the FDT-SEM$_{\text{stoch}}$ systematically outperforms the apr-SEM$_{\text{stoch}}$. In contrast to the SEM$_{\text{det}}$ (Fig. 5.5) we find that the response of both the apr-SEM$_{\text{stoch}}$ and FDT-SEM$_{\text{stoch}}$ experience a reduced variability with respect to the global anomalous forcing. However, in terms of the median of relative error no benefit is visible from the additional stochasticity in the SEM.

5.2.3 Blended short-time/quasi-Gaussian Fluctuation-Dissipation Theorem

In order to evaluate the impact of the assumption of Gaussianity made by the qG-FDT, we additionally apply the blended ST/qG-FDT of Abramov and Majda (2007) to the 20 EOF and 200 EOF case with a local anomalous forcing. For the blending we choose a $\tau_* = 2$ days, which was determined by trial and error (i.e., by comparison of the response of the qG-FDT and the ST-FDT for various τ_*). Figure

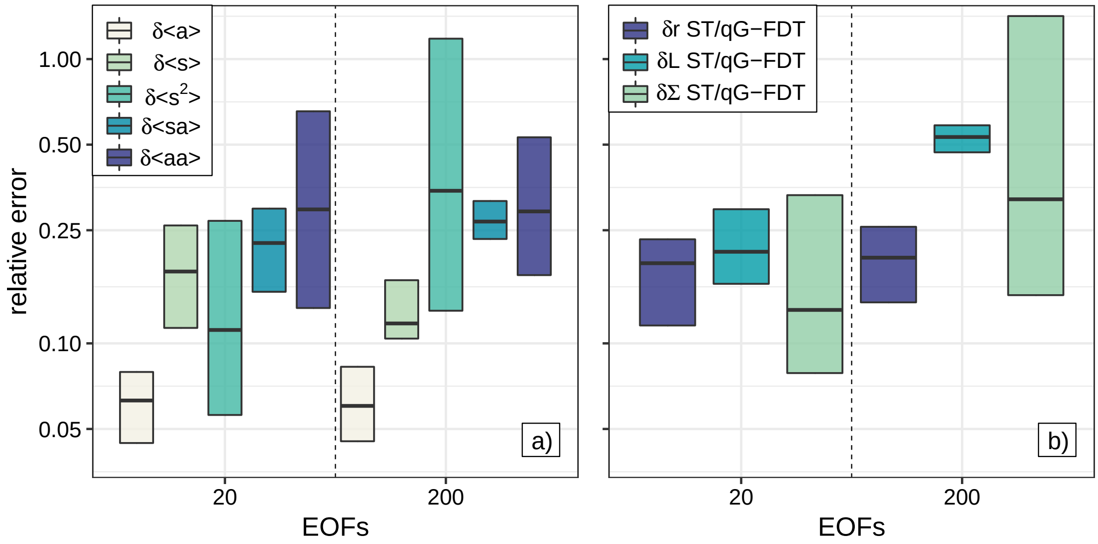

Figure 5.7: As in Fig. 5.1, but showing the result of the ST/qG-FDT algorithm (Pieroth et al. 2018, ©American Meteorological Society. Used with permission).

5.7a shows the estimation of the changes of the statistics by the blended algorithm. The result is qualitatively similar to the qG-FDT (Fig. 5.1a). The first moments are considerably better estimated than the second moments and $\delta\langle s_i^2\rangle$ experiences the highest spread. Quantitatively only slight improvements, mainly in spread, are visible for both $\delta\langle s_i^2\rangle$ and $\delta\langle \mathbf{aa}^\mathrm{T}\rangle$. In contrast, the error of $\delta\langle \mathbf{s}\rangle$ estimated by the blended algorithm is considerably higher. Consequently, no improvement is made in the closure corrections (Fig. 5.7b). In fact, because of the higher error in $\delta\langle \mathbf{s}\rangle$ the quality of $\delta\mathbf{r}$ is much lower than for the qG-FDT estimation (Fig. 5.1b). Therefore, the SEM$_\mathrm{det}$ with a ST/qG-FDT-adjusted closure experiences no improved performance compared to the FDT-SEM$_\mathrm{det}$ (not shown).

5.3 Discussion

In general, we observe an improved performance of the qG-FDT for the global anomalous forcing case (one of the first five EOFs as forcing; Fig. 5.4a) compared to the local anomalous forcing case (combination of the first 20 EOFs as forcing; Fig. 5.1a). According to Lutsko et al. (2015) taking more EOFs into account results in a higher uncertainty of the response operator. The qG-FDT response

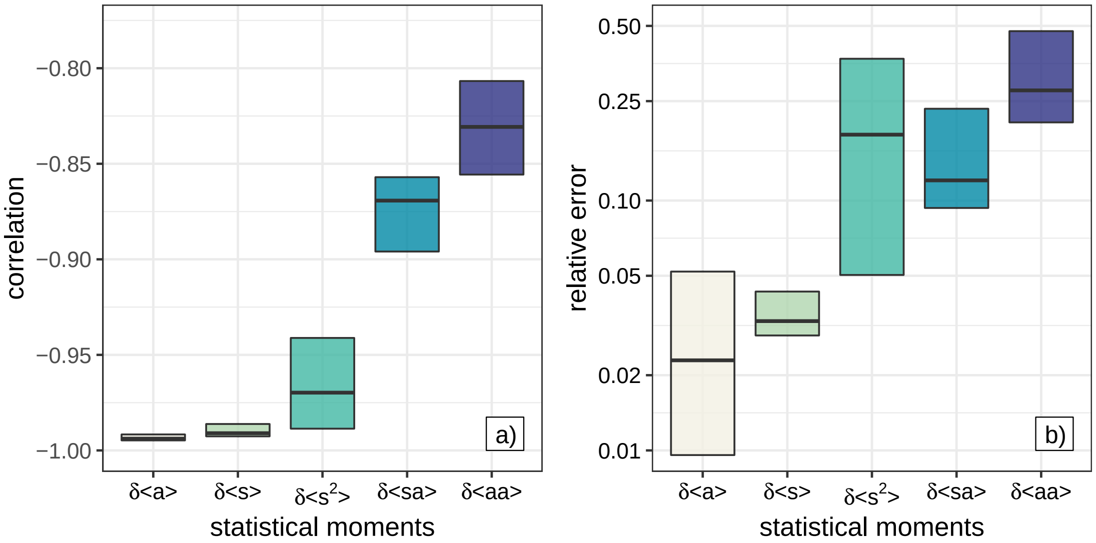

Figure 5.8: (a) Pattern correlation between the response of the local anomalous forcing with positive and negative amplitude, respectively. (b) as in Fig. 5.1a, but only taking the linear part of the true response into account.

operator is inversely proportional to the auto-covariance matrix (2.30) and thus inversely proportional to the eigenvalues of the EOFs. Since higher EOFs have per definition smaller eigenvalues this leads to sampling problems. However, the extremely long time series used in this study allows us to exclude sampling errors. In fact, tests showed that taking a subset of 3×10^6 days (or even fewer) resulted in nearly the same results as presented in this thesis. Furthermore, splitting the time series in six parts and hence creating an ensemble of qG-FDT response operators revealed a small ensemble spread while the ensemble mean operator yielded a quite similar result to the findings above. Therefore, it seems that the worse performance of the qG-FDT is not because of sampling errors but due to the "hot spot" nature of the forcing, which agrees with the result of Fuchs et al. (2015).

The higher errors in the second moments for both forcing cases and both FDT algorithms (Fig. 5.1a, Fig. 5.4a, and Fig. 5.7a) are to be expected. Gritsun et al. (2008) observed a similar behavior when applying the qG-FDT to an atmospheric GCM. Furthermore, for a transient response Majda et al. (2005, p. 68) proved that the error of the qG-FDT for the second moment ($\delta\langle \mathbf{aa}^{\mathrm{T}}\rangle$) is in general less accurate than that of the first moment ($\delta\langle \mathbf{a}\rangle$). On top of that, and in contrast to the literature (e.g., Gritsun and Branstator 2007; Gritsun et al. 2008), we use the full nonlinear a posteriori response of the QG3LM as a reference.

To investigate the impact of the nonlinearity in the a posteriori response we force the QG3LM with the local anomalous forcing but with opposite signs (i.e., $\pm\delta\mathbf{f}$). If the response is purely linear, the pattern correlation of those two forcing experiments should be -1. Figure 5.8a shows as an example the correlation of each relevant statistical moment for the 20 EOF case. Obviously, $\delta\langle\mathbf{a}\rangle$ and $\delta\langle\mathbf{s}\rangle$ are quite linear with $cor < -0.98$ and nearly no spread for all forcing cases, while the correlation of $\delta\langle s_i^2\rangle$ is slightly larger with values $cor < -0.94$ and exhibits a significant spread. The second moments have a pattern correlation of $-0.9 < cor < -0.8$. In other words, they experience a significant nonlinear response. Those nonlinearities lead to the reduced skill of the FDT in the prediction of the second moments. This is underlined by the comparison of the qG-FDT estimation to the purely linear part of the a posteriori response. The latter is extracted by subtracting the anomalous QG3LM with $-\delta\mathbf{f}$ from the simulation with $+\delta\mathbf{f}$ and dividing by 2. Since the nonlinearity is quadratic (3.1a) it cancels out and only the linear response remains (cf. Gritsun and Branstator 2016). In Fig. 5.8b we show the quality of the qG-FDT estimations of the linear part of the response. In comparison to the case with the full response (Fig. 5.1a) we observe nearly no change for the first moments. On the other hand, the estimations of the second moments are significantly improved, in terms of both median and spread. Yet, there is still a difference in relative error of roughly a factor of 10 between $\delta\langle\mathbf{a}\rangle$, $\delta\langle\mathbf{s}\rangle$ and $\delta\langle\mathbf{a}\mathbf{a}^{\mathrm{T}}\rangle$, $\delta\langle\mathbf{s}\mathbf{a}^{\mathrm{T}}\rangle$.

We observed a trend in the moments containing the SGS tendency error $\mathbf{s}$ (i.e., $\delta\langle\mathbf{s}\rangle, \delta\langle s_i^2\rangle$, and $\delta\langle\mathbf{s}\mathbf{a}^{\mathrm{T}}\rangle$): with increasing EOF truncation the quality of the FDT estimation deteriorates for both the qG-FDT (Fig. 5.1a; Fig. 5.4a) and the ST/qG-FDT (Fig. 5.7a). It could be that at higher EOF truncations we have larger contributions from the stable manifold (Gritsun and Lucarini 2017). However, by definition the amplitude of the SGS error decreases with increasing EOF truncation. Thus, all moments containing $\mathbf{s}$ suffer from a small signal-to-noise ratio. Repeating the experiments with only half of the time series increased the trend, which supports this hypothesis.

In Fig. 5.2e we see that the direct application of the qG-FDT operator yields

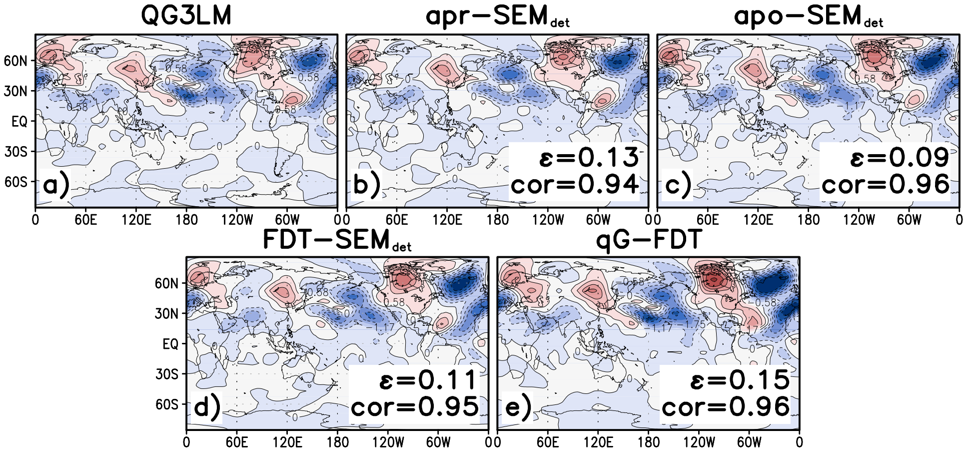

Figure 5.9: As in Fig. 5.2, but for response in meridional momentum flux ($\mathrm{m}^2\,\mathrm{s}^{-2}$; Pieroth et al. 2018, ©American Meteorological Society. Used with permission).

inferior results compared to the FDT-SEM (Fig. 5.2d). This is not universally the case. For the example of the response of meridional momentum flux $\delta\langle\mathbf{u}'\mathbf{v}'^{\mathrm{T}}\rangle$ (Fig. 5.9) we find that the direct qG-FDT application has roughly the same skill as the FDT-SEM. This variability in qG-FDT skill is again linked to the (non)linearity of the response of the considered observable. Obviously, the response of covariance of streamfunction contains to a significant degree nonlinearities while the response of meridional momentum flux seems to be quite linear. Unfortunately, the nonlinearity cannot be avoided. Thus, the original idea of Leith (1975) to utilize the FDT to estimate the climate response fails in some cases (e.g., Fig. 5.2e). Yet, using the linear estimations to update the empirical parameters of the SGS closure of a nonlinear model as proposed by Achatz et al. (2013) circumvents this issue. The results presented above and published in Achatz et al. (2013) and Pieroth et al. (2018) indicate that even for cases with nonlinear response the FDT-SEM has some skill.

In comparison to Achatz et al. (2013) the qG-FDT estimations of the response of the second moments worked significantly better, allowing a successful update of the linear operator in the SGS closure. Consequently, we show that in general the rFDT-SEM$_{\mathrm{det}}$ yields inferior results compared to the FDT-SEM$_{\mathrm{det}}$ (Fig. 5.3). This improvement was to be expected since the QG3LM with its relatively fast baroclinic instability better fulfills the constraints of the qG-FDT.

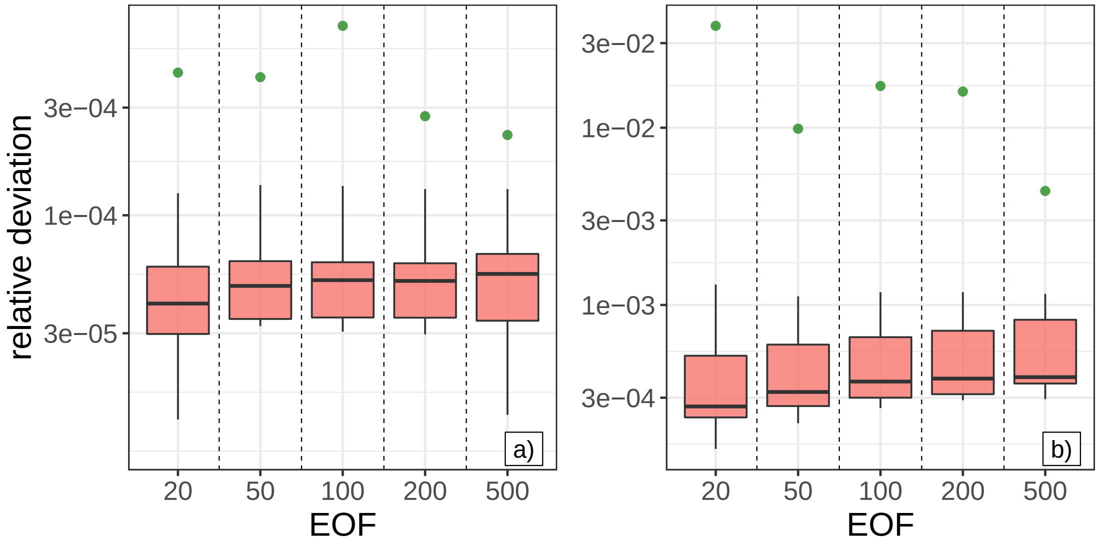

Figure 5.10: Strength of the QG3LM's response to the local anomalous forcing in comparison to the bias of the unforced $\mathrm{SEM}_{\mathrm{det}}$. The boxplot shows the relative deviation of (a) mean streamfunction and (b) covariance of streamfunction between the perturbed and unforced QG3LM against EOF truncation. The green dots are the relative errors of the unforced $\mathrm{SEM}_{\mathrm{det}}$ and QG3LM.

Nevertheless, the direct application of the qG-FDT significantly outperforms all of the SEMs for EOF truncations $\leq$ 200 EOFs for both the local (Fig. 5.3) and global anomalous forcing (Fig. 5.5), respectively. One could think that this is caused by a small signal-to-noise ratio. Indeed, comparing the bias in relative error of the unforced $\mathrm{SEM}_{\mathrm{det}}$ with the strength of the QG3LM's response reveals a disadvantageous ratio (Fig. 5.10). However, we find no correlation between the signal-to-noise ratio and the quality of the SEMs in Fig. 5.3. Because of the energy metric used for the construction of the EOFs we require at least 540 EOFs to explain 90% of the variance of the QG3LM (Fig. 3.1). Thus, SEMs based on fewer EOFs might be unable to produce a correct response, especially the response in covariance of streamfunction. Still, the results are meaningful since they show that the FDT approach in general works, even though the actual output of the FDT-SEM might not be particularly useful.

Part II

Subgrid-Scale Parameterizations based on First Principle

Chapter 6

Stochastic Mode Reduction

The theory of the stochastic mode reduction (SMR; or homogenization in the mathematical literature) for SDEs was developed by Papanicolaou (1976). Recently, SMR has found interest in geoscience (Majda et al. 2001; Majda et al. 2005). Since then its potential as an SGS parameterization has been studied in various toy models (Majda et al. 2002, 2003; Franzke et al. 2005; Dolaptchiev et al. 2013a; Dolaptchiev et al. 2013b; Wouters et al. 2016; Zacharuk et al. 2018), coupled toy ocean/atmosphere models (Demaeyer and Vannitsem 2018), and more complex atmospheric models (Franzke and Majda 2006). In principle, this method allows the construction of a parameterization based nearly fully on first principles (i.e., obtained directly from the model equations), by applying the following steps:

1.) Separation of the system's state vector into fast and slow variables with two[1] different characteristic scales.

2.) Introduction of a scale-separation factor ε that describes the characteristic scales mathematically.

3.) Replacement of the nonlinear self-interaction of the fast variable by a Gaussian stochastic process.

4.) For the limit of $\varepsilon \longrightarrow 0$ an effective equation for the slow variable is obtained that includes a stochastic parameterization, which accounts for the

---

[1] Extensions to multiple scales are possible (see references within Pavliotis and Stuart 2008), but we focus in this thesis on two scales only.

fast variable.

Conceptually, we require in step 4.) that the fast variable is infinitely faster than the slow variable. Thus, the explicit evolution of the former is no longer important: looking from the scale of the slow variable, the fast variable acts only as a random noise. The SMR provides a mathematically rigorous way to calculate this noise analytically from the model equations. Therefore, we expect the resulting SGS closure to be able to react to an external forcing. In the context of regime transitions this has already been shown by Franzke (2013) for an idealized four-dimensional toy model.

For the application of the SMR we require a scale separation. While this is given in the atmosphere and climate system, the limit of an infinite scale separation presents an approximation we have to make. However, recently the theory has been generalized to cases with a finite scale separation (Wouters and Gottwald 2018, 2019). The original articles (e.g., Majda et al. 2001, 2003) use an OU-process as a Gaussian process in step 3.). This assumption is relaxed by Franzke et al. (2005) in the so-called seamless SMR. However, both approaches rely in this step on empirical tuning, either by fitting the OU-process or by obtaining the required lag correlations directly from data, respectively. In this thesis we use the traditional approach and fit an OU-process explicitly, which allows us to apply the FDT later on.

6.1 Scale Separation

Consider an arbitrary system

$$\dot{\tilde{\mathbf{x}}} = \mathbf{F} + \mathsf{L}\tilde{\mathbf{x}} + \mathsf{N}\tilde{\mathbf{x}}\tilde{\mathbf{x}}\,, \tag{6.1}$$

where $\mathbf{F} \in \mathbb{R}^N$, $\mathsf{L} \in \mathbb{R}^{N\times N}$, and $\mathsf{N} \in \mathbb{R}^{N\times N\times N}$ are the explicit coefficients with $\mathbf{F}, \mathsf{L}, \mathsf{N} = \mathit{const.}$ and $\tilde{\mathbf{x}} \in \mathbb{R}^N$ denotes the state vector. We restrict our consideration deliberately to quadratic systems, since this is the highest nonlinearity in the QG3LM.

In the first step we assume that the state vector $\tilde{\mathbf{x}}$ can be separated in a slow variable $\mathbf{x} \in \mathbb{R}^S$ and a fast variable $\mathbf{y} \in \mathbb{R}^F$, because of the underlying physics. In practice this step is quite complex, since the scale separation is generally nontrivial (see section 7.1). However, at this point we simply assume that such a separation is possible and write (6.1) as

$$\dot{\mathbf{x}} = \mathbf{F}^{x} + \mathbf{L}^{xx}\mathbf{x} + \mathbf{N}^{xxx}\mathbf{x}\mathbf{x} + \mathbf{L}^{xy}\mathbf{y} + \mathbf{N}^{xxy}\mathbf{x}\mathbf{y} + \mathbf{N}^{xyx}\mathbf{y}\mathbf{x} + \mathbf{N}^{xyy}\mathbf{y}\mathbf{y} \tag{6.2a}$$

$$\dot{\mathbf{y}} = \mathbf{F}^{y} + \mathbf{L}^{yx}\mathbf{x} + \mathbf{N}^{yxx}\mathbf{x}\mathbf{x} + \mathbf{L}^{yy}\mathbf{y} + \mathbf{N}^{yxy}\mathbf{x}\mathbf{y} + \mathbf{N}^{yyx}\mathbf{y}\mathbf{x} + \mathbf{N}^{yyy}\mathbf{y}\mathbf{y}\,, \tag{6.2b}$$

where the superscript $\bullet^{\mu\nu\rho}$ denotes that the latter variables (ν and ρ) act on the first one (μ). In addition, the superscript indicates the dimension of the tensors (e.g., $\mathbf{N}^{xyx} \in \mathbb{R}^{S\times F\times S}$).

Applying a suitable nondimensionalization results in

$$\begin{aligned}
\mathrm{d}\hat{\mathbf{x}} &= \left(\hat{\mathbf{F}}^{x} + \hat{\mathbf{L}}^{xx}\hat{\mathbf{x}} + \hat{\mathbf{N}}^{xxx}\hat{\mathbf{x}}\hat{\mathbf{x}}\right)\mathrm{d}\hat{t} \\
&\quad + \frac{1}{\varepsilon}\left(\hat{\mathbf{L}}^{xy}\hat{\mathbf{y}} + \hat{\mathbf{N}}^{xxy}\hat{\mathbf{x}}\hat{\mathbf{y}} + \hat{\mathbf{N}}^{xyx}\hat{\mathbf{y}}\hat{\mathbf{x}} + \hat{\mathbf{N}}^{xyy}\hat{\mathbf{y}}\hat{\mathbf{y}}\right)\mathrm{d}\hat{t} \qquad (6.3\text{a}) \\
\mathrm{d}\hat{\mathbf{y}} &= \frac{1}{\varepsilon}\left(\hat{\mathbf{F}}^{y} + \hat{\mathbf{L}}^{yx}\hat{\mathbf{x}} + \hat{\mathbf{N}}^{yxx}\hat{\mathbf{x}}\hat{\mathbf{x}} + \hat{\mathbf{L}}^{yy}\hat{\mathbf{y}} + \hat{\mathbf{N}}^{yxy}\hat{\mathbf{x}}\hat{\mathbf{y}} + \hat{\mathbf{N}}^{yyx}\hat{\mathbf{y}}\hat{\mathbf{x}}\right)\mathrm{d}\hat{t} \\
&\quad + \frac{1}{\varepsilon^{2}}\hat{\mathbf{N}}^{yyy}\hat{\mathbf{y}}\hat{\mathbf{y}}\mathrm{d}\hat{t}\,, \qquad (6.3\text{b})
\end{aligned}$$

since we split the model accordingly. An estimation of ε in our case is given in section 7.2.1. For convenience we suppress the hats from now on.

6.2 Introduction of an Empirical Ornstein-Uhlenbeck Process

The only empirical step of the SMR is the replacement of the nonlinear self-interaction term of the fast variable in (6.3b) by an OU-process:

$$\mathbf{N}^{yyy}\mathbf{y}\mathbf{y}\mathrm{d}t \longrightarrow \mathbf{l}^{yy}_{\mathrm{OU}}\mathbf{y}\mathrm{d}t + \boldsymbol{\sigma}^{y}\mathrm{d}\mathbf{W}^{y}\,, \tag{6.4}$$

where $\mathbf{l}^{yy}_{\mathrm{OU}}, \boldsymbol{\sigma}^{y} \in \mathbb{R}^{F\times F}$ are constant, $\boldsymbol{\sigma}^{y}$ is diagonal, and $\mathrm{d}\mathbf{W}^{y} \in \mathbb{R}^{F}$ denotes a Wiener increment. The respective parameters of the OU-process are obtained empirically by the Maximum-Likelihood method (see appendix B.2). The classical

SMR of Majda et al. (2002) assumes also a diagonal drift term $\mathbf{l}^{yy}_{\mathrm{OU}}$. However, this assumption has been relaxed by Dolaptchiev et al. (2013a) and is also dropped here: the drift term of the OU-process is considered to be a nondiagonal and dense matrix.

While introducing the OU-process, the drift term inherits the scaling of the nonlinear self-interaction term. The diffusion term has to be rescaled to ε^{-1} to assure the same scaling as the drift term in the FPE (6.15), because of the properties of a Wiener increment (Gardiner 2009). Thus,

$$\begin{aligned} \mathrm{d}\mathbf{x} &= \left(\mathbf{F}^{x} + \mathsf{L}^{xx}\mathbf{x} + \mathsf{N}^{xxx}\mathbf{x}\mathbf{x}\right)\mathrm{d}t \\ &\quad + \frac{1}{\varepsilon}\left(\mathsf{L}^{xy}\mathbf{y} + \mathsf{N}^{xxy}\mathbf{x}\mathbf{y} + \mathsf{N}^{xyx}\mathbf{y}\mathbf{x} + \mathsf{N}^{xyy}\mathbf{y}\mathbf{y}\right)\mathrm{d}t \qquad (6.5\text{a}) \\ \mathrm{d}\mathbf{y} &= \frac{1}{\varepsilon}\left(\mathbf{F}^{y} + \mathsf{L}^{yx}\mathbf{x} + \mathsf{L}^{yy}\mathbf{y} + \mathsf{N}^{yxx}\mathbf{x}\mathbf{x} + \mathsf{N}^{yxy}\mathbf{x}\mathbf{y} + \mathsf{N}^{yyx}\mathbf{y}\mathbf{x}\right)\mathrm{d}t \\ &\quad + \frac{1}{\varepsilon^{2}}\mathbf{l}^{yy}_{\mathrm{OU}}\mathbf{y}\mathrm{d}t + \frac{1}{\varepsilon}\boldsymbol{\sigma}^{y}\mathrm{d}\mathbf{W}^{y}\,. \qquad (6.5\text{b}) \end{aligned}$$

In the next step we diagonalize $\mathbf{l}^{yy}_{\mathrm{OU}}$. In general this results in a complex diagonal matrix with eigenvalues that form a complex conjugate pair. Thus, we transform this complex matrix into a real block-diagonal matrix with 2-by-2 blocks (appendix C.1). Consequently, the columns of the transformation matrix $\mathsf{U} \in \mathbb{R}^{F\times F}$ do not consist of the complex eigenvectors of $\mathbf{l}^{yy}_{\mathrm{OU}}$ but of a combination of their real and imaginary part[2]. We write

$$\mathbf{l}^{yy}_{\mathrm{OU}} = \mathsf{U}\boldsymbol{\Lambda}\mathsf{U}^{-1}\,, \qquad (6.6)$$

where $\boldsymbol{\Lambda} \in \mathbb{R}^{F\times F}$ is the real block-diagonal matrix of $\mathbf{l}^{yy}_{\mathrm{OU}}$. Furthermore, let

$$\tilde{\mathbf{y}} = \mathsf{U}^{-1}\mathbf{y} \qquad \mathrm{d}\tilde{\mathbf{y}} = \mathsf{U}^{-1}\mathrm{d}\mathbf{y}\,. \qquad (6.7)$$

---

[2] In practice, the MATLAB routine *cdf2rdf* is used for this step.

With (6.6) and (6.7) we are able to write (6.5) as

$$\begin{aligned}
\mathrm{d}\mathbf{x} &= (\mathbf{F}^{x} + \mathsf{L}^{xx}\mathbf{x} + \mathsf{N}^{xxx}\mathbf{x}\mathbf{x})\mathrm{d}t \\
&\quad + \frac{1}{\varepsilon}\left(\tilde{\mathsf{L}}^{xy}\tilde{\mathbf{y}} + \tilde{\mathsf{N}}^{xxy}\mathbf{x}\tilde{\mathbf{y}} + \tilde{\mathsf{N}}^{xyx}\tilde{\mathbf{y}}\mathbf{x} + \tilde{\mathsf{N}}^{xyy}\tilde{\mathbf{y}}\tilde{\mathbf{y}}\right)\mathrm{d}t && \text{(6.8a)} \\
\mathrm{d}\tilde{\mathbf{y}} &= \frac{1}{\varepsilon}\left(\tilde{\mathbf{F}}^{y} + \tilde{\mathsf{L}}^{yx}\mathbf{x} + \tilde{\mathsf{N}}^{yxx}\mathbf{x}\mathbf{x} + \tilde{\mathsf{L}}^{yy}\tilde{\mathbf{y}} + \tilde{\mathsf{N}}^{yxy}\mathbf{x}\tilde{\mathbf{y}} + \tilde{\mathsf{N}}^{yyx}\tilde{\mathbf{y}}\mathbf{x}\right)\mathrm{d}t \\
&\quad + \frac{1}{\varepsilon^{2}}\mathbf{\Lambda}\tilde{\mathbf{y}}\mathrm{d}t + \frac{1}{\varepsilon}\tilde{\boldsymbol{\sigma}}^{y}\mathrm{d}\mathbf{W}^{y}\,, && \text{(6.8b)}
\end{aligned}$$

where the tilded quantities are the respective transformed coefficients[3].

Because of the transformation, $\tilde{\boldsymbol{\sigma}}^{y}$ is no longer a diagonal matrix. In recent articles (Zacharuk et al. 2018; Dolaptchiev et al. 2013a) the noise amplitude matrix has been replaced by an effective diagonal matrix $\boldsymbol{\sigma}^{\star y}_{ii} = [\sum_{j=1}^{F}(\tilde{\boldsymbol{\sigma}}^{y}_{ij})^{2}]^{1/2}$ to be conform to the classical SMR of Majda et al. (2002). This simplifies the calculation of the closure. For this thesis, however, tests with an RSM including this approximation revealed a significant decrease of performance for certain truncations of (S, F). Therefore, we do not replace the noise amplitude by an effective diagonal matrix. Instead, we keep the nondiagonal $\tilde{\boldsymbol{\sigma}}^{y}$ and thus generalize the approach of Dolaptchiev et al. (2013a).

6.3 Series Expansion of the Fokker-Planck Equation

For better readability we neglect the tilde from now on. Furthermore, we define

$$f_0(\mathbf{x}) = \mathbf{F}^{x} + \mathsf{L}^{xx}\mathbf{x} + \mathsf{N}^{xxx}\mathbf{x}\mathbf{x} \tag{6.9}$$

$$f_1(\mathbf{x},\mathbf{y}) = \mathsf{L}^{xy}\mathbf{y} + \mathsf{N}^{xxy}\mathbf{x}\mathbf{y} + \mathsf{N}^{xyx}\mathbf{y}\mathbf{x} + \mathsf{N}^{xyy}\mathbf{y}\mathbf{y} \tag{6.10}$$

$$g_0 = 0 \tag{6.11}$$

$$g_1(\mathbf{x},\mathbf{y}) = \mathbf{F}^{y} + \mathsf{L}^{yx}\mathbf{x} + \mathsf{N}^{yxx}\mathbf{x}\mathbf{x} + \mathsf{L}^{yy}\mathbf{y} + \mathsf{N}^{yxy}\mathbf{x}\mathbf{y} + \mathsf{N}^{yyx}\mathbf{y}\mathbf{x} \tag{6.12}$$

$$g_2(\mathbf{y}) = \mathbf{\Lambda}\mathbf{y}\,, \tag{6.13}$$

---

[3] For an improved readability we suppress the tilde in the superscripts.

which allows us to summarize (6.8) as

$$\mathrm{d}\mathbf{x} = f_0(\mathbf{x})\mathrm{d}t + \frac{1}{\varepsilon} f_1(\mathbf{x},\mathbf{y})\mathrm{d}t \tag{6.14a}$$

$$\mathrm{d}\mathbf{y} = g_0\mathrm{d}t + \frac{1}{\varepsilon} g_1(\mathbf{x},\mathbf{y})\mathrm{d}t + \frac{1}{\varepsilon^2} g_2(\mathbf{y})\mathrm{d}t + \frac{1}{\varepsilon}\boldsymbol{\sigma}^y \mathrm{d}\mathbf{W}^y\,. \tag{6.14b}$$

Obviously, $g_0 = 0$ will not contribute to the following calculation. However, in the anomaly experiments (see section 8.3.1) this term can potentially be nonzero. Thus, we formally keep it here.

The corresponding FPE for the PDF $p \equiv p(\mathbf{x},\mathbf{y},t|\mathbf{x}_0,\mathbf{y}_0,t_0)$ is given by

$$\partial_t p = L_3 p + \frac{1}{\varepsilon} L_2 p + \frac{1}{\varepsilon^2} L_1 p\,, \tag{6.15}$$

where

$$L_1 = -g_2(\mathbf{y})\cdot\nabla_y - \frac{1}{2}\boldsymbol{\Sigma} : \nabla_y\nabla_y \tag{6.16}$$

$$L_2 = -f_1(\mathbf{x},\mathbf{y})\cdot\nabla_x - g_1(\mathbf{x},\mathbf{y})\cdot\nabla_y \tag{6.17}$$

$$L_3 = -f_0(\mathbf{x})\cdot\nabla_x - g_0\cdot\nabla_y\,, \tag{6.18}$$

and $\boldsymbol{\Sigma} = \boldsymbol{\sigma}^y(\boldsymbol{\sigma}^y)^{\mathrm{T}}$ is a nondiagonal matrix.

Next, we expand the solution of (6.15) in terms of the scale-separation factor:

$$p = p^{(0)} + \varepsilon p^{(1)} + \varepsilon^2 p^{(2)} + \mathcal{O}(\varepsilon^3)\,. \tag{6.19}$$

Substituting this series into the FPE (6.15) yields

$$\partial_t p^{(0)} = L_3 p^{(0)} + \frac{1}{\varepsilon} L_2 p^{(0)} + L_2 p^{(1)} + \frac{1}{\varepsilon^2} L_1 p^{(0)} + \frac{1}{\varepsilon} L_1 p^{(1)} + L_1 p^{(2)} + \mathcal{O}(\varepsilon)\,. \tag{6.20}$$

Thus follows for the leading orders:

$$\mathcal{O}(\varepsilon^{-2}) \qquad 0 = L_1 p^{(0)} \tag{6.21}$$

$$\mathcal{O}(\varepsilon^{-1}) \qquad 0 = L_2 p^{(0)} + L_1 p^{(1)} \tag{6.22}$$

$$\mathcal{O}(1) \qquad \partial_t p^{(0)} = L_3 p^{(0)} + L_2 p^{(1)} + L_1 p^{(2)}\,. \tag{6.23}$$

First we remark that from (6.21) follows

$$p^{(0)} = p^{(0)}(\mathbf{x}, t|\mathbf{x}_0, t_0), \tag{6.24}$$

as is proven in appendix C.1.

We are interested in an effective equation of the slow variable where the fast variable is eliminated. For this we need to express (6.23) in terms of $p^{(0)}$ only. In order to do so we have to rearrange (6.22) for $p^{(1)}$. Formally this yields

$$p^{(1)} = -L_1^{-1} L_2 p^{(0)}\,, \tag{6.25}$$

where L_1^{-1} is the generalized inverse of L_1 (see appendix C.1). For its existence we require that $L_2 p^{(0)} \notin \ker L_1$, since otherwise we would not be able to solve (6.22) for a unique $p^{(1)}$.

Let $\mathcal{P}$ be the projection operator onto the nullspace of L_1. Then we may write $L_2 p^{(0)} \notin \ker L_1$ as

$$\mathcal{P} L_2 p^{(0)} = 0\,, \tag{6.26}$$

where the exact form of $\mathcal{P}$ is given in appendix C.1. Equation (6.26) is the so-called solvability condition, which has to be (at least approximately) fulfilled by the system[4]. Inserting L_2, applying the projection operator, and utilizing (6.24) yields

$$\begin{aligned} 0 &= -\mathcal{P}[f_1(\mathbf{x}, \mathbf{y}) \cdot \nabla_x - g_1(\mathbf{x}, \mathbf{y}) \cdot \nabla_y] p^{(0)} \\ &= -\mathbb{E}\left[f_1(\mathbf{x}, \mathbf{y})\right]_{\mathrm{OU}} \cdot \nabla_x p^{(0)}\,, \end{aligned} \tag{6.27}$$

where $\mathbb{E}[\cdot]_{\mathrm{OU}}$ is the expectation value with respect to the stationary distribution of the OU-process (C.13). Since the OU-process has zero mean, all odd moments

---

[4] Otherwise, correction terms of order ε^{-1} are present in the effective equation of $p^{(0)}$ (Papanicolaou 1976; Demaeyer and Vannitsem 2018).

of the expectation value vanishes. Thus, the solvability condition reads

$$0 = \mathsf{N}^{xyy}_{ijk}\mathsf{D}_{jk}\frac{\partial p^{(0)}}{\partial x_i}\,, \tag{6.28}$$

where D is the variance of the OU-process, which can be obtained from the so-called Lyapunov equation (see appendix C.1 for the calculation; Gardiner 2009). (6.28) can only be fulfilled if either $\mathsf{N}^{xyy}_{ijk}\mathsf{D}_{jk} = 0$, $\forall i$ or if this vector is perpendicular to $\nabla p^{(0)}$.

If the solvability condition is fulfilled, we can apply the projection operator to (6.23). This results in

$$\begin{aligned}\partial_t \mathcal{P} p^{(0)} &= \mathcal{P} L_3 p^{(0)} + \mathcal{P} L_2 p^{(1)} + \mathcal{P} L_1 p^{(2)} & (6.29)\\ &= L_3 p^{(0)} + \mathcal{P} L_2 p^{(1)}\,, & (6.30)\end{aligned}$$

since $\mathcal{P}$ acts only on the fast variable (C.10) and both $p^{(0)}$ (6.24) and L_3 (6.18) dependent only on the slow variable. Furthermore, the last term in (6.29) vanishes, since it is projected onto the nullspace of L_1. Thus, with (6.25) follows

$$\partial_t p^{(0)} = L_3 p^{(0)} - \mathcal{P} L_2 L_1^{-1} L_2 p^{(0)}\,. \tag{6.31}$$

Applying the operators (for a detailed calculation see appendix C.2) results in

$$\begin{aligned}\partial_t p^{(0)} = -\Bigg[f_0(\mathbf{x}) + \int_0^\infty \Big\{ & \mathbb{E}\left[\{f_1(\mathbf{x},\mathbf{y})\cdot\nabla_x\} f_1(\mathbf{x},\mathbf{y}[\tau])\right]_{\mathrm{OU}} \\ & + \mathbb{E}\left[\{g_1(\mathbf{x},\mathbf{y})\cdot\mathsf{D}^{-1}\mathbf{y}\} f_1(\mathbf{x},\mathbf{y}[\tau])\right]_{\mathrm{OU}} \\ & - \mathbb{E}\left[\{\nabla_y\cdot g_1(\mathbf{x},\mathbf{y})\} f_1(\mathbf{x},\mathbf{y}[\tau])\right]_{\mathrm{OU}} \Big\}\mathrm{d}\tau \Bigg]\cdot\nabla_x p^{(0)} \\ & - \int_0^\infty \mathbb{E}\left[f_1(\mathbf{x},\mathbf{y})\otimes f_1(\mathbf{x},\mathbf{y}[\tau])\right]_{\mathrm{OU}}\mathrm{d}\tau : \nabla_x\nabla_x p^{(0)}\,. \end{aligned} \tag{6.32}$$

6.4 Effective Equation of the Slow Variable

In order to obtain an Itô-SDE from (6.32), the amplitude matrix of the diffusion term has to be Cholesky-decomposed. The decomposition exists for this particular set of systems, as is proven in appendix C.3. Consequently, the effective equation with the SMR parameterization (i.e., the RSM) reads

$$\begin{aligned}\mathrm{d}\mathbf{x} &= (\mathbf{F}^{x} + \boldsymbol{\mathsf{L}}^{xx}\mathbf{x} + \boldsymbol{\mathsf{N}}^{xxx}\mathbf{x}\mathbf{x})\mathrm{d}t \\ &\quad + (\boldsymbol{\mathcal{F}} + \boldsymbol{\mathcal{L}}\mathbf{x} + \boldsymbol{\mathcal{Q}}\mathbf{x}\mathbf{x} + \boldsymbol{\mathcal{C}}\mathbf{x}\mathbf{x}\mathbf{x})\mathrm{d}t + \boldsymbol{\mathcal{A}}\mathrm{d}\mathbf{W}^{(1)} + \boldsymbol{\mathcal{M}}(\mathbf{x})\mathrm{d}\mathbf{W}^{(2)}\,, \qquad (6.33)\end{aligned}$$

where $\boldsymbol{\mathcal{F}}, \mathrm{d}\mathbf{W}^{(1)} \in \mathbb{R}^{S}$, $\boldsymbol{\mathcal{L}}, \boldsymbol{\mathcal{A}} \in \mathbb{R}^{S\times S}$, $\mathrm{d}\mathbf{W}^{(2)} \in \mathbb{R}^{F}$, $\boldsymbol{\mathcal{M}} \in \mathbb{R}^{S\times F}$, $\boldsymbol{\mathcal{Q}} \in \mathbb{R}^{S\times S\times S}$, and $\boldsymbol{\mathcal{C}} \in \mathbb{R}^{S\times S\times S\times S}$. Furthermore, $\mathrm{d}\mathbf{W}^{(1)}$ and $\mathrm{d}\mathbf{W}^{(2)}$ are independent. Following the notation of Dolaptchiev et al. (2013a) the closure parameters are given by

$$\begin{aligned}
\boldsymbol{\mathcal{F}}_{i} &= \mathbf{F}^{y}_{j}\boldsymbol{\mathsf{L}}^{xy}_{ik}\boldsymbol{\mathsf{K}}_{kj} + \left[\boldsymbol{\mathsf{L}}^{xy}_{lm}(\boldsymbol{\mathsf{N}}^{xxy}_{ilj} + \boldsymbol{\mathsf{N}}^{xyx}_{ijl})\boldsymbol{\mathsf{K}}_{jn} + \boldsymbol{\mathsf{L}}^{yy}_{lm}\boldsymbol{\mathsf{N}}^{xyy}_{ijk}\left(\boldsymbol{\mathsf{P}}_{jknl} + \boldsymbol{\mathsf{P}}_{jkln}\right)\right]\boldsymbol{\mathsf{D}}_{nm} && (6.34a)\\
\boldsymbol{\mathcal{L}}_{ij} &= \left[\mathbf{F}^{y}_{l}(\boldsymbol{\mathsf{N}}^{xxy}_{ijk} + \boldsymbol{\mathsf{N}}^{xyx}_{ikj}) + (\boldsymbol{\mathsf{N}}^{xxy}_{pjm} + \boldsymbol{\mathsf{N}}^{xyx}_{pmj})(\boldsymbol{\mathsf{N}}^{xxy}_{ipk} + \boldsymbol{\mathsf{N}}^{xyx}_{ikp})\boldsymbol{\mathsf{D}}_{lm} + \boldsymbol{\mathsf{L}}^{yx}_{lj}\boldsymbol{\mathsf{L}}^{xy}_{ik}\right]\boldsymbol{\mathsf{K}}_{kl} \\
&\quad + (\boldsymbol{\mathsf{N}}^{yxy}_{ljm} + \boldsymbol{\mathsf{N}}^{yyx}_{lmj})\boldsymbol{\mathsf{N}}^{xyy}_{ipk}\left(\boldsymbol{\mathsf{P}}_{pknl} + \boldsymbol{\mathsf{P}}_{pkln}\right)\boldsymbol{\mathsf{D}}_{nm} && (6.34b)\\
\boldsymbol{\mathcal{Q}}_{ijk} &= \left[\boldsymbol{\mathsf{L}}^{yx}_{lk}(\boldsymbol{\mathsf{N}}^{xxy}_{ijm} + \boldsymbol{\mathsf{N}}^{xyx}_{imj}) + \boldsymbol{\mathsf{N}}^{yxx}_{lkj}\boldsymbol{\mathsf{L}}^{xy}_{im}\right]\boldsymbol{\mathsf{K}}_{ml} && (6.34c)\\
\boldsymbol{\mathcal{C}}_{ijkl} &= \boldsymbol{\mathsf{N}}^{yxx}_{mkj}(\boldsymbol{\mathsf{N}}^{xxy}_{iln} + \boldsymbol{\mathsf{N}}^{xyx}_{inl})\boldsymbol{\mathsf{K}}_{nm} && (6.34d)\\
\boldsymbol{\mathcal{A}}_{ij} &= \sqrt{2}(\boldsymbol{\mathsf{C}}_{T})_{ij} && (6.34e)\\
\boldsymbol{\mathcal{M}}_{ij} &= \sqrt{2}(\boldsymbol{\mathsf{C}}_{S})_{lj}\left[\boldsymbol{\mathsf{L}}^{xy}_{il} + (\boldsymbol{\mathsf{N}}^{xxy}_{iml} + \boldsymbol{\mathsf{N}}^{xyx}_{ilm})\mathbf{x}_{m}\right]\,, && (6.34f)
\end{aligned}$$

where $\boldsymbol{\mathsf{C}}_{S} \in \mathbb{R}^{F\times F}$ and $\boldsymbol{\mathsf{C}}_{T} \in \mathbb{R}^{S\times S}$ are the Cholesky-decompositions of

$$\begin{aligned}
\boldsymbol{\mathsf{S}}_{lk} &= \frac{1}{2}\left(\boldsymbol{\mathsf{K}}_{lj}\boldsymbol{\mathsf{D}}_{jk} + \boldsymbol{\mathsf{K}}_{kj}\boldsymbol{\mathsf{D}}_{jl}\right) && (6.35)\\
\boldsymbol{\mathsf{T}}_{op} &= \frac{1}{2}\boldsymbol{\mathsf{N}}^{xyy}_{omn}\left[\boldsymbol{\mathsf{P}}_{mnij}\left(\boldsymbol{\mathsf{D}}_{ik}\boldsymbol{\mathsf{D}}_{jl} + \boldsymbol{\mathsf{D}}_{il}\boldsymbol{\mathsf{D}}_{jk}\right) + \boldsymbol{\mathsf{P}}_{klij}\left(\boldsymbol{\mathsf{D}}_{im}\boldsymbol{\mathsf{D}}_{jn} + \boldsymbol{\mathsf{D}}_{in}\boldsymbol{\mathsf{D}}_{jm}\right)\right]\boldsymbol{\mathsf{N}}^{xyy}_{pkl} && (6.36)
\end{aligned}$$

and $\boldsymbol{\mathsf{D}}$ is given in appendix C.1. Furthermore, the tensors $\boldsymbol{\mathsf{K}} \in \mathbb{R}^{F\times F}$ and $\boldsymbol{\mathsf{P}} \in \mathbb{R}^{F\times F\times F\times F}$ are defined by

$$\int_{0}^{\infty} \mathbf{y}_{i}(\tau)\mathrm{d}\tau = \boldsymbol{\mathsf{K}}_{ij}\mathbf{y}_{j}(0) \qquad (6.37)$$

$$\int_0^\infty \mathbf{y}_i(\tau)\mathbf{y}_j(\tau)\mathrm{d}\tau = \mathsf{P}_{ijkl}\mathbf{y}_k(0)\mathbf{y}_l(0)\,, \tag{6.38}$$

and read in particular (Dolaptchiev et al. 2013a)

$$\mathsf{K}_{ij} = \begin{cases} \frac{\gamma_i}{\gamma_i^2+\omega_i^2}, & j = i \\ \frac{\omega_i}{\gamma_i^2+\omega_i^2}, & j = i + \mathrm{sgn}(\omega_i), \omega_i \neq 0 \\ 0, & \text{else} \end{cases} \tag{6.39}$$

$$\mathsf{P}_{ijkl} = \begin{cases} \kappa_{ij}(\gamma_i+\gamma_j)\left[(\gamma_i+\gamma_j)^2+\omega_i^2+\omega_j^2\right], & k = i, l = j \\ \kappa_{ij}\omega_i\left[(\gamma_i+\gamma_j)^2+\omega_i^2-\omega_j^2\right], & k = i+\mathrm{sgn}(\omega_i), l = j, \omega_i \neq 0 \\ \kappa_{ij}\omega_j\left[(\gamma_i+\gamma_j)^2+\omega_j^2-\omega_i^2\right], & k = i, l = j+\mathrm{sgn}(\omega_j), \omega_j \neq 0 \\ 2\kappa_{ij}\omega_i\omega_j(\gamma_i+\gamma_j), & \begin{array}{l} k = i+\mathrm{sgn}(\omega_i), l = j+\mathrm{sgn}(\omega_j), \\ \omega_{i,j} \neq 0 \end{array} \\ 0, & \text{else} \end{cases} \tag{6.40}$$

$$\kappa_{ij} = \left\{\left[(\gamma_i+\gamma_j)^2+(\omega_i-\omega_j)^2\right]\left[(\gamma_i+\gamma_j)^2+(\omega_i+\omega_j)^2\right]\right\}^{-1}\,, \tag{6.41}$$

where sgn(·) denotes the sign function

$$\mathrm{sgn}(x) = \begin{cases} 1, & x \geq 0 \\ -1, & \text{else} \end{cases} \tag{6.42}$$

and the definitions of $\boldsymbol{\gamma}, \boldsymbol{\omega} \in \mathbb{R}^F$ are given in appendix C.1. In principle, it is possible to construct $\tilde{\boldsymbol{\mathcal{M}}} \in \mathbb{R}^{S\times S}$ (Franzke et al. 2005; Franzke and Majda 2006), however, this would require a Cholesky-decomposition each integration time step.

Chapter 7

Stochastic Mode Reduction Applied to the Quasigeostrophic Three-Layer Model

We want to apply the SMR to the QG3LM, which served already as a testbed of the FDT approach in part I. However, we do not apply the SMR directly to the full QG3LM but rather to a suitable subspace of the EOF spectrum. In this chapter we define this subspace and explain in detail the involved approximations. Furthermore, we derive the model equations on which the SMR is eventually applied to and introduce the so-called bare truncation model.

7.1 Scale Separation

Consider the QG3LM in the full EOF space (i.e., $\mathbf{a} \in \mathbb{R}^N$ with $N = 1449$)

$$\dot{\mathbf{a}} = \mathbf{F} + \mathsf{L}\mathbf{a} + \mathsf{N}\mathbf{a}\mathbf{a}\,, \tag{7.1}$$

where $\mathbf{F} \in \mathbb{R}^N$, $\mathsf{L} \in \mathbb{R}^{N\times N}$, and $\mathsf{N} \in \mathbb{R}^{N\times N\times N}$ are the constant explicit EOF coefficients (appendix E). Next, we split the state vector into a slow variable $\mathbf{x} \in \mathbb{R}^S$ and a fast variable $\mathbf{y} \in \mathbb{R}^F$ as already introduced in the derivation of the SMR closure. In addition, we introduce a third variable $\mathbf{z} \in \mathbb{R}^H$ (such that $N = S + F + H$), which we call hidden variable. With this decomposition we can rewrite (7.1) as three coupled differential equations given by

$$
\begin{aligned}
\dot{\mathbf{x}} &= \mathbf{F}^x + \mathbf{L}^{xx}\mathbf{x} + \mathbf{N}^{xxx}\mathbf{x}\mathbf{x} + \mathbf{L}^{xy}\mathbf{y} + \mathbf{N}^{xxy}\mathbf{x}\mathbf{y} + \mathbf{N}^{xyx}\mathbf{y}\mathbf{x} + \mathbf{N}^{xyy}\mathbf{y}\mathbf{y} \\
&\quad + \mathbf{L}^{xz}\mathbf{z} + \mathbf{N}^{xxz}\mathbf{x}\mathbf{z} + \mathbf{N}^{xzx}\mathbf{z}\mathbf{x} + \mathbf{N}^{xyz}\mathbf{y}\mathbf{z} + \mathbf{N}^{xzy}\mathbf{z}\mathbf{y} + \mathbf{N}^{xzz}\mathbf{z}\mathbf{z} \qquad (7.2a) \\
\dot{\mathbf{y}} &= \mathbf{F}^y + \mathbf{L}^{yx}\mathbf{x} + \mathbf{N}^{yxx}\mathbf{x}\mathbf{x} + \mathbf{L}^{yy}\mathbf{y} + \mathbf{N}^{yxy}\mathbf{x}\mathbf{y} + \mathbf{N}^{yyx}\mathbf{y}\mathbf{x} + \mathbf{N}^{yyy}\mathbf{y}\mathbf{y} \\
&\quad + \mathbf{L}^{yz}\mathbf{z} + \mathbf{N}^{yxz}\mathbf{x}\mathbf{z} + +\mathbf{N}^{yzx}\mathbf{z}\mathbf{x} + \mathbf{N}^{yyz}\mathbf{y}\mathbf{z} + \mathbf{N}^{yzy}\mathbf{z}\mathbf{y} + \mathbf{N}^{yzz}\mathbf{z}\mathbf{z} \qquad (7.2b) \\
\dot{\mathbf{z}} &= \mathbf{F}^z + \mathbf{L}^{zx}\mathbf{x} + \mathbf{N}^{zxx}\mathbf{x}\mathbf{x} + \mathbf{L}^{zy}\mathbf{y} + \mathbf{N}^{zxy}\mathbf{x}\mathbf{y} + \mathbf{N}^{zyx}\mathbf{y}\mathbf{x} + \mathbf{N}^{zyy}\mathbf{y}\mathbf{y} \\
&\quad + \mathbf{L}^{zz}\mathbf{z} + \mathbf{N}^{zxz}\mathbf{x}\mathbf{z} + \mathbf{N}^{zzx}\mathbf{z}\mathbf{x} + \mathbf{N}^{zyz}\mathbf{y}\mathbf{z} + \mathbf{N}^{zzy}\mathbf{z}\mathbf{y} + \mathbf{N}^{zzz}\mathbf{z}\mathbf{z}\,, \qquad (7.2c)
\end{aligned}
$$

where the exact shape of the tensors depends on the choice of the splitting.

In order to quantify a meaningful partition of the EOF space (i.e., one that - at least approximately - results in a scale separation) we use the integral over the absolute value of the autocorrelation function (no Einstein's summation convention)

$$
T_k = \int_0^\infty \left| \frac{\langle \mathbf{a}_k(t)\mathbf{a}_k(t+s) \rangle}{\langle \mathbf{a}_k^2 \rangle} \right| \mathrm{d}s \qquad (7.3)
$$

as an indicator of how fast the kth EOF loses its memory (Franzke and Majda 2006). The spectrum of (7.3) for all EOFs is given in Fig. 7.1. Obviously, it is a continuous curve with no clear time-scale separation. The slowest (i.e., leading) view EOFs have a decorrelation time scale of about 15-40 days. However, we observe a peak at the 1318th EOF of about 19 days. Similar results were obtained by Franzke and Majda (2006) for the same model in northern hemispheric mode, which identified this peak as an artifact of the EOF analysis.

When applying the SMR to geophysical models based on global basis functions we often encounter autocorrelation time scales similar to those shown in Fig. 7.1 that lack a clear gap in the spectrum (Franzke et al. 2005; Franzke and Majda 2006). In such cases it does not matter where we split the EOF spectrum, since the neighboring EOFs have roughly the same time scale. Nevertheless, it is common practice to split the state vector with respect to the explained variance (e.g., Franzke et al. 2005). In other words if the full EOF

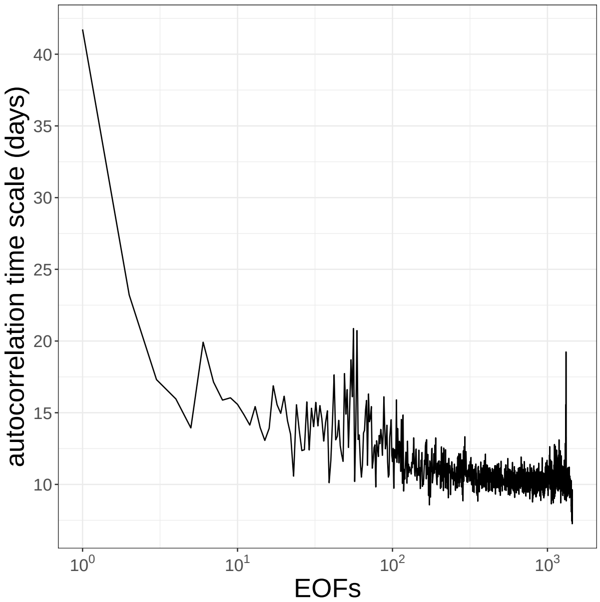

Figure 7.1: Autocorrelation time scale of the EOFs.

space is given by $\text{span}\{\mathbf{e}_1, \mathbf{e}_2, \ldots, \mathbf{e}_N\}$, then we have $\mathbf{x} \in \text{span}\{\mathbf{e}_1, \mathbf{e}_2, \ldots, \mathbf{e}_S\}$, $\mathbf{y} \in \text{span}\{\mathbf{e}_{S+1}, \mathbf{e}_{S+2}, \ldots, \mathbf{e}_{S+F}\}$, and $\mathbf{z} \in \text{span}\{\mathbf{e}_{S+F+1}, \mathbf{e}_{S+F+2}, \ldots, \mathbf{e}_N\}$.

Hence, we obtain, for example, N^{xyz}_{ijk} from the full N by letting $i = 1, 2, \ldots, S$, $j = S+1, S+2, \ldots, S+F$, and $k = S+F+1, S+F+2, \ldots, N$. The remaining tensors are constructed analogously. Note that, because of symmetry, we can choose $\mathsf{N}_{ijk} = 0 \; \forall j > k$ (appendix E) and thus $\mathsf{N}^{\bullet yx} = \mathsf{N}^{\bullet zx} = \mathsf{N}^{\bullet zy} = 0$.

7.2 Intermediate Model

In practice we eliminate the hidden variable $\mathbf{z}$ by parameterizing its effect on the remaining variables:

$$\dot{\mathbf{x}} = \mathbf{F}^x + \mathsf{L}^{xx}\mathbf{x} + \mathsf{N}^{xxx}\mathbf{xx} + \mathsf{L}^{xy}\mathbf{y} + \mathsf{N}^{xxy}\mathbf{xy} + \mathsf{N}^{xyy}\mathbf{yy} + \mathbf{p}^x(\mathbf{x}, \mathbf{y}) \tag{7.4a}$$

$$\dot{\mathbf{y}} = \mathbf{F}^y + \mathsf{L}^{yx}\mathbf{x} + \mathsf{N}^{yxx}\mathbf{xx} + \mathsf{L}^{yy}\mathbf{y} + \mathsf{N}^{yxy}\mathbf{xy} + \mathsf{N}^{yyy}\mathbf{yy} + \mathbf{p}^y(\mathbf{x}, \mathbf{y})\,. \tag{7.4b}$$

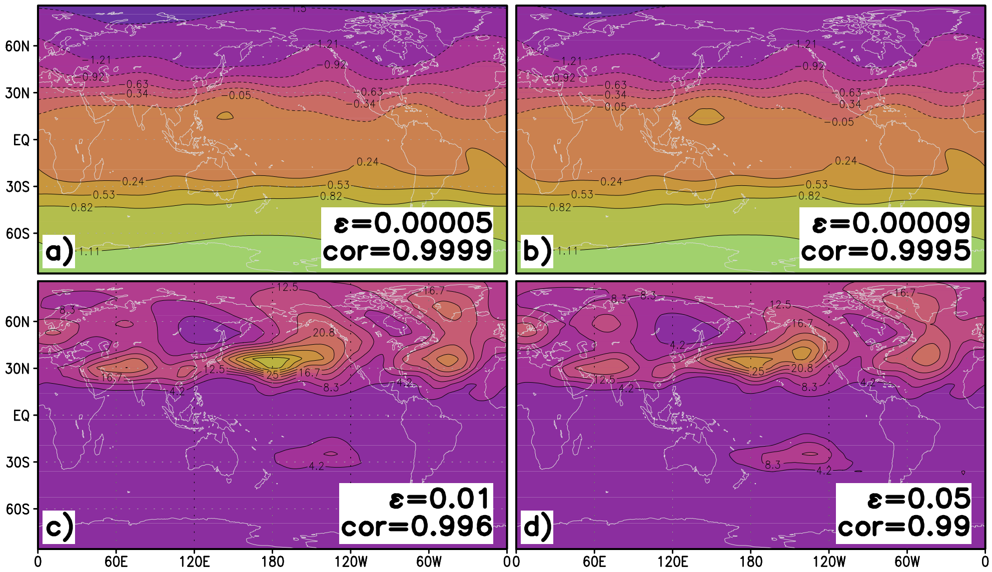

Figure 7.2: As in Fig. 3.2, but for (a),(c) the result of the IMM; (b),(d) the result of the OU-IMM for $(S, F) = (20, 10)$. The output of both models is projected onto the first 20 EOFs (i.e., the slow variable). The relative error and the correlation is calculated between the respective model and the QG3LM (Fig. 8.1) and the same color shading as for the QG3LM is used.

For this we choose a simple linear parameterization as SGS closure

$$\mathbf{p}^x(\mathbf{x},\mathbf{y}) = \mathbf{r}^x + \mathbf{l}^{xx}\mathbf{x} + \mathbf{l}^{xy}\mathbf{y} + \boldsymbol{\epsilon}^x \tag{7.5a}$$

$$\mathbf{p}^y(\mathbf{x},\mathbf{y}) = \mathbf{r}^y + \mathbf{l}^{yx}\mathbf{x} + \mathbf{l}^{yy}\mathbf{y} + \boldsymbol{\epsilon}^y\,, \tag{7.5b}$$

where $\mathbf{r}^\bullet, \mathbf{l}^{\bullet\bullet} = const.$, $\boldsymbol{\epsilon}^\bullet$ is the respective parameterization error, and the dimension is given by the superscripts. The closure is essentially $\mathbf{p}_{\text{det}}$ (3.9) of the SEM and thus is calculated in the same way (appendix B.2). In total the so-called intermediate model (IMM) reads

$$\dot{\mathbf{x}} = \mathbf{F}'^x + \mathsf{L}'^{xx}\mathbf{x} + \mathsf{N}^{xxx}\mathbf{x}\mathbf{x} + \mathsf{L}'^{xy}\mathbf{y} + \mathsf{N}^{xxy}\mathbf{x}\mathbf{y} + \mathsf{N}^{xyy}\mathbf{y}\mathbf{y} \tag{7.6a}$$

$$\dot{\mathbf{y}} = \mathbf{F}'^y + \mathsf{L}'^{yx}\mathbf{x} + \mathsf{N}^{yxx}\mathbf{x}\mathbf{x} + \mathsf{L}'^{yy}\mathbf{y} + \mathsf{N}^{yxy}\mathbf{x}\mathbf{y} + \mathsf{N}^{yyy}\mathbf{y}\mathbf{y}\,, \tag{7.6b}$$

where $\mathbf{F}'^\bullet = \mathbf{F}^\bullet + \mathbf{r}^\bullet$ and $\mathsf{L}'^{\bullet\bullet} = \mathsf{L}^{\bullet\bullet} + \mathbf{l}^{\bullet\bullet}$.

The IMM serves as basis for the construction of the RSM, i.e. we apply the

SMR to this model rather than to the full QG3LM. This allows us to counter the minor conceptual problem arising from replacing the nonlinear self-interaction of the fast variable with an OU-process. By doing so we artificially introduce a stochastic energy source (or sink) in the system. This energy fluctuation does not affect the long-term stability of the model, yet, it suggests a coupling of the system with an additional energy reservoir. The remaining unparameterized part of the hidden variable $\mathbf{z}$ may be seen as this energy reservoir to which the OU-process couples and thus explain the energy fluctuation of the resolved modes. As a positive side effect this reduces the computational effort for the calculation of the SMR closure. Furthermore, applying the SMR on the IMM offers also new opportunities in comparison to the traditional approach (chapter 6) as we will see in chapter 8.

Nevertheless, by taking this approximation the RSM will depend on the quality of the IMM. However, since the IMM is essentially the SEM we expect this to be no problem, at least if we do not perturb the system by an external forcing. Indeed, for $(S, F) = (20, 10)$ the dynamics of the IMM is quite close to the QG3LM as is shown in the mean and covariance of streamfunction in Figs. 7.2a and 7.2c, respectively. The output has been projected onto the slow variable only (i.e., the first 20 EOFs). As for the SEM of part I, the error in the mean streamfunction is negligible $[\mathcal{O}(10^{-4})]$, while the IMM slightly underestimates the covariance of streamfunction of the QG3LM (Fig. 8.1). Nevertheless, the relative amplitude error in the covariance is only $\varepsilon = 0.01$ and the correlation is $cor = 0.996$.

7.2.1 Estimating the Scale-Separation Factor

We evaluate the chosen partition of the EOF space by estimating the scale-separation factor ε for the IMM. Majda et al. (2002) present an approach for calculating the largest scale-separation factor $\varepsilon^\star$ for a three-component additive triad. We expect, however, that a high-dimensional[1] model such as the IMM does not have a global $\varepsilon^\star \ll 1$. Therefore, in the following we adapt the method of Majda et al. (2002) for our case.

---

[1] High dimensional in comparison to the three-component additive triad as considered by Majda et al. (2002).

In the remainder of this section we use Greek letters for indices which are not subject to Einstein's summation convention. Following Majda et al. (2002) we first nondimensionalize the variables by their standard deviations

$$x_\alpha \longrightarrow \mathrm{Sd}^x_\alpha \hat{x}_\alpha \qquad\qquad y_\beta \longrightarrow \mathrm{Sd}^y_\beta \hat{y}_\beta \,, \tag{7.7}$$

where $\alpha = 1, 2, \ldots, S$ and $\beta = 1, 2, \ldots, F$. Inserting this in (7.6) yields

$$\begin{aligned}
\frac{\mathrm{d}\hat{x}_\alpha}{\mathrm{d}t} &= \frac{\mathbf{F}^{\prime x}_\alpha}{\mathrm{Sd}^x_\alpha} + \frac{\mathsf{L}^{\prime xx}_{\alpha j}\mathrm{Sd}^x_j}{\mathrm{Sd}^x_\alpha}\hat{x}_j + \frac{\mathsf{N}^{xxx}_{\alpha jk}\mathrm{Sd}^x_j\mathrm{Sd}^x_k}{\mathrm{Sd}^x_\alpha}\hat{x}_j\hat{x}_k \\
&\quad + \frac{\mathsf{L}^{\prime xy}_{\alpha j}\mathrm{Sd}^y_j}{\mathrm{Sd}^x_\alpha}\hat{y}_j + \frac{\mathsf{N}^{xxy}_{\alpha jk}\mathrm{Sd}^x_j\mathrm{Sd}^y_k}{\mathrm{Sd}^x_\alpha}\hat{x}_j\hat{y}_k + \frac{\mathsf{N}^{xyy}_{\alpha jk}\mathrm{Sd}^y_j\mathrm{Sd}^y_k}{\mathrm{Sd}^x_\alpha}\hat{y}_j\hat{y}_k
\end{aligned} \tag{7.8a}$$

$$\begin{aligned}
\frac{\mathrm{d}\hat{y}_\beta}{\mathrm{d}t} &= \frac{\mathbf{F}^{\prime y}_\beta}{\mathrm{Sd}^y_\beta} + \frac{\mathsf{L}^{\prime yx}_{\beta j}\mathrm{Sd}^x_j}{\mathrm{Sd}^y_\beta}\hat{x}_j + \frac{\mathsf{N}^{yxx}_{\beta jk}\mathrm{Sd}^x_j\mathrm{Sd}^x_k}{\mathrm{Sd}^y_\beta}\hat{x}_j\hat{x}_k + \frac{\mathsf{N}^{yxy}_{\beta jk}\mathrm{Sd}^x_j\mathrm{Sd}^y_k}{\mathrm{Sd}^y_\beta}\hat{x}_j\hat{y}_k \\
&\quad + \frac{\mathsf{L}^{\prime yy}_{\beta j}\mathrm{Sd}^y_j}{\mathrm{Sd}^y_\beta}\hat{y}_j + \frac{\mathsf{N}^{yyy}_{\beta jk}\mathrm{Sd}^y_j\mathrm{Sd}^y_k}{\mathrm{Sd}^y_\beta}\hat{y}_j\hat{y}_k \,.
\end{aligned} \tag{7.8b}$$

The nondimensionalization constants of each component of $f_0(\mathbf{x})$, $f_1(\mathbf{x}, \mathbf{y})$, $g_1(\mathbf{x}, \mathbf{y})$, and $g_2(\mathbf{y})$ are given by

$$\mathsf{F}_{0\alpha} = \max_{j,k}\left\{\frac{|\mathbf{F}^{\prime x}_\alpha|}{\mathrm{Sd}^x_\alpha}, \frac{|\mathsf{L}^{\prime xx}_{\alpha j}|\mathrm{Sd}^x_j}{\mathrm{Sd}^x_\alpha}, \frac{|\mathsf{N}^{xxx}_{\alpha jk}|\mathrm{Sd}^x_j\mathrm{Sd}^x_k}{\mathrm{Sd}^x_\alpha}\right\} \tag{7.9a}$$

$$\mathsf{F}_{1\alpha} = \max_{j,k}\left\{\frac{|\mathsf{L}^{\prime xy}_{\alpha j}|\mathrm{Sd}^y_j}{\mathrm{Sd}^x_\alpha}, \frac{|\mathsf{N}^{xxy}_{\alpha jk}|\mathrm{Sd}^x_j\mathrm{Sd}^y_k}{\mathrm{Sd}^x_\alpha}, \frac{|\mathsf{N}^{xyy}_{\alpha jk}|\mathrm{Sd}^y_j\mathrm{Sd}^y_k}{\mathrm{Sd}^x_\alpha}\right\} \tag{7.9b}$$

$$\mathsf{G}_{1\beta} = \max_{j,k}\left\{\frac{|\mathbf{F}^{\prime y}_\beta|}{\mathrm{Sd}^y_\beta}, \frac{|\mathsf{L}^{\prime yx}_{\beta j}|\mathrm{Sd}^x_j}{\mathrm{Sd}^y_\beta}, \frac{|\mathsf{N}^{yxx}_{\beta jk}|\mathrm{Sd}^x_j\mathrm{Sd}^x_k}{\mathrm{Sd}^y_\beta}, \frac{|\mathsf{N}^{yxy}_{\beta jk}|\mathrm{Sd}^x_j\mathrm{Sd}^y_k}{\mathrm{Sd}^y_\beta}\right\} \tag{7.9c}$$

$$\mathsf{G}_{2\beta} = \max_{j,k}\left\{\frac{|\mathsf{L}^{\prime yy}_{\beta j}|\mathrm{Sd}^y_j}{\mathrm{Sd}^y_\beta}, \frac{|\mathsf{N}^{yyy}_{\beta jk}|\mathrm{Sd}^y_j\mathrm{Sd}^y_k}{\mathrm{Sd}^y_\beta}\right\} \,. \tag{7.9d}$$

Next we identify the maximum of $\mathsf{F}_{0\alpha}$

$$\mathsf{F}^\star_0 = \max_\alpha \mathsf{F}_{0\alpha} \tag{7.10}$$

and use it to nondimensionalize the time:

$$t \longrightarrow \frac{\hat{t}}{\mathsf{F}_0^\star}\,, \tag{7.11}$$

which allows us to write (7.8) shortly as

$$\frac{\mathrm{d}\hat{x}_\alpha}{\mathrm{d}\hat{t}} = \hat{f}_{0\alpha}(\hat{\mathbf{x}}) + \frac{\mathsf{F}_{1\alpha}}{\mathsf{F}_0^\star}\hat{f}_{1\alpha}(\hat{\mathbf{x}},\hat{\mathbf{y}}) \tag{7.12a}$$

$$\frac{\mathrm{d}\hat{y}_\beta}{\mathrm{d}\hat{t}} = \frac{\mathsf{G}_{1\beta}}{\mathsf{F}_0^\star}\hat{g}_{1\beta}(\hat{\mathbf{x}},\hat{\mathbf{y}}) + \frac{\mathsf{G}_{2\beta}}{\mathsf{F}_0^\star}\hat{g}_{2\beta}(\hat{\mathbf{y}})\,. \tag{7.12b}$$

For the application of the SMR we require

$$\frac{1}{\varepsilon} \approx \frac{\mathsf{F}_{1\alpha}}{\mathsf{F}_0^\star} \approx \frac{\mathsf{G}_{1\beta}}{\mathsf{F}_0^\star} \approx \sqrt{\frac{\mathsf{G}_{2\beta}}{\mathsf{F}_0^\star}} \tag{7.13}$$

with $\varepsilon \ll 1\ \forall \alpha, \beta$.

In practice this requirement is only approximately fulfilled (see section 8.2.2). Nevertheless, we assume that this is sufficient for the application of the SMR and thus write (7.6) as

$$\mathrm{d}\mathbf{x} = (\mathbf{F}'^{x} + \mathsf{L}'^{xx}\mathbf{x} + \mathsf{N}^{xxx}\mathbf{x}\mathbf{x})\,\mathrm{d}t + \frac{1}{\varepsilon}\left(\mathsf{L}'^{xy}\mathbf{y} + \mathsf{N}^{xxy}\mathbf{x}\mathbf{y} + \mathsf{N}^{xyy}\mathbf{y}\mathbf{y}\right)\mathrm{d}t \tag{7.14a}$$

$$\mathrm{d}\mathbf{y} = \frac{1}{\varepsilon}\left(\mathbf{F}'^{y} + \mathsf{L}'^{yx}\mathbf{x} + \mathsf{N}^{yxx}\mathbf{x}\mathbf{x} + \mathsf{N}^{yxy}\mathbf{x}\mathbf{y} + \mathsf{L}'^{yy}\mathbf{y}\right)\mathrm{d}t + \frac{1}{\varepsilon^2}\mathsf{N}^{yyy}\mathbf{y}\mathbf{y}\mathrm{d}t\,, \tag{7.14b}$$

where we suppressed the hats for convenience.

7.3 Ornstein-Uhlenbeck Intermediate Model

The next step in the application of the SMR is the replacement of the self-interaction of the fast variable with an OU-process. For this we solve (7.14b) for the terms of order ε^{-2}, approximate the tendency by finite differences, and apply the Maximum-Likelihood Method as described in appendix B.2. However, it is crucial that we use the tendency of the full QG3LM instead of the IMMs' tendency in this step. This way we are effectively replacing $\mathsf{N}^{yyy} + \boldsymbol{\epsilon}^y$ [where $\boldsymbol{\epsilon}^y$ is the residual error of the IMM closure (7.5b)] and thus can account for the remaining unparameterized part of the hidden variable $\mathbf{z}$ in the OU-process. This results in the Ornstein-Uhlenbeck intermediate model (OU-IMM)

$$\mathrm{d}\mathbf{x} = (\mathbf{F}'^{x} + \boldsymbol{\mathsf{L}}'^{xx}\mathbf{x} + \boldsymbol{\mathsf{N}}^{xxx}\mathbf{x}\mathbf{x})\mathrm{d}t + \frac{1}{\varepsilon}(\boldsymbol{\mathsf{L}}'^{xy}\mathbf{y} + \boldsymbol{\mathsf{N}}^{xxy}\mathbf{x}\mathbf{y} + \boldsymbol{\mathsf{N}}^{xyy}\mathbf{y}\mathbf{y})\mathrm{d}t \tag{7.15a}$$

$$\begin{aligned}\mathrm{d}\mathbf{y} &= \frac{1}{\varepsilon}(\mathbf{F}'^{y} + \boldsymbol{\mathsf{L}}'^{yx}\mathbf{x} + \boldsymbol{\mathsf{N}}^{yxx}\mathbf{x}\mathbf{x} + \boldsymbol{\mathsf{N}}^{yxy}\mathbf{x}\mathbf{y} + \boldsymbol{\mathsf{L}}'^{yy}\mathbf{y})\mathrm{d}t \\ &\quad + \frac{1}{\varepsilon^2}\mathbf{l}^{yy}_{\mathrm{OU}}\mathbf{y}\mathrm{d}t + \boldsymbol{\sigma}^{y}\mathrm{d}\mathbf{W}^{y}\,.\end{aligned} \tag{7.15b}$$

Similar to the IMM, we consider the OU-IMM as a step towards the construction of the RSM. Thus, we pass on a rigorous investigation of the performance of this model. Instead, we compare the IMM and OU-IMM for the special case of $(S,F) = (20,10)$ in Fig. 7.2. In particular, Figs. 7.2a and 7.2c show the mean and covariance of the IMM whereas Figs. 7.2b and 7.2d display the the respective results of the OU-IMM. While the mean is virtually identical, the covariance changes more prominently. Overall, the amplitude of covariance is slightly reduced. Furthermore, the OU-IMM experiences two maxima over the Pacific Ocean whereas the IMM (and QG3LM) only has one distinct maximum. In comparison to the IMM the relative error in the covariance increases by a factor of 5, yet it is still of order $\mathcal{O}(10^{-2})$ while the correlation of the OU-IMM is $cor = 0.99$.

7.4 Bare Truncation Model

Before we investigate the RSM in detail we first introduce the so-called bare truncation model (BTM). The BTM is the RSM without the closure following from the SMR:

$$\mathrm{d}\mathbf{x} = (\boldsymbol{\mathsf{F}}'^{x} + \boldsymbol{\mathsf{L}}'^{xx}\mathbf{x} + \boldsymbol{\mathsf{N}}^{xxx}\mathbf{x}\mathbf{x})\mathrm{d}t\,, \tag{7.16}$$

which allows us to evaluate the effect of the SMR closure directly.

We should note, however, that the BTM used in this thesis differs slightly from the classical definition in literature (e.g., Franzke and Majda 2006; Dolaptchiev et al. 2013a; Zacharuk et al. 2018). Usually, the BTM contains only the interaction coefficients of the slow variable $\mathbf{x}$. Yet, in our case we use $f_0(\mathbf{x})$ of the IMM (7.14b), which contains the additional empirical closure of the hidden variable $\mathbf{z}$. In fact, the BTM as defined in literature diverges in our case if $S \lesssim 200$.

Chapter 8

Results

In this chapter we investigate the RSM obtained from applying the SMR to the QG3LM. In the following we introduce the general setup of the numerical simulations concerning the SMR. The remaining chapter is then split into the respective experiments. In particular, we are investigating the performance of the RSM and, for a perturbed climate, the quality of the anomalous RSM. Furthermore, we exploit the fact that we apply the SMR to a subspace rather than to the full QG3LM. This allows us to go beyond the classical SMR and include explicitly the nonlinear self-interaction of the fast variable (i.e., N^{yyy}) in the SMR closure.

8.1 The General Simulation Setup

For the investigation of the RSM we consider four different dimensions of the slow variable ($\mathbf{x} \in \mathbb{R}^S$, $S \in \{10, 20, 30, 50\}$) each with four dimensions of the fast variable ($\mathbf{y} \in \mathbb{R}^F$, $F \in \{5, 10, 20, 30\}$). The corresponding dimension of the hidden variable ($\mathbf{z} \in \mathbb{R}^H$) can be calculated by $H = N - S - F$, where $N = 1449$. In contrast to part I, we integrate the models only 3×10^5 days, since this is sufficient to tune the OU-process. Nevertheless, we again discard the first 10 000 days to eliminate potential spinup effects. The quantitative evaluation of the results is done using the relative amplitude error as defined in (5.1), however, computed on the grid instead of in the EOF space.

As for the SEM in part I, we adjust the hyperdiffusion by changing the diffusion

Table 8.1: Adjusted diffusion time scale (days) that is used in the RSM. The original value is $\tau_H = 2$ days.

$S+F$	15	20	25	30	35	40	50	55	60	70	80
τ_H	1.2	0.7	1.2	1.5	1.5	1.6	1.2	1.2	1.2	1.2	1.0

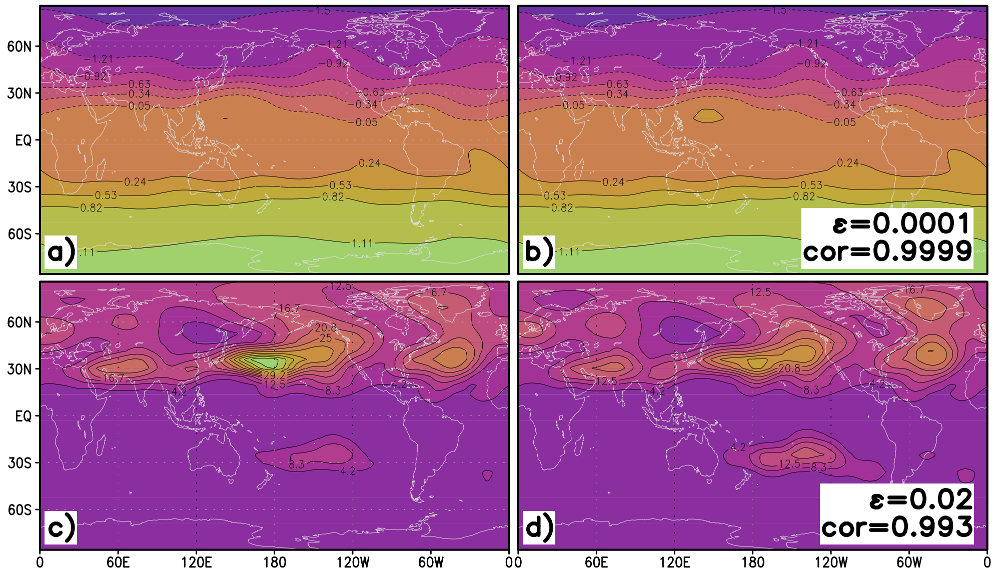

Figure 8.1: As in Fig. 7.2, but for (a),(c) the QG3LM; (b),(d) the result of the RSM.

time scale τ_H. The numerical values for the following simulations are given in Table 8.1.

8.2 Reduced Stochastic Model

8.2.1 Numerical Experiments

Before we analyze the performance of the RSM systematically, we first consider the case with $(S, F) = (20, 10)$. This truncation corresponds to the results of the IMM and OU-IMM (Fig. 7.2) in the previous chapter. Figure 8.1 shows the mean streamfunction and covariance of streamfunction of the RSM in comparison to the QG3LM. The RSM is able to reproduce the mean streamfunction of the QG3LM

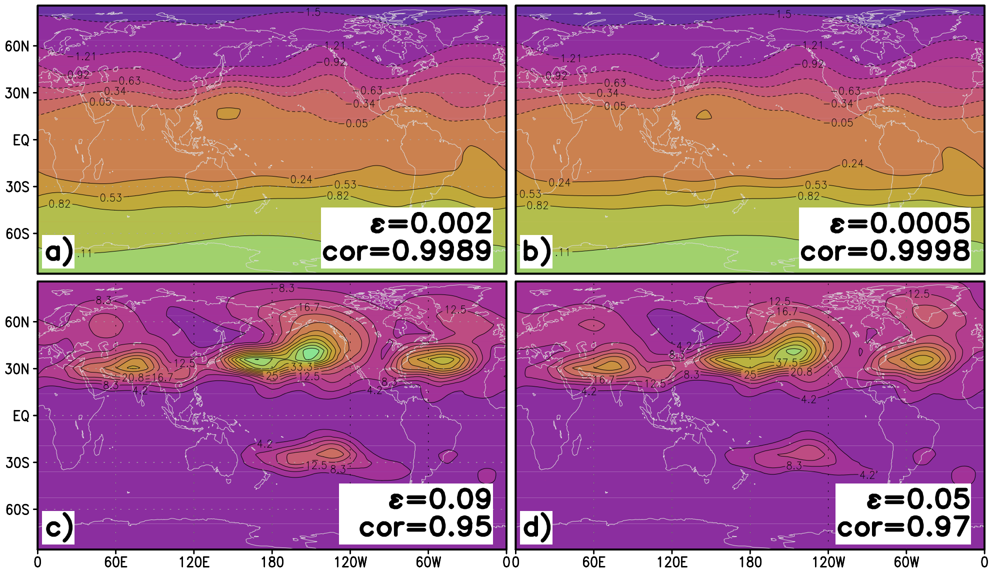

Figure 8.2: As in Fig. 7.2, but for (a),(c) the BTM; (b),(d) the SEM.

with a relative amplitude error of $\varepsilon = \mathcal{O}(10^{-4})$ and a correlation of $cor \approx 1$. For the covariance of streamfunction the RSM underestimates the amplitude over the Pacific Ocean. On the other hand, the amplitude of the side maxima over India and the Atlantic Ocean are well reproduced, resulting in $\varepsilon = 0.02$ and $cor = 0.993$.

The SMR closure has indeed a positive effect on the reduced model. In comparison to the RSM the BTM exhibits both in the mean streamfunction (Fig. 8.2a) and the covariance of streamfunction (Fig.8.2c) an increase in relative amplitude error of a factor of 10 and 3, respectively. This decrease of performance is irrelevant for the mean streamfunction. Yet, for the covariance of the streamfunction the BTM clearly overestimates the amplitude, not only for the maximum over the Pacific Ocean but also for the side maxima over the Atlantic Ocean and India. Similar behavior is shown by the SEM (Figs. 8.2b and 8.2d). This model also overestimates the covariance of streamfunction, although not as much as the BTM, resulting in $\varepsilon = 0.05$ and $cor = 0.97$. Thus, we might summarize that the RSM tends to underestimate the covariance while the conventional data-driven approach (SEM) slightly overestimates the covariance of the streamfunction.

In Fig. 8.3 and Fig. 8.4 we show for various (S, F) the relative error of the RSM, BTM, and SEM for the mean streamfunction and covariance of the streamfunction,

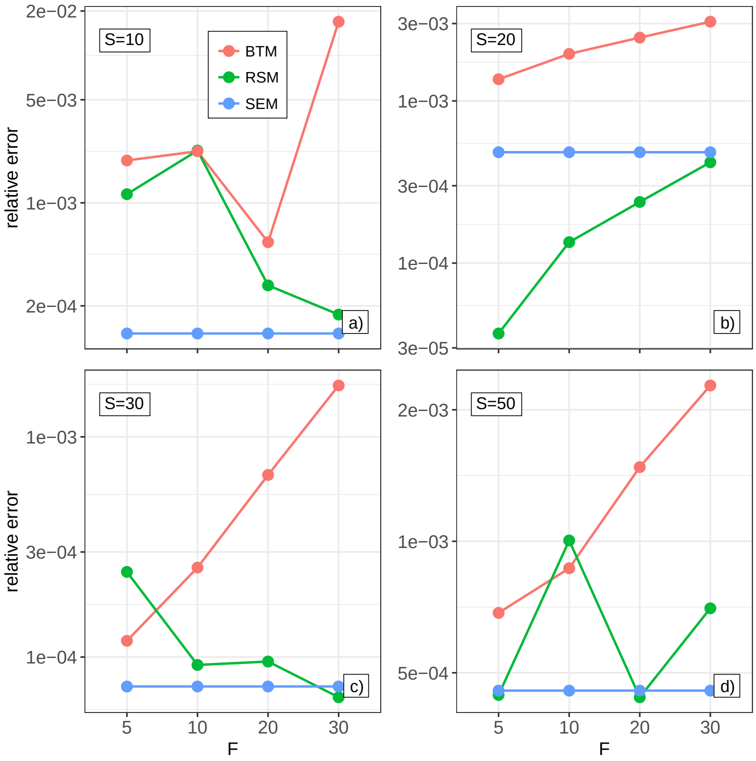

Figure 8.3: Relative error of the mean streamfunction of the RSM in comparison to the BTM and SEM for various combinations of $S \in \{10, 20, 30, 50\}$ and $F \in \{5, 10, 20, 30\}$.

respectively. First we note that by design the SEM is independent of F, since only the slow variable is described explicitly and both $\mathbf{y}$ and $\mathbf{z}$ are treated with the data-driven parameterization. Furthermore, we observe not much variation of the SEM with respect to S. In contrast, the error of the BTM increases significantly with increasing dimension of the fast variable. This effect is strongest for $S = 10$, which is unsurprising since the BTM neglects the impact of the fast variable completely. On the other hand, the RSM is only weakly dependent (in first approximation even independent) on F and experiences only small variations with respect to S. Furthermore, for the majority of the considered cases the RSM outperforms the BTM significantly, especially for large F. Yet, for a few combinations of large S and small F the BTM is comparable to or even slightly better than the RSM, respectively. In comparison to the SEM, the RSM seems to be qualitatively and quantitatively similar. Nevertheless, only for $S = 20$ the RSM is able to systematically outperform the SEM. However, as we have already seen in the example with $(S, F) = (20, 10)$ (Fig. 8.1 and Fig. 8.2) the difference between the RSM and SEM is relatively small.

8.2.2 Discussion

We found that the performance of the RSM seems to be (nearly) independent of the chosen (S, F) (Fig. 8.3 and Fig. 8.4). Yet, we investigated only a small range of these parameters. We expect that, if we increase (S, F) further, we would eventually find a combination where the RSM (or rather the assumption of scale separation) breaks down. Nevertheless, selected tests with F up to 100 showed no decrease in performance. The reason for this is the actual unimportance of $\mathbf{N}^{yyy}$ in (7.14b). If we run the IMM with and without the nonlinear self-interaction of the fast variable, we find nearly no difference in the model output (Fig. 8.5). This is supported by the fact that we cannot construct a RSM if we use the tendency of the IMM when fitting the OU-process, since the latter would practically be zero. Thus, the required scale separation is caused by the remaining unparameterized effects of $\mathbf{z}$ in the IMM closure [i.e., $\boldsymbol{\epsilon}^y$ in (7.5b)]. Consequently, when increasing F we simply shift the importance of $\boldsymbol{\epsilon}^y$ to $\mathbf{N}^{yyy}$, which should not affect the scaling of the fitted OU-process. Of course, the situation is completely different when

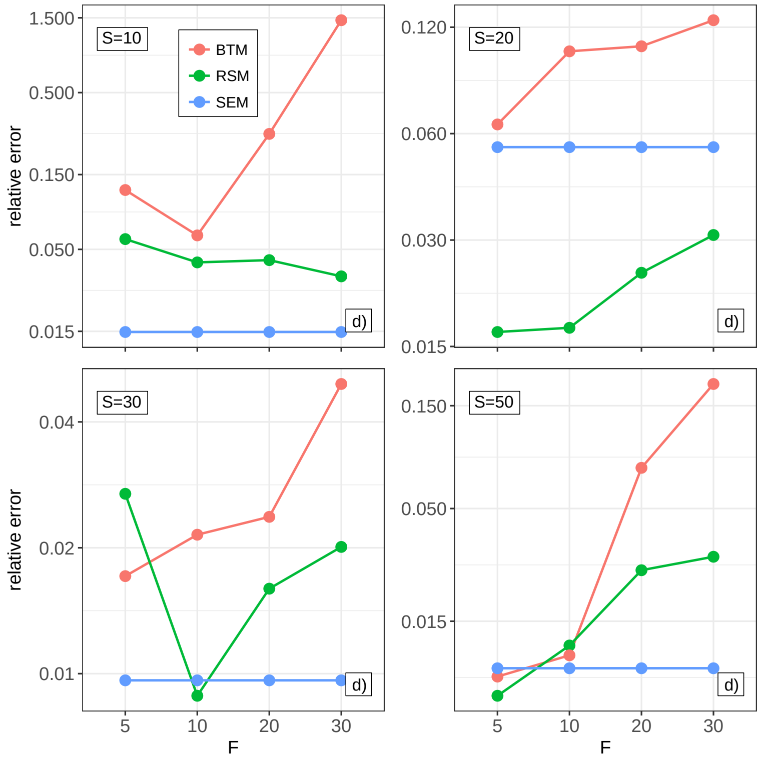

Figure 8.4: As in Fig. 8.3, but for relative error in covariance of streamfunction.

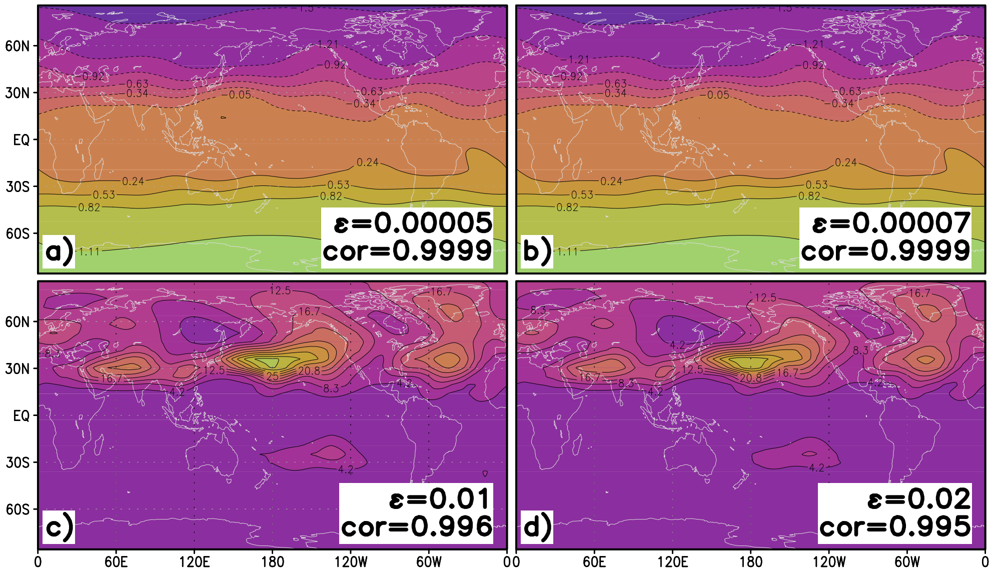

Figure 8.5: As in Fig. 7.2, but for (a),(c) the IMM; (b),(d) the IMM with $\mathbf{N}^{yyy} = 0$.

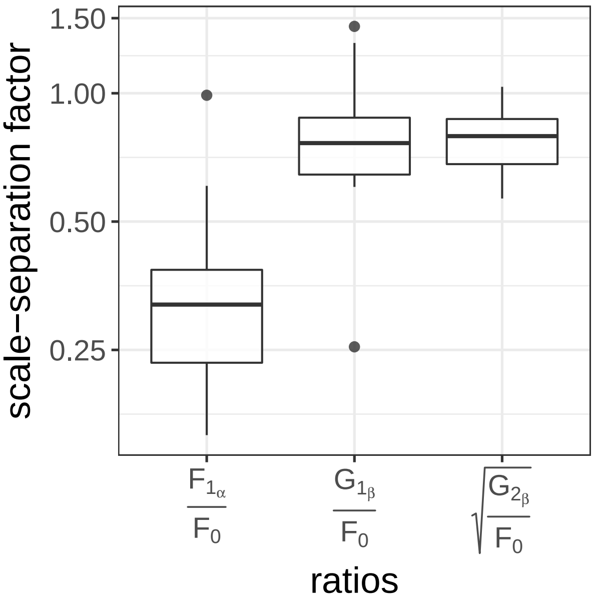

Figure 8.6: Boxplot with values of the scale-separation factors (7.13) for the OU-IMM with $(S, F) = (20, 10)$.

changing S instead of F. Looking at the autocorrelation time scale (Fig. 7.1) we see that if we increase S we will eventually have enough "fast" components in $\mathbf{x}$ to violate the assumption of scale separation. However, given the fact that the SMR closure contains a cubic term in $\mathbf{x}$ (6.34d) such large S are undesired anyway.

Instead of directly investigating the performance of the SMR with respect to (S, F), we might simply estimate the scale-separation factor as described in section 7.2.1. In Fig. 8.6 we show a boxplot of all components of the respective scale-separation (7.13) of the OU-IMM. Overall, all three distributions show a median well below 1. For the ratio $\mathsf{F}_1/\mathsf{F}_0$ we find no scale separation > 1. Consequently, the corresponding smallest scale-separation factor ($\varepsilon^\star$) reads $\varepsilon^\star_{\mathsf{F}_1} = 1.01$. For $[\mathsf{G}_2/\mathsf{F}_0]^{\frac{1}{2}}$ the result is only marginally better with one component slightly larger than 1 ($\varepsilon^\star_{\mathsf{G}_2} = 0.97$). On the other hand, for $\mathsf{G}_1/\mathsf{F}_0$ 20% of the components are larger than 1 and the smallest scale-separation factor reads $\varepsilon^\star_{\mathsf{G}_1} = 0.70$. We would not have expected to see that all components of the ratios show a clear scale-separation. Nevertheless, even if we assume that the components corresponding to $\varepsilon^\star$ are dominating Fig. 8.6 suggests no scale-separation within the equation of the slow variable while for $\mathbf{y}$ the coupling terms seem to dominate the OU-process. However, as seen in Fig. 8.6 we find that the RSM performs quite well if we assume the classical SMR scaling (7.14). This indicates that (7.13) is not a suitable a priori measure of the applicability of the SMR especially since we would expect an even unclearer result for larger (S, F).

The contradicting result of $\varepsilon^\star$ and the performance of the RSM suggests that the estimation of the scale-separation factor in section 7.2.1 is, at least partly, incorrect. Most likely the nonlinear terms have been falsely nondimensionalized. As Majda et al. (2002) has stated the nondimensionalization of the variables by their standard deviations only holds on average. Thus, by using the same nondimensionalization constant for the nonlinear terms we effectively assume, for example $\langle \mathbf{x}\mathbf{y}^{\mathrm{T}} \rangle = \langle \mathbf{x} \rangle \langle \mathbf{y}^{\mathrm{T}} \rangle$, which is in general not true. Consequently, $\hat{f}_{0\alpha}$, $\hat{f}_{1\alpha}$, and $\hat{g}_{1\beta}$ in (7.12) might not be of $\mathcal{O}(1)$.

Fact is that the performance of the RSM is remarkably good. Franzke and Majda (2006) applied the SMR to the same model but run only in northern hemispheric mode. Their resulting RSM showed significantly less accuracy as the results presented in this thesis. In general, Franzke and Majda (2006) observed an underestimation of the amplitudes of various fields (e.g., streamfunction, eddy forcing) by a factor varying between 1.5 and 6. Furthermore, their RSM experienced a climatic drift, which had to be corrected by empirical fitting (i.e., adjusting the amplitudes of various terms in the SMR closure). In return this allowed them to obtain correlations above 0.95 for both the mean and standard deviation of the streamfunction, respectively.

To understand the difference in RSM performance we have to compare the assumptions leading to the respective RSMs. In contrast to the setup used here (chapter 6 and chapter 7), Franzke and Majda (2006) applied the so-called seamless SMR (Franzke et al. 2005). Instead of fitting an OU-process explicitly and using its variance D to calculate the SMR closure (6.34), the seamless SMR estimates the required correlations (i.e., $\langle \mathbf{y}\mathbf{y}^{\mathrm{T}} \rangle$ and $\langle \mathbf{y}\mathbf{y}^{\mathrm{T}}(t) \rangle$) directly from data. Furthermore, Franzke and Majda (2006) assume these correlations to be diagonal. This corresponds to a diagonal drift term $\mathbf{l}_{\mathrm{OU}}^{yy}$ in the OU-process. Lastly, they apply the seamless SMR to their full QG3LM with $S \leq 10$.

RSMs constructed with a diagonal $\mathbf{l}_{\mathrm{OU}}^{yy}$ caused no significant decrease in model performance (not shown). Hence, only the presence of the hidden variable can

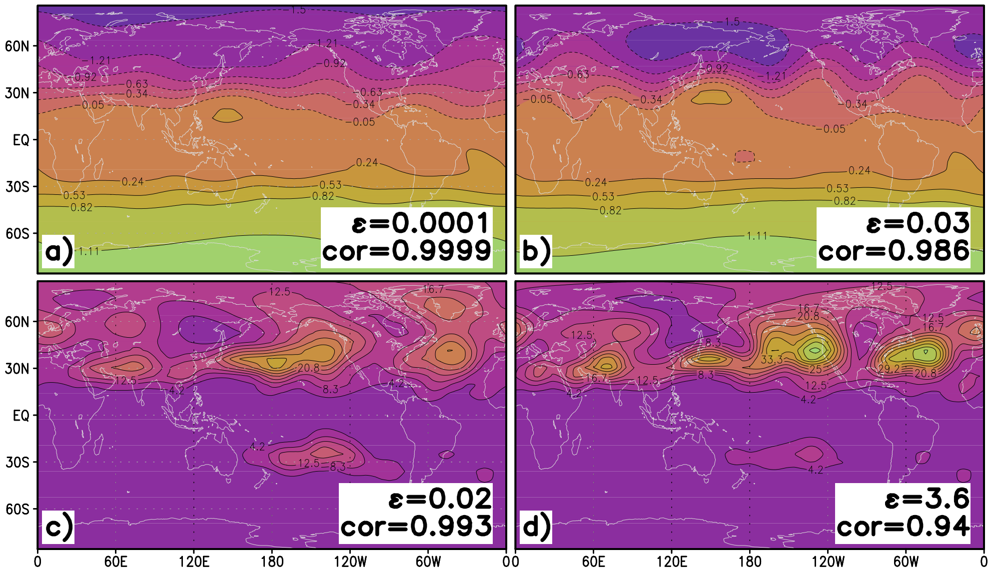

Figure 8.7: As in Fig. 7.2, but for (a),(c) the RSM; (b),(d) the result of the RSM-x_{off}. The units and the color shading are the same for each row, but (d) has been divided by a factor of 5.

cause the improved performance of our RSM. Unfortunately, for technical reasons a corresponding simulation with $H = 0$ (i.e., no hidden variable) has not been done yet. However, as discussed above we would not expect worse results for large F. On the other hand, Franzke and Majda (2006) identified the bare truncation part as the source of their climatic drift. Consequently, their additional empirical weighting of the RSM terms suppressed the bare truncation part in favor of the SMR closure terms. In this thesis, we introduce an empirical closure in the bare truncation part because of the hidden variable. To analyze its effect on the RSM we show in Fig. 8.7 the RSM for $(S, F) = (20, 10)$ with and without the empirical closure in the bare truncation part (RSM-x_{off}), respectively. The mean streamfunction of the RSM-x_{off} (Fig. 8.7b) shows differences compared to the standard RSM (Fig. 8.7a), such as the multiple local minima at 60°N. This results in a relative amplitude error of $\varepsilon = 0.03$ and a correlation of $cor = 0.986$. While the absolute value of ε is still quite low it is several orders of magnitude higher than for all considered reduced models so far. Furthermore, the RSM-x_{off} significantly overestimates the covariance of streamfunction (Fig. 8.7d) also seen by the relative amplitude error of $\varepsilon = 3.6$. In fact, to reveal the structure of the covariance of streamfunction of the RSM-$\mathrm{x}_{\mathrm{off}}$ Fig. 8.7d had to be divided by a factor of 5. The overall covariance pattern is reproduced ($cor = 0.94$), yet, we find that the global maximum is shifted from the Pacific to the Atlantic Ocean, respectively.

The empirical closure in the bare truncation part has obviously a significant effect on the RSM. However, tests with relatively large F (up to $F = 100$; not shown) revealed no decrease in the performance of the RSM. Nevertheless, the larger F the less important the empirical closure in the bare truncation part should become. Thus, it remains to be seen how our RSM performs when constructed from the full QG3LM before we can conclude our comparison to Franzke and Majda (2006).

8.3 Anomalous Reduced Stochastic Model

8.3.1 Analytic Results

Since the SMR is constrained by first principles, the theory automatically accounts for the effect of an external forcing on the SGS closure. In fact, the calculation of the closure (6.34) stays exactly the same, merely the explicit coefficients (see appendix E) have to be adjusted. In particular, for a time independent constant anomalous forcing δf, as considered in section 4.1, the new constant interaction coefficient reads

$$\mathbf{F}_l \longrightarrow \mathbf{F}_l + \delta f_l \,, \tag{8.1}$$

where $\delta f, \mathbf{F} \in \mathbb{R}^N$. The change of the constant interaction coefficient yields two additional terms in (6.32) given by

$$- \left[\delta f^x + \int_0^\infty \mathbb{E} \left[\{ \delta f^y \cdot \mathsf{D}^{-1} \mathbf{y} \} f_1(\mathbf{x}, \mathbf{y}[\tau]) \right]_{\mathrm{OU}} \mathrm{d}\tau \right] \cdot \nabla_x p^{(0)} \,. \tag{8.2}$$

Thus, the constant (6.34a) and linear (6.34b) part of the SMR closure, respectively, are modified by

$$\boldsymbol{\mathcal{F}}_i \longrightarrow \boldsymbol{\mathcal{F}}_i + \delta f^y_j \mathsf{L}^{xy}_{ik} \mathsf{K}_{kj} \tag{8.3a}$$

$$\boldsymbol{\mathcal{L}}_{ij} \longrightarrow \boldsymbol{\mathcal{L}}_{ij} + \delta f^y_k (\mathbf{N}^{xxy}_{ijl} + \mathbf{N}^{xyx}_{ilj}) \mathbf{K}_{lk} \,. \tag{8.3b}$$

We call the resulting model the a priori RSM (apr-RSM).

Limits of the Closure Correction

The closure correction in (8.3) fails for external forcings that are too strong. In general, we can write the perturbed IMM as

$$\mathrm{d}\mathbf{x} = f_0(\mathbf{x})\mathrm{d}t + \frac{1}{\varepsilon} f_1(\mathbf{x}, \mathbf{y})\mathrm{d}t + \beta_x \delta f^x \mathrm{d}t \tag{8.4a}$$

$$\mathrm{d}\mathbf{y} = g_0 \mathrm{d}t + \frac{1}{\varepsilon} g_1(\mathbf{x}, \mathbf{y})\mathrm{d}t + \frac{1}{\varepsilon^2} g_2(\mathbf{y})\mathrm{d}t + \frac{1}{\varepsilon} \boldsymbol{\sigma}^{\star y} \mathrm{d}\mathbf{W}^y + \beta_y \delta f^y \mathrm{d}t \,, \tag{8.4b}$$

where β_x, β_y indicate the order of the scale separation (i.e., $\beta_x \in \{0, 1, \varepsilon^{-1}\}$ and $\beta_y \in \{0, \varepsilon^{-1}, \varepsilon^{-2}\}$). Setting $\beta_x = \beta_y = 0$ yields the unperturbed IMM (7.6) while $\beta_y = 1$ is not of interest since such small forcings would have no effect on SMR closure.

Depending on the order of scale separation, several cases occur:

1.) $\beta_x \in \{0, 1\}, \beta_y = \varepsilon^{-1}$

In this case the above mentioned closure correction (8.3) is obtained. In particular, the case with $\beta_x = 0$ is of interest since then the external forcing is acting only on the SGS processes. Consequently, a common data-driven model (e.g., the SEM in section 3.2) is unable to respond at all, while the RSM is able to react to such a forcing.

2.) $\beta_x = \varepsilon^{-1}$

If the forcing in the slow variable is too strong, we end up modifying

$$f_1(\mathbf{x}, \mathbf{y}) \longrightarrow f_1(\mathbf{x}, \mathbf{y}) + \delta f^x \,. \tag{8.5}$$

This results in a new solvability condition given by

$$0 = \left(\delta f_i^x + \mathsf{N}_{ijk}^{xyy}\mathsf{D}_{jk}\right) \frac{\partial p^{(0)}}{\partial x_i}\,. \tag{8.6}$$

However, we assume that the original solvability condition (6.28) is correct. Thus, the modified version can only be fulfilled if the gradient of probability changes in such a way that the scalar product vanishes. In general, this is not necessarily given. Consequently, the SMR cannot be derived and the RSM would not be applicable.

In principle it is possible to correct for the term violating the solvability condition. Yet, this introduces a correction in (6.32), which is of $\mathcal{O}(\varepsilon^{-1})$ (Papanicolaou 1976; Demaeyer and Vannitsem 2018). However, this correction is not considered in this thesis. Instead, in the following anomaly experiments we avoid this case by choosing a sufficiently small external forcing.

3.) $\beta_x \in \{0,1\}, \beta_y = \varepsilon^{-2}$

In this case the fast variable is dominated by a constant and we have

$$f_0(\mathbf{x}) \longrightarrow f_0(\mathbf{x}) + \delta f^x, \quad \text{if } \beta_x = 1 \tag{8.7a}$$

$$g_2(\mathbf{y}) \longrightarrow g_2(\mathbf{y}) + \delta f^y\,. \tag{8.7b}$$

The modification of $g_2(\mathbf{y})$ corresponds to a strong anomalous forcing in the fast variable. Consequently, the OU-process experiences a mean value. In return this modifies the solvability condition:

$$0 = \left\{[\mathsf{L}_{ij}^{xy} + (\mathsf{N}_{ikj}^{xxy} + \mathsf{N}_{ijk}^{xyx})\mathbf{x}_k]\mathbb{E}\left[\mathbf{y}_j\right]_{\mathrm{OU}} + \mathsf{N}_{ijk}^{xyy}\mathbb{E}\left[\mathbf{y}_j\mathbf{y}_k\right]_{\mathrm{OU}}\right\} \frac{\partial p^{(0)}}{\partial x_i} \tag{8.8}$$

$$= \left\{[\mathsf{L}_{ij}^{xy} + (\mathsf{N}_{ikj}^{xxy} + \mathsf{N}_{ijk}^{xyx})\mathbf{x}_k]\delta f_j^y + \mathsf{N}_{ijk}^{xyy}\mathsf{D}_{jk}\right\} \frac{\partial p^{(0)}}{\partial x_i}\,, \tag{8.9}$$

since odd moments of the OU-process no longer vanish. Consequently, the SMR cannot be applied unless it is modified as discussed in **2.)**. Furthermore, additional closure terms would occur since during the derivation of the RSM we made repeatedly use of the fact that odd moments vanish.

Update Empirical Part with the Fluctuation-Dissipation Theorem

Even if the closure correction (8.3) is applicable, we might improve the RSM even further if we also retune the OU-process and the empirical $\mathbf{z}$ closure from a perturbed climate simulation of the QG3LM. This would result in what we call the a posteriori RSM (apo-RSM). However, this is impossible for realistic settings. Instead, we use the qG-FDT to estimate the update of the empirical part in both the $\mathbf{z}$ closure and the OU-process as introduced in part I, resulting in a modification of $\mathbf{K}$ (6.39), $\mathbf{P}$ (6.40), and various interaction coefficients (7.6) and thus a change of all components of the RSM closure (6.34).

8.3.2 Setup

In contrast to the general setup (section 8.1), we investigate the robustness of the RSM against a perturbed climate only for $(S, F) = (20, 10)$. As external forcing we use the local anomalous forcing of part I (see section 4.1). In analogy to the FDT experiments we are considering 12 forcing positions $\lambda_c \in \{0°, 30°, \dots, 330°\}$. However, in contrast to part I we do not restrict the forcing to the first 20 EOFs only.

For the SMR anomaly experiments we compare the following models:

- apr-RSM: Using the SMR closure with the corresponding correction terms from the theory.
- apo-RSM: Using the perfect (a posteriori) parameterization by retuning the empirical OU-process and the empirical closure to the perturbed data set (impossible in realistic settings).
- FDT-RSM: As the apr-RSM, however, additionally the OU-process and the empirical closure is updated with the qG-FDT.
- apr-SEM: Using the a priori parameterization of the unforced case (4.3). This simulates the state-of-the-art case of using a GCM for sensitivity studies without retuning any empirical parameters.
- FDT-SEM: Updating the parameterization with the help of the qG-FDT as presented in part I.

For the evaluation of the perturbed models we again focus on the 200 hPa layer. Furthermore, we are investigating two different forcing cases:

- Forcing all scales: The external forcing acts on both the slow and fast variable, respectively (i.e., $\delta f \in \mathbb{R}^{S+F}$ where $\delta f_i \neq 0, \forall i$).
- Forcing the SGS: The external forcing acts only on the fast variable (i.e., $\delta f \in \mathbb{R}^{S+F}$ where $\delta f_i = 0, \forall i \leq S$).

8.3.3 Numerical Experiments

Anomaly Experiment: Forcing all Scales

For certain (S, F) the RSM is able to reproduce the QG3LM qualitatively and quantitatively in terms of both mean and covariance of streamfunction, respectively. Nevertheless, since the SMR is based mainly on first principle, we are particularly interested in the performance of the RSM in a perturbed climate. Before we conduct the anomaly experiments, however, we require an appropriate forcing. Using the original one in (4.1) results in a response in the QG3LM that is too weak to be significant with respect to the bias of the unforced RSM. Consequently, the potentially correct response of the forced RSM might be masked by the underlying bias. Therefore, we introduce an additional amplitude factor $\alpha_{\text{all}} \in \mathbb{R}$ with which we multiply the local anomalous forcing (4.1). We compute α_{all} by perturbing the QG3LM and measure its response in terms of a relative deviation which in turn is compared to the relative error of the unforced RSM (i.e., its bias). As can be seen in Fig. 8.8 an amplitude factor of $\alpha_{\text{all}} = 15$ is sufficient.

In Fig. 8.9 we show, as an example, the response in covariance of streamfunction for an anomalous forcing located at $\lambda_c = 210°$. In Fig. 8.9a we see the response of the QG3LM projected on the slow variable (i.e., the first 20 EOFs). The QG3LM experiences three distinct maxima over Eastern Europe, Western Canada, and Greenland. Furthermore, we find a weak minimum over the Pacific Ocean. Figure 8.9b shows the response of covariance of the apr-RSM. In contrast to the reference, this model has a weak global minimum over the northern hemisphere and multiple isolated maxima at 30°N, resulting in a correlation of $\mathit{cor} = 0.80$ and a relative amplitude error of $\varepsilon = 1.37$. The apo-RSM (Fig. 8.9c) fairs better.

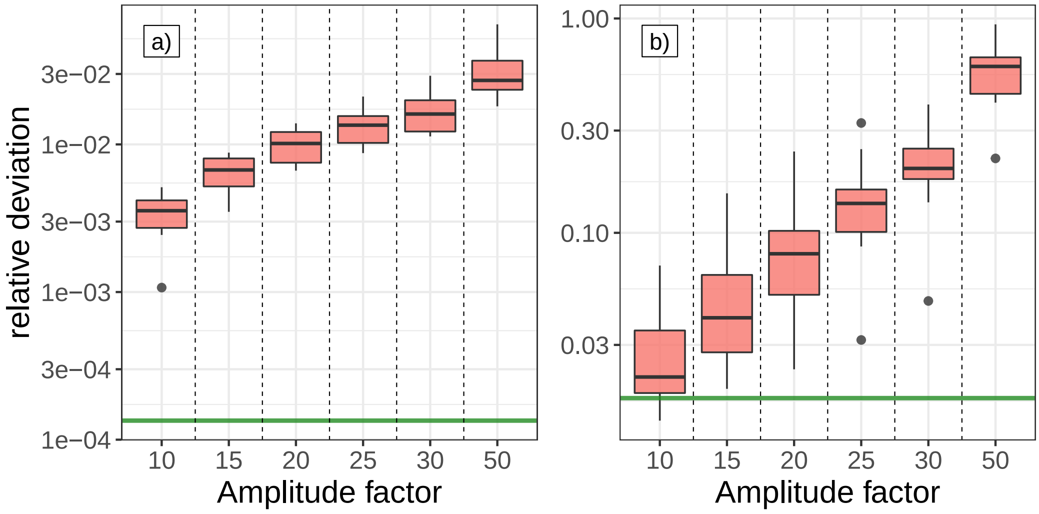

Figure 8.8: Strength of the response of the QG3LM in comparison to the bias of the unforced RSM with $(S, F) = (20, 10)$. The boxplot shows the relative deviation of (a) mean streamfunction and (b) covariance of streamfunction between the perturbed and unforced QG3LM for various amplitude factors of the anomalous forcing acting on all scales. The green line is the relative error between the unforced RSM and QG3LM.

The overall pattern of the response is reproduced ($cor = 0.96$), however, the amplitude of the maximum at Western Canada is slightly underestimated. Still, the apo-RSM has a relative amplitude error of only $\varepsilon = 0.10$. Figure 8.9d shows the response of the FDT-RSM divided by a factor of 25. This reveals a relatively good reconstruction of the pattern ($cor = 0.91$). Nevertheless, in general the response is significantly overestimated resulting in $\varepsilon = 41.63$. In Fig. 8.9e we see the response of the apr-SEM divided by 2. The pattern correlation reads $cor = -0.92$ and overall the response is too pronounced with $\varepsilon = 4.90$. Similar results are found for the FDT-SEM (Fig. 8.9f, response divided by 2). Again the correlation is negative with $cor = -0.88$. Furthermore, the FDT-SEM also experiences a response in covariance that is too strong. In comparison to the apr-SEM, however, the maximum over Eastern Europe is missing, resulting in a relative error of $\varepsilon = 4.27$. Qualitatively similar results are found for the response in mean streamfunction (not shown).

For the different forcing locations we show a summarizing evaluation of the

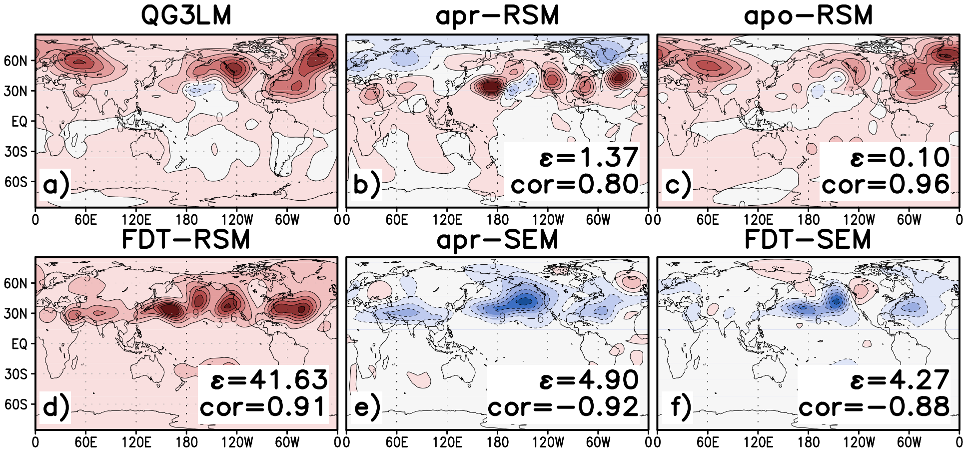

Figure 8.9: Response in covariance of streamfunction ($10^{13}\,\mathrm{m}^4\,\mathrm{s}^{-2}$) at 200 hPa resulting from a local anomalous forcing acting on all scales and located at $\lambda_c = 210°$. The response of (a) the QG3LM projected onto the slow variable (first 20 EOFs), (b) apr-RSM, (c) apo-RSM, (d) FDT-RSM, (e) apr-SEM, and (f) FDT-SEM. The color shading is the same for each panel, however, the response of the FDT-RSM (d) has been divided by 25 and the response of both SEMs (e) and (f) has been divided by 2, respectively.

models in Fig. 8.10. In particular, Figs. 8.10a and 8.10c display the relative amplitude error and correlation of the response in mean streamfunction, respectively, whereas Figs. 8.10b and 8.10d show the equivalent for the covariance of streamfunction. The RSM-FDT is unstable for all cases except $\lambda_c = 210°$. Furthermore, the FDT-SEM experiences the highest error for nearly all cases and both moments. Since this model is clearly not providing any useful results we adjusted the vertical axis in Figs. 8.10a and 8.10b to focus on the remaining models. For those we observe that both RSMs (apr-RSM and apo-RSM) outperform the apr-SEM for most forcing locations. Nevertheless, only in four cases ($\lambda_c \in \{90°, 120°, 300°, 330°\}$) the apr-RSM has a relative error in the response of both mean and covariance of streamfunction that is (slightly) less than 1. Unexpectedly, the response of the apo-RSM is not systematically better than that of the apr-RSM. For the response in mean streamfunction the apo-RSM outperforms all other models. However, for the response in covariance of streamfunction the situation is less clear. Even though there are cases in which the apo-RSM experiences a lower amplitude error, we also have forcing locations (e.g., $\lambda_c \leq 120°$) where the apr-RSM significantly

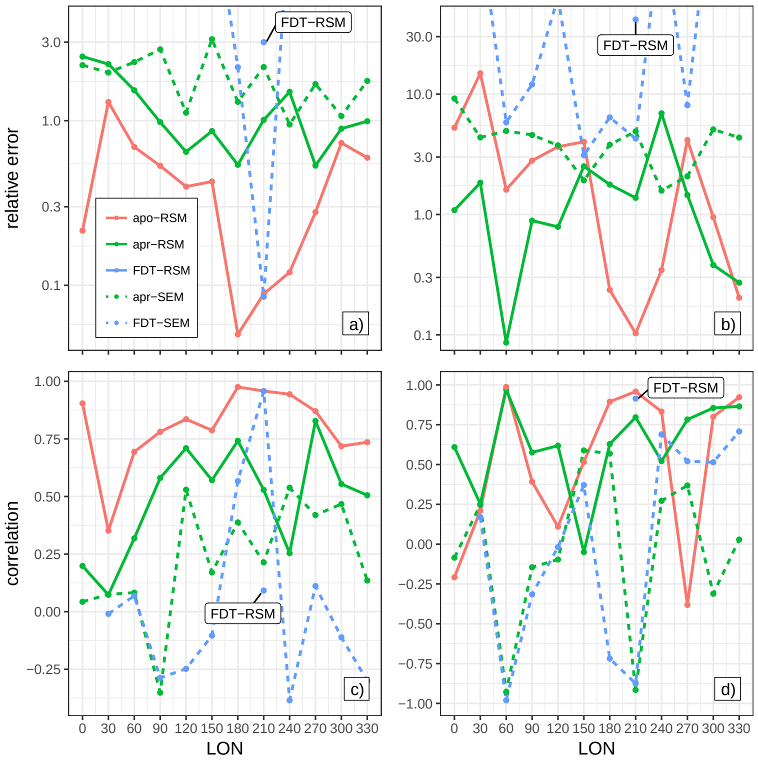

Figure 8.10: (Top) Relative error and (bottom) correlation of various RSMs and SEMs for $(S, F) = (20, 10)$ against longitude position of the external forcing acting on all scales. Shown is (a),(c) mean streamfunction; (b),(d) covariance of streamfunction. For the relative error the limits of the vertical axis have been set to 4 and 30, respectively. Thus some results of the FDT-SEM are cut out.

outperforms the retuned apo-RSM. In those cases, we see also a larger pattern correlation by the apr-RSM.

Anomaly Experiments: Forcing the Subgrid Scales

For the forcing acting only on the SGS we obtain an amplitude factor of $\alpha_{\text{SGS}} = 25$. Applying such a forcing located at $\lambda_c = 240°$ results in a response in covariance of streamfunction as shown in Fig. 8.11. First we note that by design the apr-SEM is independent of a forcing acting only on the SGS processes. Thus, Fig. 8.11e shows no response. The response of the QG3LM (Fig. 8.11a) is dominated by a maximum over Western Canada. The apr-RSM (Fig. 8.11b) is able to capture this maximum rather well, however, its amplitude is too weak. Furthermore, the

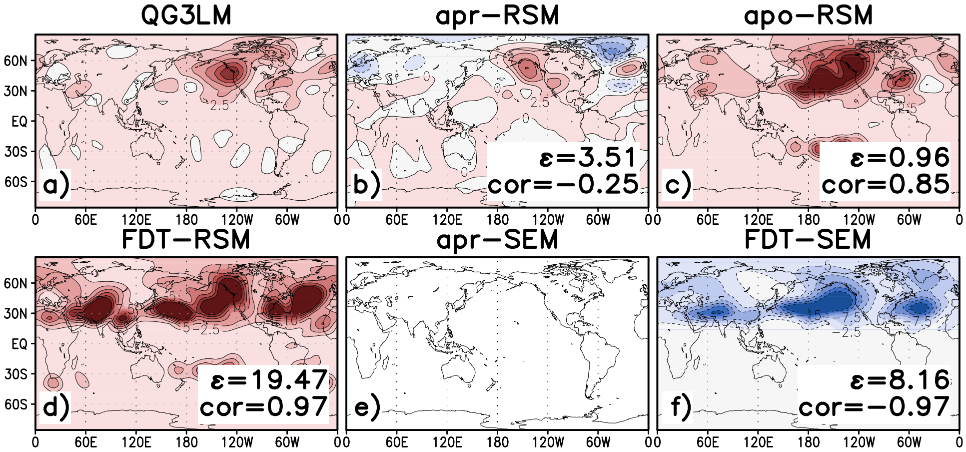

Figure 8.11: As in Fig. 8.9, but for a local anomalous forcing acting only on the SGS variable and located at $\lambda_c = 240°$. The color shading is the same for each panel, however, the response of the FDT-RSM (d) and of the FDT-SEM (f) has been divided by 5 and 2, respectively. Note that by design the apr-SEM (e) is independent of such a forcing and thus has no response.

apr-RSM suffers from a global minimum over the northern hemisphere similar to the case with forcing all scales (Fig. 8.9b). Therefore, the relative error reads $\varepsilon = 3.51$ and the correlation is given by $cor = -0.25$. Again, the apo-RSM (Fig. 8.11c) fairs better. It captures the pattern quite well, resulting in $cor = 0.85$. Yet, the apo-RSM overestimates the amplitude of the maximum over Western Canada and experiences an additional maximum in the southern hemisphere ($\varepsilon = 0.96$). In Fig. 8.11d we see the response of the FDT-RSM divided by 5. As for the previous forcing case we find that this model is able to reproduce the pattern ($cor = 0.97$) but significantly overestimates the strength of the response ($\varepsilon = 19.48$). Similar results are found for the FDT-SEM (Fig. 8.11f, response divided by 2) where the amplitude is also overestimated ($\varepsilon = 8.16$) and the response has an incorrect sign, resulting in $cor = -0.97$. Overall, we find a qualitatively similar behavior for the response in mean streamfunction (not shown).

Figure 8.12 shows the performance of all considered models against the forcing position. Similar to the case forcing all scales (Fig. 8.10) we find that most of the FDT-RSMs are unstable, except for $\lambda_c \in \{90°, 240°\}$. Additionally, the FDT-SEMs are also either unstable or experience a large relative amplitude error, which renders the model output useless. Thus, we again adjust the vertical axis in Figs.

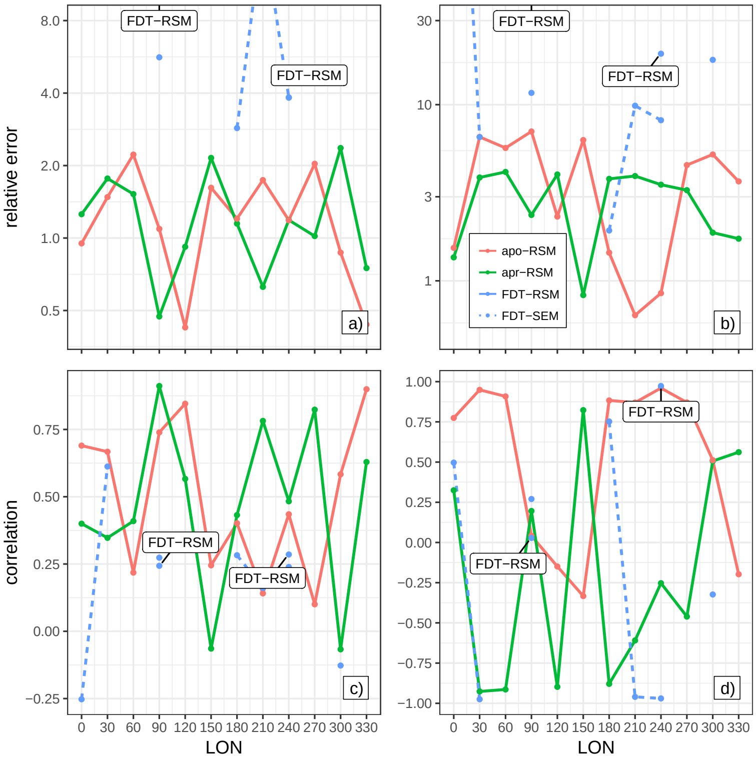

Figure 8.12: As in Fig. 8.10, but for a local anomalous forcing acting only on the SGS variable. Some relative errors of the FDT-SEM and of the FDT-RSM at $\lambda_c = 90°$ have been cut out since the limits of the vertical axis have been set to 8 and 30, respectively. Note that by design the apr-SEM is independent of a forcing acting on the SGS and thus has an infinite relative error and zero correlation (not shown).

8.12a and 8.12b to focus on the apr-RSM and apo-RSM. In general, we find a similar result as for the forcing with all scales, albeit the errors are overall larger. For roughly half of the forcing locations the apr-RSM outperforms (in terms of relative error and correlation) the apo-RSM and vice versa for both the response in mean and covariance of streamfunction, respectively.

8.3.4 Discussion

We find that, apart from the apr-SEM, both the forcing acting on all scales and the forcing acting only on the SGS processes produce the same behavior of the

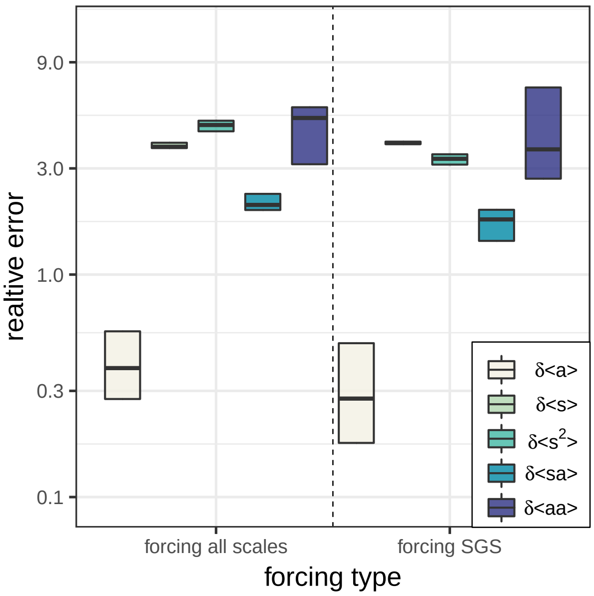

Figure 8.13: Boxplot of the relative error between the qG-FDT estimation and the true response of the moments for (left) the forcing acting on all scales, (right) the forcing acting on the SGS. The statistics for the boxplot come from the different forcing positions $\lambda_c \in \{0°, 30°, \ldots, 330°\}$. Both forcings have been multiplied by their respective amplitude factors (i.e., $\alpha_{\text{all}} = 15$ and $\alpha_{\text{SGS}} = 25$).

models. Thus, unless otherwise stated, we discuss in the following only the case with the forcing acting on all scales.

First we note that most of the FDT-RSM and a few of the FDT-SEM (Fig. 8.10 and Fig. 8.12) are unstable. This is caused by the incorrect closure update (or more precisely by the incorrect qG-FDT estimations of the perturbed statistics, see part I) by the qG-FDT. Figure 8.13 shows for both forcing types a boxplot of relative error between the qG-FDT estimations and the true response of the statistical moments. Clearly, the qG-FDT is unable to estimate all moments, except $\delta\langle\mathbf{a}\rangle$. The median of relative error of the latter is around $\varepsilon = 0.3$, whereas for the remaining moments the median of relative error is $\varepsilon > 2$. This indicates that the amplified forcings are too strong for the application of the qG-FDT.

Thus, we repeated the anomaly experiments with a forcing acting on all scales and an amplitude factor of $\alpha_{\text{all}} = 1$ (i.e., we are using the local anomalous forcing as presented in section 4.1.1 but projected onto the first 30 EOFs). Figure 8.14

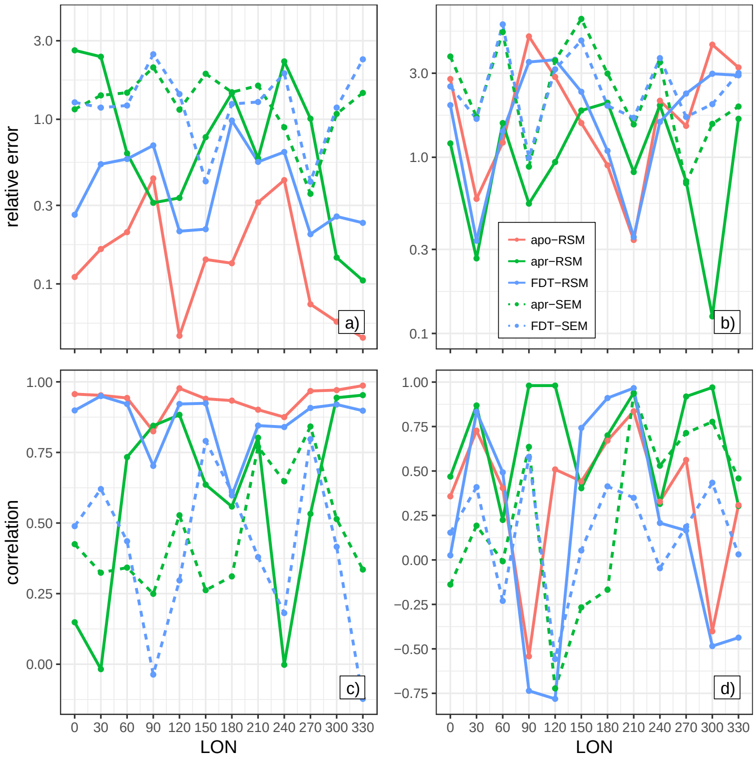

Figure 8.14: As in Fig. 8.10, but with a forcing amplitude of $\alpha_{\text{all}} = 1$.

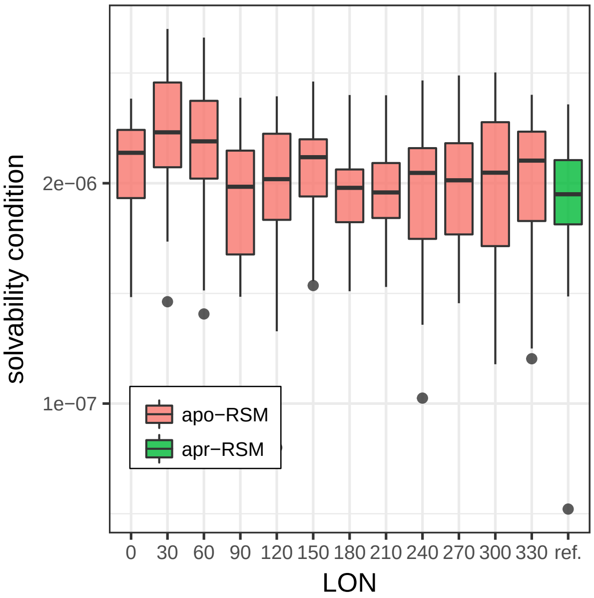

Figure 8.15: Boxplot of absolute value of the solvability condition for the apo-RSM with $(S, F) = (20, 10)$ against forcing position $\lambda_c \in \{0°, 30°, \ldots, 330°\}$. As reference the absolute value of the solvability condition of the apr-RSM is given.

shows the summarizing evaluation for all forcing locations. In general, we find that all models fair better in predicting the response of the weaker forcing (compare Fig. 8.14 to Fig. 8.10). Furthermore, both FDT-RSM and FDT-SEM are stable, and the former seems to be performing roughly similar to the apo-RSM, especially for the response in the covariance of the streamfunction. For the response in the mean streamfunction caused by the weak forcing (Fig. 8.14a) the apo-RSM seems to outperform the apr-RSM. Yet, for the response in covariance (Fig. 8.14b) the opposite is the case. Similar results were already found for the stronger forcing (Fig. 8.10).

To investigate this unexpected result, we first show the absolute values of the solvability condition [i.e., the amplitude of the gradient of the PDF in (6.28)] for the apo-RSM in the case of the forcing acting on all scales. In comparison, the reference of the unforced RSM is plotted as well (Fig. 8.15). We find that the apo-RSM has roughly the same solvability condition as the reference. Furthermore, there is no clear correlation between the magnitude of the solvability condition of the apo-RSM and the quality of its response. Thus, the variations in the solvability

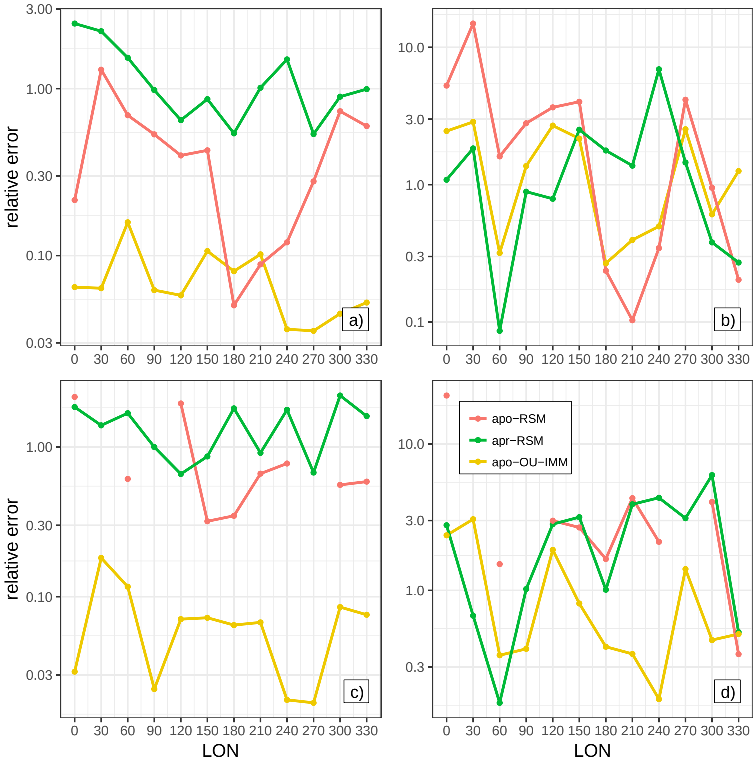

Figure 8.16: Relative error of the apr-RSM, apo-RSM, and apo-OU-IMM of the response of (a),(c) mean streamfunction and (b),(d) covariance of streamfunction resulting from a forcing acting on all scales. (a),(b) Evaluates the response for the forcing with an amplitude factor of $\alpha_{\text{all}} = 15$; (c),(d) for an amplitude factor of $\alpha_{\text{all}} = 30$.

condition cannot explain the observed performance of the apo-RSM.

It is possible that the forcing amplitude is still too weak, causing incorrect a posteriori parameters due to a small signal-to-noise ratio. Thus, we repeat the experiment with the forcing acting on all scales using an amplitude factor of $\alpha_{\text{all}} = 30$ (Fig. 8.16). Besides the apr-RSM and apo-RSM we also consider the apo-OU-IMM since this model contains the identical empirical parameters as the apo-RSM. In general, we find a decrease in performance for both RSMs for the forcing with $\alpha_{\text{all}} = 30$ (Figs. 8.16c and 8.16d) in comparison to $\alpha_{\text{all}} = 15$ (Figs. 8.16a and 8.16b). For the stronger forcing some apo-RSMs are unstable ($\lambda_c \in \{30°, 90°, 270°\}$) while for the rest the unexpected behavior (i.e., no systematic improvement over the apr-RSM) remains. The apo-OU-IMM outperforms the

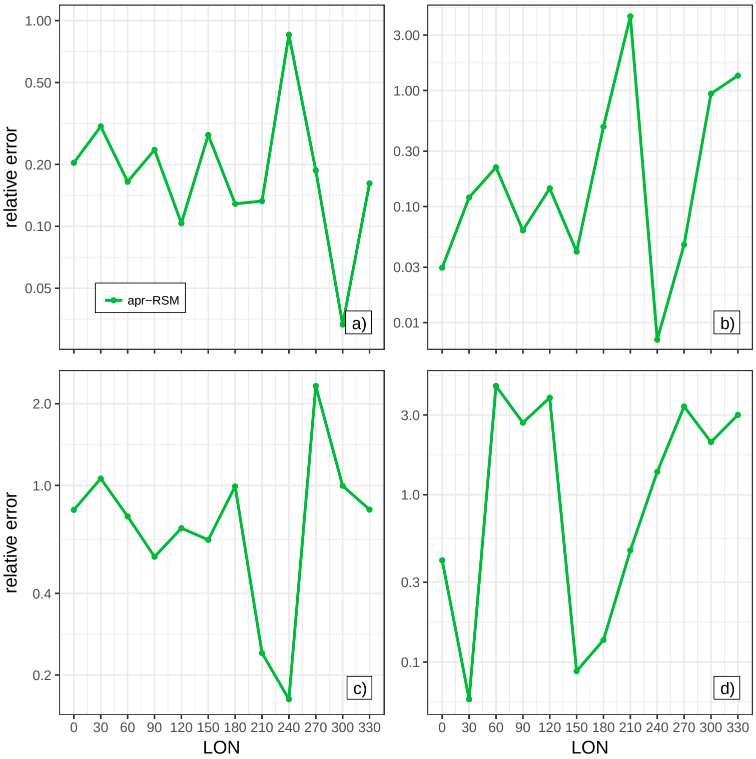

Figure 8.17: Relative error of the response of (a),(c) mean streamfunction and (b),(d) covariance of streamfunction of the apr-RSM with the apr-OU-IMM as reference. (a),(b) Shows the performance for a forcing acting on all sales, (c),(d) for the forcing acting only on the SGS. Both forcings are multiplied by their respective amplitude factors (i.e., $\alpha_{\text{all}} = 15$ and $\alpha_{\text{SGS}} = 25$).

RSMs for the response in mean streamfunction (on average $\varepsilon < 0.1$) and produces, at least for the case with $\alpha_{\text{all}} = 30$ (Fig. 8.16d), in approximately 70% of the forcing locations a useful response in the covariance of streamfunction ($\varepsilon < 0.8$). This indicates that there is no incorrect update of the empirical parameters.

Nevertheless, the empirical parameters seem to be the cause of the unexpected behavior of the apo-RSM. Thus, to disable the impact of the empirical parameters we use the OU-IMM instead of the QG3LM as a reference. In particular, we are comparing the forced apr-OU-IMM to the forced apr-RSM. Both models contain exactly the same empirical components (including the identical OU-process) allowing us to exclude any influence of tuning parameters. Figure 8.17 shows the summarizing evaluation for both forcing types (multiplied by their respective amplitude factors $\alpha_{\mathrm{all}} = 15$ and $\alpha_{\mathrm{SGS}} = 25$) and both statistical moments. In particular, Figs. 8.17a and 8.17b show the relative error of the response in the mean and covariance of streamfunction, respectively, for the forcing acting on all scales. Figures 8.17c and 8.17d show the counterpart for the forcing acting only on the SGS. Clearly, the apr-RSM is able to reproduce the response for both moments if the forcing acts on all scales. Overall, for the response in mean streamfunction the median of the relative error is $\varepsilon = 0.18$ and median of the correlation reads $cor = 0.92$. For the response in covariance of streamfunction the corresponding values are $\varepsilon = 0.13$ and $cor = 0.98$. In contrast, for the forcing acting only on the SGS the apr-RSM performs generally worse. In this case for the response in mean (variance) streamfunction the median of the relative error is given by $\varepsilon = 0.79$ ($\varepsilon = 1.72$) and the correlation reads $cor = 0.63$ ($cor = 0.41$). Yet, for the cases with a relative error less than 1 in the response of covariance the correlations are above $cor > 0.90$. Nevertheless, the performance of the apr-RSM in comparison to the apr-OU-IMM is significantly better than in comparison to the QG3LM (Fig. 8.10 and Fig. 8.12) for both forcing types.

Using this idealized setup, we can even go beyond a constant anomalous forcing by changing the amplitude of the linear coupling interaction coefficients:

$$\mathbf{L}'^{xy} \longrightarrow 1.65 \times \mathbf{L}'^{xy} \tag{8.10a}$$

$$\mathbf{L}'^{yx} \longrightarrow 0.65 \times \mathbf{L}'^{yx}\,, \tag{8.10b}$$

where the amplitude factors are arbitrarily chosen. Figure 8.18 shows the response in covariance of streamfunction of both the apr-OU-IMM (Figs. 8.18a and 8.18b) and apr-RSM (Figs. 8.18c and 8.18d) for the two forcings, respectively. The increase of the amplitude of $\mathbf{L}'^{xy}$ causes as response in covariance of streamfunction three maxima located over India, the Atlantic, and the Pacific Ocean in the apr-OU-IMM (Fig. 8.18a). The former two are significantly weaker than the latter. Furthermore, we observe another relatively weak maximum over the southern Pacific Ocean. The apr-RSM (Fig. 8.18c) reproduces the pattern of the response remarkably well, resulting in $cor = 0.996$. Also the strength of the response is well reproduced with a relative error of $\varepsilon = 0.03$. For the decrease in amplitude of $\mathbf{L}'^{yx}$ the response of covariance of streamfunction of the apr-OU-IMM (Fig. 8.18b)

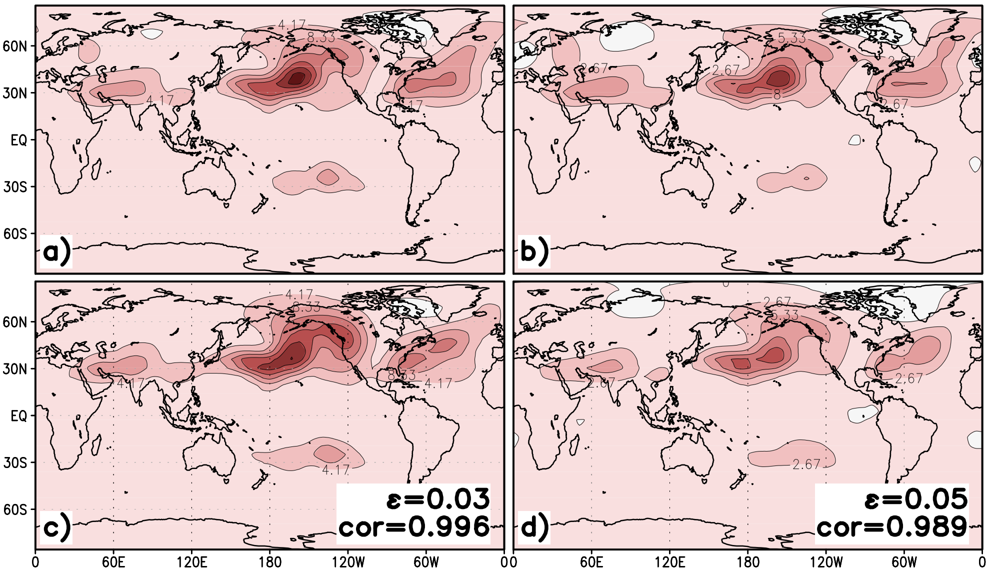

Figure 8.18: Response in covariance of streamfunction ($10^{13}\,\mathrm{m}^4\,\mathrm{s}^{-2}$) at 200 hPa of (a),(b) the apr-OU-IMM and (c),(d) the apr-RSM. (a),(c) Shows the response resulting from a change in $\mathbf{L}'^{xy}$ (8.10a); (b),(d) resulting from a change in $\mathbf{L}'^{yx}$ (8.10b). The relative amplitude error and the correlation have been calculated with respect to the apr-OU-IMM.

has nearly the same pattern as for the change in the linear coupling of the slow equation. Yet, overall the strength of the response is roughly 35% weaker. Again the apr-RSM (Fig. 8.18d) is able to reproduce the response pattern quite well ($cor = 0.989$). However, the response of the apr-RSM is slightly underestimating the reference. Still, the relative error is only $\varepsilon = 0.05$. This shows that in principle the RSM is able to adapt even to anomalies in the linear dynamics, at least if the impact of the empirical parameters is disabled.

The results with the apr-OU-IMM as reference show that the RSM is able to respond correctly to external forcings if the impact of the tuning parameters is disabled. The a posteriori tuning parameters are correct, yet the apo-RSM is unable to produce a correct response in the covariance of the streamfunction. On the other hand, the response in the mean streamfunction is relatively well reproduced. In part I we found qualitatively similar behavior of the apo-SEM for cases with ≤ 200 EOFs. This suggests that a RSM with larger (S, F) might perform better as well.

8.4 Reduced Stochastic Model Including the Nonlinear Self-Interaction of the Fast Variable

Usually when applying the SMR, the nonlinear self-interaction term of the fast variable is replaced by an OU-process, since this term is the dominating term in the system. In return, this OU-process is then used to derive the RSM. However, Fig. 8.5 shows that the nonlinear self-interaction of the fast variable [at least for the truncations of (S, F) considered in this thesis] is not the dominating term of the IMM. Therefore, we exploit the fact that we do not apply the SMR directly to the QG3LM but to a subspace and include $\boldsymbol{\mathsf{N}}^{yyy}$ explicitly in the RSM, by constructing a stochastic IMM. This results in a modification of the RSM closure as described below.

8.4.1 Analytic Results

Stochastic Intermediate Model

For the stochastic IMM (IMM$_{\mathrm{stoch}}$) we replace the linear deterministic closure of $\mathbf{z}$ in the fast variable (7.5b) by an OU-process, i.e.

$$\mathbf{p}^{y}(\mathbf{x},\mathbf{y}) = \mathbf{r}^{y} + \mathbf{l}^{yx}\mathbf{x} + \mathbf{l}^{yy}\mathbf{y} + \boldsymbol{\sigma}^{y}\dot{\mathbf{W}} + \boldsymbol{\epsilon}^{y}\,. \tag{8.11}$$

This approach is analogous to the construction of the SEM$_{\mathrm{stoch}}$. Similar to the OU-IMM it is crucial that we use the tendency of the QG3LM to fit the OU-process (see section 8.2.2). The IMM$_{\mathrm{stoch}}$ reads then

$$\begin{aligned}
\mathrm{d}\mathbf{x} = {} & [(\mathbf{F}^{x} + \mathbf{r}^{x}) + (\boldsymbol{\mathsf{L}}^{xx} + \mathbf{l}^{xx})\mathbf{x} + \boldsymbol{\mathsf{N}}^{xxx}\mathbf{x}\mathbf{x} \\
& +(\boldsymbol{\mathsf{L}}^{xy} + \mathbf{l}^{xy})\mathbf{y} + \boldsymbol{\mathsf{N}}^{xxy}\mathbf{x}\mathbf{y} + \boldsymbol{\mathsf{N}}^{xyx}\mathbf{y}\mathbf{x} + \boldsymbol{\mathsf{N}}^{xyy}\mathbf{y}\mathbf{y}]\,\mathrm{d}t & \quad (8.12\mathrm{a}) \\
\mathrm{d}\mathbf{y} = {} & [(\mathbf{F}^{y} + \mathbf{r}^{y}) + (\boldsymbol{\mathsf{L}}^{yx} + \mathbf{l}^{yx})\mathbf{x} + \boldsymbol{\mathsf{N}}^{yxx}\mathbf{x}\mathbf{x} \\
& +(\boldsymbol{\mathsf{L}}^{yy} + \mathbf{l}^{yy})\mathbf{y} + \boldsymbol{\mathsf{N}}^{yxy}\mathbf{x}\mathbf{y} + \boldsymbol{\mathsf{N}}^{yyx}\mathbf{y}\mathbf{x} + \boldsymbol{\mathsf{N}}^{yyy}\mathbf{y}\mathbf{y}]\,\mathrm{d}t + \boldsymbol{\sigma}^{y}\mathrm{d}\mathbf{W}\,. & \quad (8.12\mathrm{b})
\end{aligned}$$

Since we used the tendency of the QG3LM, the OU-process is dominating (8.12b). Thus, in contrast to the classical SMR (chapter 6) we can keep the nonlinear self-interaction term of the fast variable in the IMM$_{\mathrm{stoch}}$.

Modification of the Standard Reduced Stochastic Model

The nonlinear self-interaction of the fast variable in the $\mathrm{IMM}_{\mathrm{stoch}}$ (8.12) is relatively unimportant (see Fig. 8.5). Therefore, we assume that $\mathbf{N}^{yyy}\mathbf{y}\mathbf{y}$ scales with ε^{-1} while using the same scaling as in the OU-IMM (7.15) for the remaining terms. Hence, we have

$$g_1(\mathbf{x},\mathbf{y}) \longrightarrow g_1(\mathbf{x},\mathbf{y}) + \mathbf{N}^{yyy}\mathbf{y}\mathbf{y}\,, \tag{8.13}$$

which leads to

$$\int_0^\infty \mathbb{E}\left[\{\mathbf{N}^{yyy}\mathbf{y}\mathbf{y}\cdot\mathbf{D}^{-1}\mathbf{y}\}f_1(\mathbf{x},\mathbf{y}[\tau])\right]_{\mathrm{OU}}\,\mathrm{d}\tau\,. \tag{8.14}$$

Consequently, we obtain the original RSM (6.33) with the following modifications

$$\boldsymbol{\mathcal{F}}_i \longrightarrow \boldsymbol{\mathcal{F}}_i + \mathbf{N}^{yyy}_{klm}\mathbf{L}^{xy}_{ij}\mathbf{D}_{lm}\mathbf{K}_{jk} \tag{8.15a}$$

$$\boldsymbol{\mathcal{L}}_{ij} \longrightarrow \boldsymbol{\mathcal{L}}_{ij} + \mathbf{N}^{yyy}_{lmn}(\mathbf{N}^{xxy}_{ijk} + \mathbf{N}^{xyx}_{ikj})\mathbf{D}_{mn}\mathbf{K}_{kl}\,. \tag{8.15b}$$

We call the resulting model the $\mathbf{N}^{yyy}$-RSM.

8.4.2 Setup

We use the same setup as for the unforced RSM, however, we restrict the investigation of the $\mathbf{N}^{yyy}$-RSM on $S \in \{10, 20\}$.

8.4.3 Numerical Experiments

Figure 8.19 shows the relative error between the $\mathbf{N}^{yyy}$-RSM and the QG3LM in comparison to the performance of the classical RSM for both the mean streamfunction (Fig. 8.19a and 8.19b) and the covariance of streamfunction (Fig. 8.19c and 8.19d). For the mean streamfunction the $\mathbf{N}^{yyy}$-RSM outperforms the RSM for $S = 10$ and $F \in \{5, 10\}$ as well as $S = 20$ and $F \in \{20, 30\}$. In contrast, for the covariance of streamfunction we find only for $S = 20$ and $F \in \{20, 30\}$ a slightly

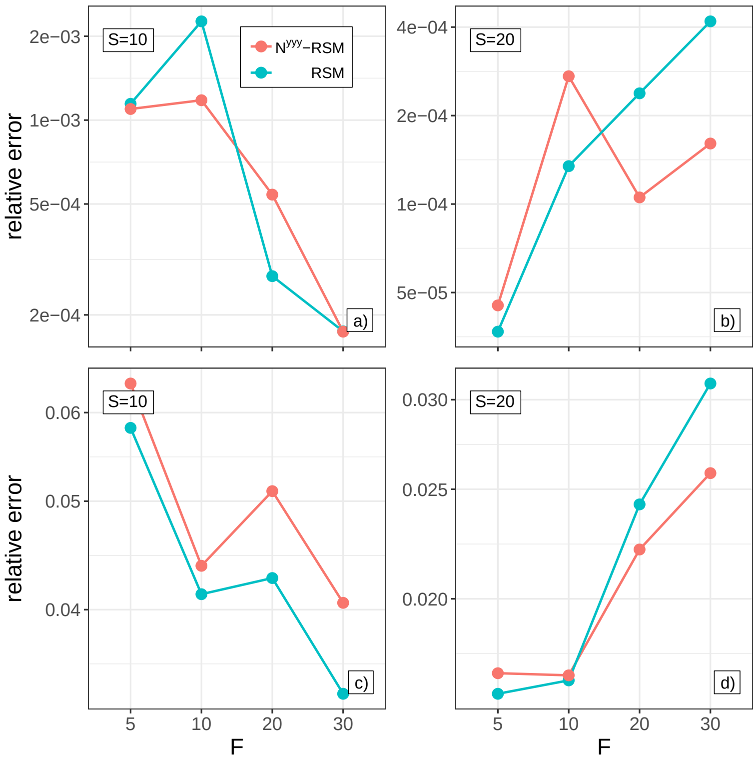

Figure 8.19: As in Fig. 8.3, but for the $\mathbf{N}^{yyy}$-RSM and RSM for various combinations of $S \in \{10, 20\}$ and $F \in \{5, 10, 20, 30\}$. (a),(b) Relative error of mean streamfunction; (c),(d) corresponding relative error in covariance of streamfunction.

better performance of the $\mathbf{N}^{yyy}$-RSM. For the remaining truncations the explicit consideration of the nonlinear self-interaction of the fast variable yields no benefit. Yet, overall the differences between the classical RSM and the $\mathbf{N}^{yyy}$-RSM are quite small and thus insignificant.

8.4.4 Discussion

For the unforced case we find that the $\mathbf{N}^{yyy}$-RSM performs equally well compared to the RSM. This shows that it is possible to generalize the SMR, allowing for a quadratic nonlinearity in the fast variable. Even for higher truncations of S (not shown) we find that the $\mathbf{N}^{yyy}$-RSM is virtually identical to the RSM. Yet, as discussed in section 8.2.2 with increasing F we shift the importance of the remaining unparameterized part of the hidden variable to $\mathbf{N}^{yyy}$. Therefore, we would expect that the $\mathbf{N}^{yyy}$-RSM eventually would fail to reproduce the statistics of the QG3LM for large enough F.

Since the considered cases here we find no added value by considering the nonlinear self-interaction explicitly in the SMR, we pass on an investigation of a forced $\mathbf{N}^{yyy}$-RSM.

Chapter 9

Conclusion

In this thesis we investigated the issue of tuning parameters under different boundary conditions (e.g., a different climate). In part I we addressed whether it is possible to update already existing tuning parameters in the models according to the acting anomalous forcing, thus making them climate dependent. If the tuning is done objectively (i.e., the empirical parameters depend on the statistics of the data), then we might be able to utilize the Fluctuation-Dissipation theorem (FDT) as proposed by Achatz et al. (2013). Complementary to that we constructed a reduced stochastic model (RSM) using the stochastic mode reduction (SMR) in part II. This method is constrained by first principle and hence requires only minimal tuning. However, for the application of the SMR we require a scale separation in the system. In addition, we combined both methods to see whether applying the FDT to the remaining empirical components of the RSM leads to further improvement.

We tested the two approaches on the well-established quasigeostrophic three-layer model (QG3LM) of Marshall and Molteni (1993). Furthermore, we perturbed the model by a local anomalous forcing given by a localized heat source that simulates the effect of a sea-surface temperature anomaly (Branstator and Haupt 1998; Achatz and Branstator 1999). Additionally, we used one of the first five empirical orthogonal functions (EOFs), respectively, and constructed a global dynamical forcing (Pieroth et al. 2018).

In part I we considered a semi-empirical model (SEM) based on the leading EOFs of the QG3LM and supplemented by a purely data-driven subgrid-scale (SGS) parameterization. As a closure we considered either a simple linear function ($\mathrm{SEM}_{\mathrm{det}}$) or an Ornstein-Uhlenbeck process (OU-process; $\mathrm{SEM}_{\mathrm{stoch}}$). Both parameterizations were objectively tuned by minimizing the residual error and applying the Maximum-Likelihood method, respectively. We showed that both SEMs are qualitatively and quantitatively able to reproduce the statistics of the QG3LM. However, they experienced an incorrect response in the presence of the external forcings. This issue is well known for reduced models containing data-driven parameterizations (Achatz and Branstator 1999; Achatz and Opsteegh 2003b) and renders these types of models useless for climate projections. Yet, this is a fundamental problem in climate modeling, which is not limited to low-order models but also affects state-of-the-art global circulation models (GCMs) and climate models. Usually such models do not contain purely data-driven SGS parameterizations but closures based on physics. Nevertheless, even physically based SGS parameterizations, such as convection, radiation, or gravity wave schemes, contain to some degree empirical components (e.g., entrainment of convective cells, aerosol distribution, or launch level of gravity waves). While one could hope that, in comparison to purely data-driven parameterizations, the physical basis would make such closures more robust against an external forcing, we find indications in the literature that this is not the case (e.g., Schirber et al. 2015; Rockel and Geyer 2008).

To tackle this issue, we followed the approach of Achatz et al. (2013) and used the FDT to estimate updates of the tuning parameters. The FDT provides estimations on the change of the statistics of a system that is perturbed by an external forcing. If the empirical parameters depend in a mathematically rigorous way on the statistics, the FDT estimations might be used to introduce a climate dependence in the tuning parameters. In particular, we used the simplest form of the FDT: the quasi-Gaussian FDT (qG-FDT). In this approximation the response operator of the qG-FDT reduces to a simple integral over lag-correlation functions. Achatz et al. (2013) applied this ansatz to a barotropic flow on the sphere. While they found a systematic improvement in the models with the qG-FDT-treated closure only a part of the tuning parameters could be updated. The qG-FDT estimations of the second moments were not sufficiently accurate to provide useful updates for the remaining tuning parameters. Achatz et al. (2013) potentially suffered from a lack of high-frequency variability, which limits the applicability of the FDT. In contrast, the QG3LM, which includes baroclinic instability, is better suited for the FDT.

For both the local and global anomalous forcings we found that the qG-FDT estimations of the response of the first moments were remarkably accurate. However, the estimations for the second moments experienced a systematically higher error. This is consistent with the results of Gritsun et al. (2008) and has been proven, for a transient response, by Majda et al. (2005, p. 68) as a general property of the FDT. In contrast to Achatz et al. (2013), however, the estimations of the second moments were sufficiently accurate to provide useful updates for all empirical closure parameters in the SEM. We could show that the FDT-SEM (i.e., where the tuning parameters have been updated with the FDT) systematically outperformed the apr-SEM (i.e., the SEM with an unmodified closure). Furthermore, we found that the combination of the linear FDT estimation with the nonlinear SEM yields a skillful response even if the response is nonlinear. Therefore, this approach is superior in comparison to the direct application of the FDT as proposed by Leith (1975, 1978), at least if sufficiently large EOF truncations are used. In general, we required SEMs with at least 200 EOFs to obtain useful results for the response in covariance of streamfunction (i.e., relative errors below 100%). We could exclude the signal-to-noise ratio as a reason for this behavior. It is possible that the SEMs need to describe a certain amount of explained variance of the QG3LM, for a correct representation of the response in covariance.

In addition to the qG-FDT, we applied the more sophisticated blended Short-Time/qG-FDT (ST/qG-FDT; Abramov and Majda 2008) onto selected cases. The ST/qG-FDT drops to some degree the assumption of Gaussianity resulting in a generally superior response operator (Abramov and Majda 2008, 2009), however, the increased accuracy is at the expense of computational effort. At least for the cases considered in this thesis, no notable benefit was gained by the ST/qG-FDT. Instead, our results indicated that the comparatively simple qG-FDT suffices to compute useful updates for the empirical parameters.

All in all, we could show that, under appropriate conditions, the FDT enables us to update tuning parameters of SGS closures in the presence of an external forcing. However, it remains to be seen if this ansatz can be used to update tuning parameters of standard physical SGS parameterizations (e.g., turbulence, gravity waves, clouds, or convection). Furthermore, it might be interesting to see whether the FDT is able to deal with a realistic external forcing. Additionally, the applicability of this approach to more complex models (e.g., GCMs) with unbalanced motion such as gravity waves should be considered.

Yet, the FDT ansatz suffers also from disadvantages. The response operator of the FDT itself is data dependent. Therefore, we require sufficient data to construct a useful operator. In particular, we need to sufficiently sample the statistical steady state of the model. Furthermore, it is unlikely that the FDT predicts correctly a drastic change in the climate (i.e., tipping points) unless the data used for the computation of the response operator included a statistical significant sample of such a regime transition. Moreover, for the FDT to work the forcing must not project onto the stable direction of the attractor (Gritsun and Lucarini 2017). However, it is not guaranteed that the driving force of the climate change projects only in the unstable direction. Lastly, the FDT is a linear theory that breaks down if the forcing is too strong.

Given the disadvantages of the FDT ansatz it can only be seen as a temporary solution. Instead, climate models and GCMs should use SGS parameterizations based on first principles. Thus, we investigated in part II the SMR as an approach to construct an SGS closure constrained by first principles (Franzke 2013). The SMR requires that the system can be separated into different characteristic scales (e.g., fast and slow modes). Furthermore, it assumes that the fastest components of the system can be replaced by a Gaussian process. In this thesis we fitted an OU-process explicitly, although, in general this Gaussian process does not need to be specified (Franzke et al. 2005). In the limit of an infinite scale separation the explicit evolution of the fast modes is no longer important, and their effect on the slow variable can be treated by a suitable noise. The SMR provides a mathematically rigorous and analytic derivation of this stochastic parameterization, depending explicitly on the interaction coefficients (i.e., the model equation).

In contrast to the classical theory, we applied the SMR not directly to the QG3LM, to avoid a minor conceptual energy conservation problem. Instead, we split the EOF space into three variables: the slow variable, the fast mode, and the hidden variable. The latter was eliminated and described by a deterministic data-driven SGS parameterization (the same as used in the $\mathrm{SEM}_{\mathrm{det}}$). Next we fit an OU-process to replace the nonlinear self-interaction of the fast variable and the remaining unparameterized hidden modes. This way the energy fluctuations of resolved modes, introduced by the OU-process, may be seen as a coupling to the energy reservoir of the unparameterized hidden variable. For the partition of the EOF space we defined the first few EOFs as the slow variable, followed by the fast modes, and declared the remaining EOFs as the hidden variable, since the explained variance roughly coincides with the autocorrelation time scale (Franzke and Majda 2006).

We successfully constructed the RSM for the OU intermediate model (OU-IMM; i.e., the QG3LM without the hidden variable but with the empirical OU-process) using the SMR. Independent of the dimension of the fast and slow variable, respectively, the RSM was both quantitatively and qualitatively similar to the SEM. Franzke and Majda (2006) applied the seamless SMR (Franzke et al. 2005) to the same model in northern hemispheric mode. However, their RSM experienced a climatic drift and thus performed significantly worse than the RSM presented in this thesis. We identified the additional empirical closure in the slow variable, caused by the elimination of the hidden mode, as the reason for the improved performance of our RSM. Furthermore, the hidden variable allowed us to go beyond the classical SMR and keep the fastest term explicitly in the RSM. However, the resulting modified RSM showed no improvement over the standard RSM.

For the investigation of the RSMs' robustness with respect to an external forcing we perturbed the model with the localized heat source. In particular, we considered the heat source acting either on all scales (on both the slow and fast variable) or only on the SGS (i.e., the fast variable), respectively. In contrast to part I, we deliberately increased the forcing strength until the response was significantly stronger than the bias of the unforced RSM. For the anomaly experiments we considered five different models: the apr-RSM (no change in tuning parameters but an adjusted closure as given by the SMR), the apo-RSM (as the apr-RSM but with retuned empirical closure and OU-process, respectively), the FDT-RSM (as the apo-RSM but with updates estimated by the qG-FDT), the apr-SEM (no change in parameterization), and the FDT-SEM (closure updated with the qG-FDT).

In general, all models performed better for a forcing acting on all scales compared to the case with the forcing acting only on the SGS. Still, for both forcing types we found that the RSMs systematically outperformed the SEMs. For the response in covariance of streamfunction, however, the relative errors were above 100%. Furthermore, we found no clear improvement of the apo-RSM in comparison to the apr-RSM. While the correlation was mostly higher for the apo-RSM, the amplitude of the response in covariance of streamfunction was not always improved. In contrast, for the response in mean streamfunction the apo-RSM provided useful results and systematically outperformed the apr-RSM, although, only for the forcing acting on all scales. In addition, the strong external forcings denied the application of the qG-FDT. Both the FDT-RSM and the FDT-SEM were either unstable or produced an unrealistic response with significant amplitude errors. For the original strength of the forcing (i.e., as used in part I) the FDT-RSM provided roughly the same results as the apo-RSM. Nevertheless, even for the weaker external forcings the apo-RSM did not perform systematically better than the apr-RSM, and both RSMs experienced relative errors $\varepsilon > 1$ for the response in covariance of the streamfunction.

The unexpected low performance of the apo-RSM was most likely caused by the empirical parameters introduced when eliminating the hidden variable. We could exclude incorrect a posteriori parameters caused by a small signal-to-noise ratio. It is possible that the considered apo-RSM, based on a twenty-dimensional slow variable and a ten-dimensional fast variable, is simply too low dimensional in order to resolve a correct response in the covariance of the streamfunction. The qualitatively similar results of the apo-SEM in part I indicate that also for the apo-RSM we might require at least 200 EOFs to resolve this response correctly.

Nevertheless, we could show that in general the RSM is able to produce a correct response if we exclude the impact of the empirical parameters. For this we conducted anomaly experiments with the apr-OU-IMM as the reference instead of the QG3LM. We found that the RSM reproduced the response in mean streamfunction and covariance of streamfunction, of both the strong and weak external forcings, remarkably well. Furthermore, we could show that the RSM is able to adapt even to anomalies in the linear dynamics.

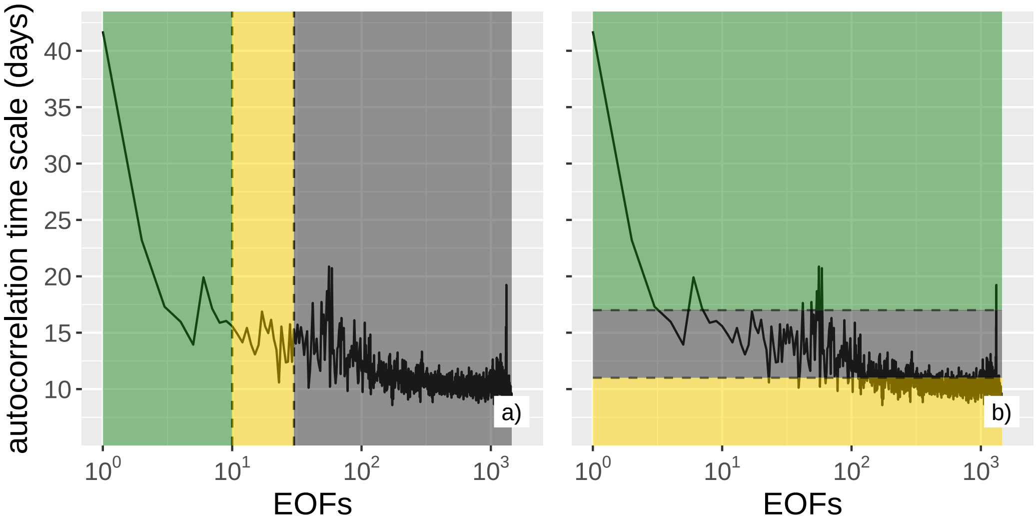

Figure 9.1: Schematic of EOF space partitions. (a) Traditional partition with respect to the explained variance, (b) alternative partition with respect to the autocorrelation time scale. The colors indicate the slow variable (green), the fast variable (yellow), and the hidden variable (grey).

These results encourage us to investigate the response of RSMs with larger (S, F) to study if the model benefits from an increased dimension. In this context, it is interesting to see whether we need to increase the dimension of the resolved variable or if an increase of the dimension of the fast variable is sufficient. Taking this to the extreme, we should construct a RSM based on the full QG3LM (i.e., without the hidden variable). This would allow us to confirm that the hidden variable (or rather the additional empirical closure used to describe its effect on the remaining variables) is the reason that the RSM presented in this thesis significantly outperforms the results of Franzke and Majda (2006). Furthermore, the hidden variable offers an alternative partition of the EOF space. Instead of splitting the EOF space with respect to the explained variance (Franzke et al. 2005; Franzke and Majda 2006), we could reorder the EOFs with respect to the autocorrelation time scale, as shown schematically in Fig. 9.1, and investigate the effect of this alternative partition on the performance of the RSM.

Appendix A

Fluctuation-Dissipation Theorem

A.1 Cooper-Haynes Algorithm

The FDT operator is based on the integral of the cross-covariance matrix

$$\int\limits_0^\infty \mathsf{C}_h(\tau)\mathrm{d}\tau = \int\limits_0^\infty h(\tau)\mathbf{x}'^{\mathrm{T}}(0)\mathrm{d}\tau \,, \tag{A.1}$$

where h is an arbitrary variable whose response should be estimated. For practical purposes the infinite integral is approximated by a finite time lag T_{max}:

$$\int\limits_0^\infty \mathsf{C}_h(\tau)\mathrm{d}\tau \approx \int\limits_0^{T_{\mathrm{max}}} \mathsf{C}_h(\tau)\mathrm{d}\tau \,. \tag{A.2}$$

Lutsko et al. (2015) presents an efficient algorithm, the so-called Cooper-Haynes Algorithm (CHA), which solves (A.2). In this chapter the CHA is derived for Simpson's rule.

For a time series of length n the cross-covariance matrix in (A.2) is given by

$$\mathsf{C}_h(\tau) = \frac{1}{n-l-1}\sum_{k=1}^{n-l} h_{k+l}\mathbf{x}_k'^{\mathrm{T}} \,, \tag{A.3}$$

where l is the number of data points of time lag τ and r denotes the number of points of the maximum time lag $T_{\max}$ (i.e., $r = T_{\max}/\Delta\tau$, where $\Delta\tau$ is the integration time step). Furthermore, we assume, without loss of generality, that r is even[1]. Then the integral (A.2) can be written as

$$
\begin{aligned}
&\int\limits_0^{T_{\max}} \mathsf{C}_h(\tau)\mathrm{d}\tau \approx \\
&\quad \frac{\Delta\tau}{3}\left[\frac{1}{n-1}\sum_{k=1}^{n} h_k \mathbf{x}_k'^{\mathrm{T}} + \frac{1}{n-r-1}\sum_{k=1}^{n-r} h_{k+r}\mathbf{x}_k'^{\mathrm{T}} + \frac{2}{n-2}\sum_{k=1}^{n-1} f(k+1)h_{k+1}\mathbf{x}_k'^{\mathrm{T}}\right. \\
&\qquad + \frac{2}{n-4}\sum_{k=1}^{n-3} f(k+3)h_{k+3}\mathbf{x}_k'^{\mathrm{T}} + \ldots + \frac{2}{n-r}\sum_{k=1}^{n-(r-1)} f(k+r-1)h_{k+r-1}\mathbf{x}_k'^{\mathrm{T}} \\
&\qquad + \frac{2}{n-3}\sum_{k=1}^{n-2} f(k+2)h_{k+2}\mathbf{x}_k'^{\mathrm{T}} + \frac{2}{n-5}\sum_{k=1}^{n-4} f(k+4)h_{k+4}\mathbf{x}_k'^{\mathrm{T}} \\
&\qquad \left. + \ldots + \frac{2}{n-r+1}\sum_{k=1}^{n-(r-2)} f(k+r-2)h_{k+r-2}\mathbf{x}_k'^{\mathrm{T}}\right], \qquad \text{(A.4)}
\end{aligned}
$$

where the function $f : \mathbb{N} \to \mathbb{R}$ is defined by

$$
f(k) = \begin{cases} 2, & k \text{ even} \\ 1, & k \text{ odd}\,. \end{cases} \qquad \text{(A.5)}
$$

Thus, (A.4) can be reduced to

$$
\begin{aligned}
\int\limits_0^{\infty} \mathsf{C}_h(\tau)\mathrm{d}\tau \approx \frac{\Delta\tau}{3}&\left\{\frac{1}{n-1}\sum_{k=1}^{n} h_k \mathbf{x}_k'^{\mathrm{T}} - \frac{1}{n-r-1}\sum_{k=1}^{n-r} h_{k+r}\mathbf{x}_k'^{\mathrm{T}}\right. \\
&+ \sum_{l=1}^{r/2}\left[\frac{2}{n-2l}\sum_{k=1}^{n-2l+1} f(k+2l-1)h_{k+2l-1}\mathbf{x}_k'^{\mathrm{T}}\right. \\
&\left.\left. + \frac{2}{n-2l-1}\sum_{k=1}^{n-2l} f(k+2l)h_{k+2l}\mathbf{x}_k'^{\mathrm{T}}\right]\right\}. \qquad \text{(A.6)}
\end{aligned}
$$

If we additionally assume that the time lag is small compared to the total length

---

[1] Should this be not the case, we simply neglect the first data point of the time series.

of the time series (i.e., $r \ll n$), the last term can be further simplified to

$$\sum_{l=1}^{r/2}\left[\frac{2}{n-2l}\sum_{k=1}^{n-2l+1} f(k+2l-1)h_{k+2l-1}\mathbf{x}_k'^{\mathrm{T}} + \frac{2}{n-2l-1}\sum_{k=1}^{n-2l} f(k+2l)h_{k+2l}\mathbf{x}_k'^{\mathrm{T}}\right]$$
$$\approx \frac{2\Delta\tau}{3(n-r-1)}\sum_{k=1}^{n-r}\sum_{l=1}^{r/2}\left[f(k+2l-1)h_{k+2l-1}+f(k+2l)h_{k+2l}\right]\mathbf{x}_k'^{\mathrm{T}}\,. \tag{A.7}$$

Hence, the CHA for Simpson's rule reads

$$\int_0^{T_{\max}} \mathsf{C}_h(\tau)\mathrm{d}\tau = \frac{\Delta\tau}{3}\left\{\frac{1}{n-1}\sum_{k=1}^{n} h_k\mathbf{x}_k'^{\mathrm{T}} - \frac{1}{n-r-1}\sum_{k=1}^{n-r} h_{k+r}\mathbf{x}_k'^{\mathrm{T}}\right.$$
$$\left.\frac{2}{n-r-1}\sum_{k=1}^{n-r}\sum_{l=1}^{r/2}\left[f(k+2l-1)h_{k+2l-1}+f(k+2l)h_{k+2l}\right]\mathbf{x}_k'^{\mathrm{T}}\right\}\,. \tag{A.8}$$

The sum over k in the last term of (A.8) can be obtained from the previous partial sum by a single addition and subtraction operation, respectively. Thus, for $\mathsf{C}_h \in \mathbb{R}^{N\times N}$ the CHA requires only $N^2 n$ operations (Lutsko et al. 2015).

A.2 Short-Time Fluctuation-Dissipation Theorem

In the following we proof that the nonlocal derivative $\nabla_{\mathbf{x}} h(\mathbf{X}[\tau,\mathbf{x}])$ can be calculated by the tangent linear model. The following calculation is based on Baiesi and Maes (2013).

Proof. Let us consider a discrete time evolution of the system (2.1)

$$\mathbf{x}_{n+1} = \mathbf{x}_n + \Delta t\mathbf{G}(\mathbf{x}_n) \equiv \mathbb{G}_n(\mathbf{x}_n)\,, \tag{A.9}$$

where $n \in \mathbb{N}$ denotes the time index and Δt is the time step of the discrete evolution (i.e., in the limit $\Delta t \to 0$ the original system is recovered). Then we have in the discrete setting

$$\nabla_{\mathbf{x}_0} h(\mathbf{x}[\tau]) = \nabla_{\mathbf{x}_0} h(\mathbf{x}_{n_\tau})\,, \tag{A.10}$$

where n_τ indicates the time steps needed to reach time τ and, without loss of generality, we set $t = 0$ and let $\mathbf{x}(0) = \mathbf{x}_0$. By chain rule we get

$$\nabla_{\mathbf{x}_0} h(\mathbf{x}_{n_\tau}) = \nabla h(\mathbf{x}_{n_\tau}) \nabla_{\mathbf{x}_0} \mathbf{x}_{n_\tau} \,. \tag{A.11}$$

Applying (A.9) and the chain rule recursively yields

$$\begin{aligned}
\nabla_{\mathbf{x}_0} h(\mathbf{x}_{n_\tau}) &= \nabla h(\mathbf{x}_{n_\tau}) \nabla_{\mathbf{x}_0} \mathbb{G}_{n_\tau-1}(\mathbf{x}_{n_\tau-1}) && \text{(A.12)}\\
&= \nabla h(\mathbf{x}_{n_\tau}) \nabla \mathbb{G}_{n_\tau-1}(\mathbf{x}_{n_\tau-1}) \nabla_{\mathbf{x}_0} \mathbb{G}_{n_\tau-2}(\mathbf{x}_{n_\tau-2}) && \text{(A.13)}\\
&= \nabla h(\mathbf{x}_{n_\tau}) \nabla \mathbb{G}_{n_\tau-1}(\mathbf{x}_{n_\tau-1}) \nabla \mathbb{G}_{n_\tau-2}(\mathbf{x}_{n_\tau-2}) \ldots \nabla_{\mathbf{x}_0} \mathbb{G}_0(\mathbf{x}_0) \,. && \text{(A.14)}
\end{aligned}$$

The Jacobian of $\mathbb{G}_k$ is given by $\nabla \mathbb{G}_k(\mathbf{x}_k) = \mathbb{1} + \Delta t \nabla \mathbf{G}(\mathbf{x}_k)$, $\forall k \in \{0, 1, \ldots, n_\tau - 1\}$. Hence,

$$\begin{aligned}
&\nabla_{\mathbf{x}_0} h(\mathbf{x}_{n_\tau})\\
&\quad = \nabla h(\mathbf{x}_{n_\tau}) [\mathbb{1} + \Delta t \nabla \mathbf{G}(\mathbf{x}_{n_\tau-1})][\mathbb{1} + \Delta t \nabla \mathbf{G}(\mathbf{x}_{n_\tau-2})] \ldots [\mathbb{1} + \Delta t \nabla \mathbf{G}(\mathbf{x}_0)] \,. && \text{(A.15)}
\end{aligned}$$

For sufficiently small Δt we have $[\mathbb{1} + \Delta t \nabla \mathbf{G}(\mathbf{x}_{n_\tau-1})] \simeq \exp\{\Delta t \nabla \mathbf{G}(\mathbf{x}[\tau - \Delta t])\}$. Thus, formally we obtain in the limit $\Delta t \to 0$

$$\nabla_{\mathbf{x}_0} h(\mathbf{x}[\tau]) = \nabla h(\mathbf{x}[\tau]) \mathbb{T} \exp \left[\int_0^\tau \nabla \mathbf{G}(\mathbf{x}[s]) \mathrm{d}s \right] \,, \tag{A.16}$$

where $\mathbb{T}$ is the time-order operator. □

Appendix B

Linear Empirical Closure

In this chapter we derive the set of optimal closure parameters for the SEM$_{\mathrm{det}}$ and SEM$_{\mathrm{stoch}}$ by minimization of the residual error and the Maximum-Likelihood method (Honerkamp 1994), respectively. The latter can, after some simple algebraic treatment, also be used to calculate the OU-process required for the SMR.

B.1 Minimization of the Residual Error

One possibility to obtain a set of optimal closure parameters for the SEM$_{\mathrm{det}}$ is via linear regression. In particular, by the minimization of the time-averaged norm of the residual error (3.8) (i.e., $\langle \|\boldsymbol{\epsilon}_p\|^2 \rangle$). First we rearrange (3.8) to

$$\begin{aligned} \boldsymbol{\epsilon}_p &= \frac{\mathrm{d}\mathbf{a}}{\mathrm{d}t} - \tilde{\mathbf{G}}(\mathbf{a}) - \mathbf{r} - \mathbf{La} && \text{(B.1)} \\ &\approx \frac{\mathbf{a}(t+\Delta t) - \mathbf{a}(t-\Delta t)}{2\Delta t} - \tilde{\mathbf{G}}[\mathbf{a}(t)] - \mathbf{r} - \mathbf{L}\mathbf{a}(t)\,, && \text{(B.2)} \end{aligned}$$

where Δt denotes the time step of the model output and we discretized the time derivative of the principal components by the Leapfrog scheme. With the definition of the SGS error

$$\mathbf{s}(t) = \frac{\mathbf{a}(t+\Delta t) - \mathbf{a}(t-\Delta t)}{2\Delta t} - \tilde{\mathbf{G}}[\mathbf{a}(t)] \tag{B.3}$$

(B.2) may be written as

$$\epsilon_{p_i} = s_i(t) - r_i - \mathsf{L}_{ij} a_j(t)\,. \tag{B.4}$$

The squared norm of the residual error reads

$$\|\epsilon_p\|^2 = s_i^2 + r_i^2 + \mathsf{L}_{ij}\mathsf{L}_{ik} a_j a_k - 2\left[s_i r_i + \mathsf{L}_{ij}(s_i a_j - r_i a_j)\right]\,, \tag{B.5}$$

where we suppressed the explicit time dependence for a better readability.

Thus, for the vector $\mathbf{r}$ we obtain

$$\begin{aligned} 0 &= \partial_{r_\beta} \|\varepsilon_p\|^2 && \text{(B.6)} \\ &= \delta_{i\beta}\left[2r_i - 2s_i + 2\mathsf{L}_{ij} a_j\right] && \text{(B.7)} \\ &= r_\beta - s_\beta + \mathsf{L}_{\beta j} a_j\,, && \text{(B.8)} \end{aligned}$$

which can be further simplified to

$$N_t r_i = \sum_{n=1}^{N_t} s_i^n - \mathsf{L}_{ij} a_j^n\,. \tag{B.9}$$

Dividing by N_t yields

$$r_\beta = \langle s_\beta \rangle - \mathsf{L}_{\beta j} \langle a_j \rangle \qquad \Leftrightarrow \qquad \mathbf{r} = \langle \mathbf{s} \rangle - \mathsf{L} \langle \mathbf{a} \rangle\,. \tag{B.10}$$

The minimization of (B.5) with respect to L is given by

$$\begin{aligned} 0 &= \partial_{\mathsf{L}_{\beta\gamma}} \|\varepsilon_p\|^2 && \text{(B.11)} \\ &= \delta_{i\beta}\delta_{j\gamma} a_j \mathsf{L}_{ik} a_k + \mathsf{L}_{ij} a_j \delta_{i\beta}\delta_{k\gamma} a_k - 2\delta_{i\beta}\delta_{j\gamma}\left[s_i a_j + r_i a_j\right] && \text{(B.12)} \\ &= 2\left[\mathsf{L}_{\beta j} a_j a_\gamma - s_\beta a_\gamma + r_\beta a_\gamma\right]\,, && \text{(B.13)} \end{aligned}$$

which can be written as

$$0 = \sum_{n=1}^{N_t} a_\gamma \left[\mathsf{L}_{\beta j} a_j - s_\beta + r_\beta\right]\,. \tag{B.14}$$

Using (B.10) yields

$$0 = \sum_{n=1}^{N_t} a_\gamma \left[\mathsf{L}_{\beta j} a_j - s_\beta + \langle s_\beta \rangle - \mathsf{L}_{\beta j} \langle a_j \rangle \right] \tag{B.15}$$

$$= \sum_{n=1}^{N_t} a_\gamma \left[\mathsf{L}_{\beta j} a'_j - s'_\beta \right] . \tag{B.16}$$

Hence, we obtain

$$\mathsf{L}_{\beta j} = \langle s'_\beta a'_\gamma \rangle \langle a'_\gamma a'_j \rangle^{-1} \qquad \Leftrightarrow \qquad \mathsf{L} = \langle \mathbf{s}' \mathbf{a}'^{\mathrm{T}} \rangle \langle \mathbf{a}' \mathbf{a}'^{\mathrm{T}} \rangle^{-1} . \tag{B.17}$$

Strictly speaking it remains to be shown that the Hessian is positive definite. However, this proof is not be given here but left for the reader as an exercise.

B.2 Maximum-Likelihood Method

In this section we derive the optimal set of closure parameters for the $\mathrm{SEM}_{\mathrm{stoch}}$ using the Maximum-Likelihood method. However, since the closure is essentially an OU-process that we require for both the IMM and the SMR as well, we generalize the problem by considering an arbitrary coupled system

$$\mathrm{d}\mathbf{x}(t) = \{ \mathsf{G}^x[\mathbf{x}(t), \mathbf{y}(t)] + \mathbf{r}^x + \mathsf{l}^{xx}\mathbf{x}(t) + \mathsf{l}^{xy}\mathbf{y}(t) \} \, \mathrm{d}t + \boldsymbol{\sigma}^x \mathrm{d}\mathbf{W}^x(t) \tag{B.18a}$$

$$\mathrm{d}\mathbf{y}(t) = \{ \mathsf{G}^y[\mathbf{x}(t), \mathbf{y}(t)] + \mathbf{r}^y + \mathsf{l}^{yx}\mathbf{x}(t) + \mathsf{l}^{yy}\mathbf{y}(t) \} \, \mathrm{d}t + \boldsymbol{\sigma}^y \mathrm{d}\mathbf{W}^y(t) , \tag{B.18b}$$

where $\mathbf{r}, \mathsf{l}, \boldsymbol{\sigma} = \mathit{const.}$ and $\boldsymbol{\sigma}$ is diagonal.

First we note that, because of the identical structure, we can summarize (B.18) in the general form

$$\mathrm{d} \bullet (t) = \{ \mathsf{G}^\bullet[\mathbf{x}(t), \mathbf{y}(t)] + \mathbf{r}^\bullet + \mathsf{l}^{\bullet x}\mathbf{x}(t) + \mathsf{l}^{\bullet y}\mathbf{y}(t) \} \, \mathrm{d}t + \boldsymbol{\sigma}^\bullet \mathrm{d}\mathbf{W}^\bullet(t) , \tag{B.19}$$

where $\bullet \in \mathbb{R}^m$ stands for either $\mathbf{x}$ or $\mathbf{y}$. Next we rearrange (B.19) to

$$\boldsymbol{\sigma}^\bullet \mathrm{d}\mathbf{W}^\bullet(t) = \left[\frac{\mathrm{d} \bullet (t)}{\mathrm{d}t} - \{ \mathsf{G}^\bullet[\mathbf{x}(t), \mathbf{y}(t)] + \mathbf{r}^\bullet + \mathsf{l}^{\bullet x}\mathbf{x}(t) + \mathsf{l}^{\bullet y}\mathbf{y}(t) \} \right] \mathrm{d}t . \tag{B.20}$$

This is then approximated using the Leapfrog scheme, i.e.

$$\begin{aligned}
&\boldsymbol{\sigma}^{\bullet}\Delta\tilde{\mathbf{W}}^{\bullet}(t)\\
&\quad\approx \left\{\frac{\bullet(t+\Delta t)-\bullet(t-\Delta t)}{2\Delta t} - \boldsymbol{\mathsf{G}}^{\bullet}[\mathbf{x}(t),\mathbf{y}(t)] - \mathbf{r}^{\bullet} - \boldsymbol{\mathsf{l}}^{\bullet x}\mathbf{x}(t) - \boldsymbol{\mathsf{l}}^{\bullet y}\mathbf{y}(t)\right\} 2\Delta t\,,
\end{aligned} \tag{B.21}$$

where Δt denotes the time step of the model output. Since the Leapfrog scheme requires two time steps we approximate $\Delta\tilde{\mathbf{W}}^{\bullet}(t)$ by two consecutive Euler steps

$$\Delta\tilde{\mathbf{W}}^{\bullet}(t) = \mathbf{W}(t+\Delta t) - \mathbf{W}(t-\Delta t) \tag{B.22}$$

$$= \mathbf{W}(t+\Delta t) - \mathbf{W}(t) + \mathbf{W}(t) - \mathbf{W}(t-\Delta t) \tag{B.23}$$

$$= \Delta\mathbf{W}(t) + \Delta\mathbf{W}(t-\Delta t)\,. \tag{B.24}$$

Hence, we have

$$\operatorname{var}\left[\boldsymbol{\sigma}^{\bullet}\Delta\tilde{\mathbf{W}}^{\bullet}(t)\right] = 2\Delta t\boldsymbol{\sigma}^{\bullet 2}\,. \tag{B.25}$$

With the definition of the subgrid-scale error

$$\mathbf{s}^{\bullet}(t) = \frac{\bullet(t+\Delta t)-\bullet(t-\Delta t)}{2\Delta t} - \boldsymbol{\mathsf{G}}[\mathbf{x}(t),\mathbf{y}(t)] \tag{B.26}$$

(B.21) can be written as

$$\boldsymbol{\sigma}^{\bullet}d\mathbf{W}^{\bullet}(t) = [\mathbf{s}^{\bullet}(t) - \mathbf{r}^{\bullet} - \boldsymbol{\mathsf{l}}^{\bullet x}\mathbf{x}(t) - \boldsymbol{\mathsf{l}}^{\bullet y}\mathbf{y}(t)]\,2\Delta t\,. \tag{B.27}$$

For a better readability we suppress the dependency of t in the following.

Because of (B.25) the right-hand side of (B.27) is normally distributed with $\mathcal{N}(0, 2\Delta t\boldsymbol{\sigma}^{\bullet 2})$. Thus, the Maximum-Likelihood function is given by

$$\begin{aligned}
&L(\mathbf{r}^{\bullet},\boldsymbol{\mathsf{l}}^{\bullet x},\boldsymbol{\mathsf{l}}^{\bullet y},\boldsymbol{\sigma}^{\bullet})\\
&\quad= \prod_{n=1}^{N_t} p_n(\mathbf{r},\boldsymbol{\mathsf{l}}^{\bullet x},\boldsymbol{\mathsf{l}}^{\bullet y},\boldsymbol{\sigma}^{\bullet})
\end{aligned} \tag{B.28}$$

$$
\begin{aligned}
&= \left[(2\pi)^m \det(2\Delta t\boldsymbol{\sigma}^{\bullet 2})\right]^{-\frac{N_t}{2}} \exp\left\{-\sum_{n=1}^{N_t} 2\Delta t \left[\mathbf{s}^{\bullet n} - (\mathbf{r}^{\bullet} + \mathbf{l}^{\bullet x}\mathbf{x}^n + \mathbf{l}^{\bullet y}\mathbf{y}^n)\right]^{\mathrm{T}}\right.\\
&\qquad \left.\frac{(2\Delta t\boldsymbol{\sigma}^{\bullet 2})^{-1}}{2} 2\Delta t \left[\mathbf{s}^{\bullet n} - (\mathbf{r}^{\bullet} + \mathbf{l}^{\bullet x}\mathbf{x}^n + \mathbf{l}^{\bullet y}\mathbf{y}^n)\right]\right\}
\end{aligned}
\tag{B.29}
$$

$$
\begin{aligned}
&= \left[(4\pi\Delta t)^m \prod_{i=1}^{m} \boldsymbol{\sigma}_{ii}^{\bullet\,2}\right]^{-\frac{N_t}{2}} \exp\left\{-\sum_{n=1}^{N_t} \Delta t \left[\mathbf{s}^{\bullet n} - (\mathbf{r}^{\bullet} + \mathbf{l}^{\bullet x}\mathbf{x}^n + \mathbf{l}^{\bullet y}\mathbf{y}^n)\right]^{\mathrm{T}}\right.\\
&\qquad \left.\boldsymbol{\sigma}^{\bullet -2} \left[\mathbf{s}^{\bullet n} - (\mathbf{r}^{\bullet} + \mathbf{l}^{\bullet x}\mathbf{x}^n + \mathbf{l}^{\bullet y}\mathbf{y}^n)\right]\right\} .
\end{aligned}
\tag{B.30}
$$

The corresponding log-likelihood function reads

$$
\begin{aligned}
&\mathcal{L}(\mathbf{r}^{\bullet}, \mathbf{l}^{\bullet x}, \mathbf{l}^{\bullet y}, \boldsymbol{\sigma}^{\bullet})\\
&\qquad = \log(L) && \text{(B.31)}\\
&\qquad = -\frac{N_t}{2}\log[(4\pi\Delta t)^m] - N_t \sum_{i=1}^{m} \log\left(\boldsymbol{\sigma}_{ii}^{\bullet}\right)\\
&\qquad - \frac{\Delta t}{\boldsymbol{\sigma}_{ii}^{\bullet\,2}} \sum_{n=1}^{N_t} \left[s_i^{\bullet n} - (r_i^{\bullet} + \mathbf{l}_{ij}^{\bullet x} x_j^n + \mathbf{l}_{ik}^{\bullet y} y_k^n)\right] \left[s_i^{\bullet n} - (r_i^{\bullet} + \mathbf{l}_{il}^{\bullet x} x_l^n + \mathbf{l}_{im}^{\bullet y} y_m^n)\right] . && \text{(B.32)}
\end{aligned}
$$

Thus for the vector $\mathbf{r}^{\bullet}$ we obtain

$$
\begin{aligned}
0 &= \frac{\partial \mathcal{L}}{\partial r_{\beta}^{\bullet}} && \text{(B.33)}\\
&= -\frac{\Delta t}{\boldsymbol{\sigma}_{ii}^{\bullet\,2}} \sum_{n=1}^{N_t} \partial_{r_{\beta}^{\bullet}} \left[s_i^{\bullet n} - (r_i^{\bullet} + \mathbf{l}_{ij}^{\bullet x} x_j^n + \mathbf{l}_{ik}^{\bullet y} y_k^n)\right] \left[s_i^{\bullet n} - (r_i^{\bullet} + \mathbf{l}_{il}^{\bullet x} x_l^n + \mathbf{l}_{im}^{\bullet y} y_m^n)\right] && \text{(B.34)}\\
&= \sum_{n=1}^{N_t} \delta_{i\beta} \left\{\left[s_i^{\bullet n} - (r_i^{\bullet} + \mathbf{l}_{il}^{\bullet x} x_l^n + \mathbf{l}_{im}^{\bullet y} y_m^n)\right] + \left[s_i^{\bullet n} - (r_i^{\bullet} + \mathbf{l}_{ij}^{\bullet x} x_j^n + \mathbf{l}_{ik}^{\bullet y} y_k^n)\right]\right\} && \text{(B.35)}\\
&= \sum_{n=1}^{N_t} 2\left[s_{\beta}^{\bullet n} - (r_{\beta}^{\bullet} + \mathbf{l}_{\beta j}^{\bullet x} x_j^n + \mathbf{l}_{\beta k}^{\bullet y} y_k^n)\right] . && \text{(B.36)}
\end{aligned}
$$

This can be simplified to

$$N_t r^\bullet_\beta = \sum_{n=1}^{N_t} \left[s^{\bullet\,n}_\beta - (\boldsymbol{\mathsf{l}}^{\bullet x}_{\beta j} x^n_j + \boldsymbol{\mathsf{l}}^{\bullet y}_{\beta k} y^n_k) \right] , \tag{B.37}$$

which is equivalent to

$$r^\bullet_\beta = \left\langle s^\bullet_\beta \right\rangle - \boldsymbol{\mathsf{l}}^{\bullet x}_{\beta j} \left\langle x_j \right\rangle - \boldsymbol{\mathsf{l}}^{\bullet y}_{\beta k} \left\langle y_k \right\rangle \qquad \Leftrightarrow \qquad \mathbf{r}^\bullet = \left\langle \mathbf{s}^\bullet \right\rangle - \boldsymbol{\mathsf{l}}^{\bullet x} \left\langle \mathbf{x} \right\rangle - \boldsymbol{\mathsf{l}}^{\bullet y} \left\langle \mathbf{y} \right\rangle . \tag{B.38}$$

The calculation of the linear term acting on the first variable $\boldsymbol{\mathsf{l}}^{\bullet x}$ is given by

$$
\begin{align}
0 &= \frac{\partial \mathcal{L}}{\partial \boldsymbol{\mathsf{l}}^{\bullet x}_{\beta\gamma}} \tag{B.39} \\
&= -\frac{\Delta t}{{\boldsymbol{\sigma}^{\bullet}_{ii}}^{2}} \sum_{n=1}^{N_t} \partial_{\boldsymbol{\mathsf{l}}^{\bullet x}_{\beta\gamma}} \left[s^{\bullet n}_i - (r^\bullet_i + \boldsymbol{\mathsf{l}}^{\bullet x}_{ij} x^n_j + \boldsymbol{\mathsf{l}}^{\bullet y}_{ik} y^n_k) \right] \left[s^{\bullet n}_i - (r^\bullet_i + \boldsymbol{\mathsf{l}}^{\bullet x}_{il} x^n_l + \boldsymbol{\mathsf{l}}^{\bullet y}_{im} y^n_m) \right] \tag{B.40} \\
&= \sum_{n=1}^{N_t} \delta_{i\beta} \left\{ \delta_{j\gamma} x^n_j \left[s^{\bullet n}_i - (r^\bullet_i + \boldsymbol{\mathsf{l}}^{\bullet x}_{il} x^n_l + \boldsymbol{\mathsf{l}}^{\bullet y}_{im} y^n_m) \right] \right. \nonumber \\
&\quad \left. + \delta_{l\gamma} x^n_l \left[s^{\bullet n}_i - (r^\bullet_i + \boldsymbol{\mathsf{l}}^{\bullet x}_{ij} x^n_j + \boldsymbol{\mathsf{l}}^{\bullet y}_{ik} y^n_k) \right] \right\} \tag{B.41} \\
&= \sum_{n=1}^{N_t} 2 x^n_\gamma \left[s^{\bullet\,n}_\beta - (r^\bullet_\beta + \boldsymbol{\mathsf{l}}^{\bullet x}_{\beta j} x^n_j + \boldsymbol{\mathsf{l}}^{\bullet y}_{\beta k} y^n_k) \right] , \tag{B.42}
\end{align}
$$

which can be simplify to

$$0 = \sum_{n=1}^{N_t} x^n_\gamma \left[s^{\bullet\,n}_\beta - (r^\bullet_\beta + \boldsymbol{\mathsf{l}}^{\bullet x}_{\beta j} x^n_j + \boldsymbol{\mathsf{l}}^{\bullet y}_{\beta k} y^n_k) \right] . \tag{B.43}$$

Using (B.38) yields

$$
\begin{align}
0 &= \sum_{n=1}^{N_t} x^n_\gamma \left[s^{\bullet\,n}_\beta - \left\langle s^\bullet_\beta \right\rangle - (\boldsymbol{\mathsf{l}}^{\bullet x}_{\beta j} x^n_j - \boldsymbol{\mathsf{l}}^{\bullet x}_{\beta j} \left\langle x_j \right\rangle + \boldsymbol{\mathsf{l}}^{\bullet y}_{\beta k} y^n_k - \boldsymbol{\mathsf{l}}^{\bullet y}_{\beta k} \left\langle y_k \right\rangle) \right] \tag{B.44} \\
&= \sum_{n=1}^{N_t} x^n_\gamma \left[{s'}^{\bullet\,n}_\beta - (\boldsymbol{\mathsf{l}}^{\bullet x}_{\beta j} {x'}^n_j + \boldsymbol{\mathsf{l}}^{\bullet y}_{\beta k} {y'}^n_k) \right] . \tag{B.45}
\end{align}
$$

Thus,

$$
\begin{aligned}
&& \mathsf{l}^{\bullet x}_{\beta j} &= \left[\left\langle {x'}_\gamma {s'}^{\bullet}_{\beta}\right\rangle - \mathsf{l}^{\bullet y}_{\beta k}\left\langle {x'}_\gamma {y'}_k\right\rangle\right]\left\langle {x'}_\gamma {x'}_j\right\rangle^{-1} && \text{(B.46a)}\\
\Leftrightarrow && \mathsf{l}^{\bullet x} &= \left[\left\langle \mathbf{s}'^{\bullet}\mathbf{x}'^{\mathrm{T}}\right\rangle - \mathsf{l}^{\bullet y}\left\langle \mathbf{y}'\mathbf{x}'^{\mathrm{T}}\right\rangle\right]\left\langle \mathbf{x}'\mathbf{x}'^{\mathrm{T}}\right\rangle^{-1} . && \text{(B.46b)}
\end{aligned}
$$

Analogously we obtain for $\mathsf{l}^{\bullet y}$

$$
0 = \sum_{n=1}^{N_t} y^n_\gamma \left[{s'}^{\bullet n}_{\beta} - \left(\mathsf{l}^{\bullet x}_{\beta j}{x'}^n_j + \mathsf{l}^{\bullet y}_{\beta k}{y'}^n_k\right)\right] . \tag{B.47}
$$

Inserting (B.46) yields

$$
0 = \left\langle {y'}_\gamma {s'}^{\bullet}_{\beta}\right\rangle - \left[\left\langle {x'}_l {s'}^{\bullet}_{\beta}\right\rangle - \mathsf{l}^{\bullet y}_{\beta k}\left\langle {x'}_l {y'}_k\right\rangle\right]\left\langle {x'}_l {x'}_j\right\rangle^{-1}\left\langle x'_j y'_\gamma\right\rangle - \mathsf{l}^{\bullet y}_{\beta k}\left\langle {y'}_k {y'}_\gamma\right\rangle , \tag{B.48}
$$

which can be rearranged to

$$
\begin{aligned}
&& \mathsf{l}^{\bullet y}_{\beta k} &= \left[\left\langle {y'}_\gamma {s'}^{\bullet}_{\beta}\right\rangle - \left\langle {x'}_l {s'}^{\bullet}_{\beta}\right\rangle\left\langle {x'}_l {x'}_j\right\rangle^{-1}\left\langle x'_j y'_\gamma\right\rangle\right]\\
&& &\quad\times\left[\left\langle {y'}_k {y'}_\gamma\right\rangle - \left\langle {x'}_l {y'}_k\right\rangle\left\langle {x'}_l {x'}_j\right\rangle^{-1}\left\langle x'_j y'_\gamma\right\rangle\right]^{-1} && \text{(B.49a)}\\
\Leftrightarrow && \mathsf{l}^{\bullet y} &= \left[\left\langle \mathbf{s}'^{\bullet}\mathbf{y}'^{\mathrm{T}}\right\rangle - \left\langle \mathbf{s}'^{\bullet}\mathbf{x}'^{\mathrm{T}}\right\rangle\left\langle \mathbf{x}'\mathbf{x}'^{\mathrm{T}}\right\rangle^{-1}\left\langle \mathbf{x}'\mathbf{y}'^{\mathrm{T}}\right\rangle\right]\\
&& &\quad\times\left[\left\langle \mathbf{y}'\mathbf{y}'^{\mathrm{T}}\right\rangle - \left\langle \mathbf{y}'\mathbf{x}'^{\mathrm{T}}\right\rangle\left\langle \mathbf{x}'\mathbf{x}'^{\mathrm{T}}\right\rangle^{-1}\left\langle \mathbf{x}'\mathbf{y}'^{\mathrm{T}}\right\rangle\right]^{-1} . && \text{(B.49b)}
\end{aligned}
$$

The calculation of $\boldsymbol{\sigma}^{\bullet}$ yields

$$
\begin{aligned}
0 &= \frac{\partial\mathcal{L}}{\partial\boldsymbol{\sigma}^{\bullet}_{\beta\gamma}} && \text{(B.50)}\\
&= -\partial_{\boldsymbol{\sigma}^{\bullet}_{\beta\gamma}} N_t\sum_{i=1}^{m}\log\left(\boldsymbol{\sigma}^{\bullet}_{ii}\right) - \partial_{\boldsymbol{\sigma}^{\bullet}_{\beta\gamma}}\frac{\Delta t}{\boldsymbol{\sigma}^{\bullet 2}_{ii}}\sum_{n=1}^{N_t}\left\{\left[s^{\bullet n}_i - \left(r^{\bullet}_i + \mathsf{l}^{\bullet x}_{ij}x^n_j + \mathsf{l}^{\bullet y}_{ik}y^n_k\right)\right]\right.\\
&\quad\times\left.\left[s^{\bullet n}_i - \left(r^{\bullet}_i + \mathsf{l}^{\bullet x}_{il}x^n_l + \mathsf{l}^{\bullet y}_{im}y^n_m\right)\right]\right\} && \text{(B.51)}\\
&= -N_t\sum_{i=1}^{m}\frac{\delta_{i\beta}\delta_{\beta\gamma}}{\boldsymbol{\sigma}^{\bullet}_{\beta\gamma}} + \frac{2\Delta t}{\boldsymbol{\sigma}^{\bullet 3}_{\beta\gamma}}\sum_{n=1}^{N_t}\delta_{i\beta}\delta_{\beta\gamma}\left\{\left[s^{\bullet n}_i - \left(r^{\bullet}_i + \mathsf{l}^{\bullet x}_{ij}x^n_j + \mathsf{l}^{\bullet y}_{ik}y^n_k\right)\right]\right.\\
&\quad\times\left.\left[s^{\bullet n}_i - \left(r^{\bullet}_i + \mathsf{l}^{\bullet x}_{il}x^n_l + \mathsf{l}^{\bullet y}_{im}y^n_m\right)\right]\right\} && \text{(B.52)}
\end{aligned}
$$

$$
\begin{aligned}
&= -\frac{N_t}{\boldsymbol{\sigma}^{\bullet}_{\beta\beta}} + \frac{2\Delta t}{{\boldsymbol{\sigma}^{\bullet}}^{3}_{\beta\beta}} \sum_{n=1}^{N_t} \left\{ \left[{s^{\bullet}_{\beta}}^{n} - (r^{\bullet}_{\beta} + \mathsf{l}^{\bullet x}_{\beta j} x^{n}_{j} + \mathsf{l}^{\bullet y}_{\beta k} y^{n}_{k}) \right] \right. \\
&\quad \left. \times \left[{s^{\bullet}_{\beta}}^{n} - (r^{\bullet}_{\beta} + \mathsf{l}^{\bullet x}_{\beta l} x^{n}_{l} + \mathsf{l}^{\bullet y}_{\beta m} y^{n}_{m}) \right] \right\} , \qquad \text{(B.53)}
\end{aligned}
$$

which results in

$$
{\boldsymbol{\sigma}^{\bullet}}^{2}_{\beta\beta} = 2\Delta t \left\langle \left[s^{\bullet}_{\beta} - (r^{\bullet}_{\beta} + \mathsf{l}^{\bullet x}_{\beta j} x_{j} + \mathsf{l}^{\bullet y}_{\beta k} y_{k}) \right] \left[s^{\bullet}_{\beta} - (r^{\bullet}_{\beta} + \mathsf{l}^{\bullet x}_{\beta l} x_{l} + \mathsf{l}^{\bullet y}_{\beta m} y_{m}) \right] \right\rangle \qquad \text{(B.54a)}
$$

$$
\Leftrightarrow \quad {\boldsymbol{\sigma}^{\bullet}}^{2} = 2\Delta t \left\langle \left[s^{\bullet} - (r^{\bullet} + \mathsf{l}^{\bullet x}\mathbf{x} + \mathsf{l}^{\bullet y}\mathbf{y}) \right] \left[s^{\bullet} - (r^{\bullet} + \mathsf{l}^{\bullet x}\mathbf{x} + \mathsf{l}^{\bullet y}\mathbf{y}) \right]^{\mathrm{T}} \right\rangle . \qquad \text{(B.54b)}
$$

Let $\mathbf{r}^{\bullet} = \mathbf{r}, \mathsf{l}^{\bullet x} = \mathsf{L}, \mathsf{l}^{\bullet y} = 0, \mathbf{y} = 0$, and $\mathbf{x} = \mathbf{a}$. Then the comparison of (B.10) with (B.38) and (B.17) with (B.46) shows that we obtain the same set of optimal closure parameters with both methods.

For the calculation of the OU-process in the SMR, we use an Euler scheme instead of the Leapfrog scheme presented above. Furthermore, we do not use the model time step but $\Delta t = 1$ day and set $\mathbf{r}^{\bullet} = 0$. Thus, the constant vector vanishes and the variances changes to second moments (e.g., $\langle \mathbf{x}'\mathbf{y}'^{\mathrm{T}} \rangle \longrightarrow \langle \mathbf{x}\mathbf{y}^{\mathrm{T}} \rangle$) in the equations of the linear closure parameters ($\mathsf{l}^{\bullet x}$ and $\mathsf{l}^{\bullet y}$).

Appendix C

Stochastic Mode Reduction

This appendix contains the calculations needed for the derivation and application of the SMR. Note that in this chapter we do not apply Einstein's summation convention.

C.1 Projection Operator and Generalized Inverse of L_1

Consider the initial value problem of a damped OU-process (Gardiner 2009)

$$\partial_t g(\mathbf{x},\mathbf{y},t) = L_1 g(\mathbf{x},\mathbf{y},t) - f(\mathbf{x},\mathbf{y},t_r) \tag{C.1a}$$

$$g(\mathbf{x},\mathbf{y},0) = h(\mathbf{x},\mathbf{y},t_r) \tag{C.1b}$$

with an arbitrary function $f(\mathbf{x},\mathbf{y},t_r)$ as inhomogeneity, the L_1 operator (6.16) (only acting on the slow variable), and an arbitrary reference time t_r. The solution of (C.1) reads

$$g(\mathbf{x},\mathbf{y},t) = e^{L_1 t} h(\mathbf{x},\mathbf{y},t_r) - \int\limits_0^t e^{L_1(t-s)} f(\mathbf{x},\mathbf{y},t_r) \mathrm{d}s\,, \tag{C.2}$$

which can easily be proven by insertion.

First we decompose L_1 in its eigenfunctions $e_\mu(\mathbf{y})$, i.e.

$$L_1 e_\mu = \lambda_\mu e_\mu \,, \tag{C.3}$$

where λ_μ is the eigenvalue corresponding to e_μ. With this we can decompose an arbitrary function $k(\mathbf{x}, \mathbf{y}, t)$ as

$$k(\mathbf{x}, \mathbf{y}, t) = \sum_\mu k_\mu(\mathbf{x}, t) e_\mu(\mathbf{y}) \,. \tag{C.4}$$

From (C.4) we obtain for g, h, and f in the solution (C.2)

$$g_\mu(\mathbf{x}, t) = h_\mu(\mathbf{x}, t_r) e^{\lambda_\mu t} - \begin{cases} f_\mu(\mathbf{x}, t_r) t & , \lambda_\mu = 0 \\ (1 - e^{\lambda_\mu t}) \frac{f_\mu(\mathbf{x}, t_r)}{\lambda_\mu} & , \text{else} \,. \end{cases} \tag{C.5}$$

Since (C.1) is the differential equation of the damped OU-process, the solution is well defined for an initialization at $t \to -\infty$ (i.e., $\lambda_\mu \geq 0 \,, \forall \mu$). Consider (C.5) in the limit $t \to -\infty$

1. with $f = 0$. All eigenmodes with $\lambda \neq 0$ are suppressed and only those with $\lambda_\mu = 0$ contribute to the solution. However, per definition those eigenmodes span the nullspace of L_1, i.e.

$$\lim_{t \to -\infty} g(\mathbf{x}, \mathbf{y}, t) \Big|_{f=0} = \mathcal{P} h(\mathbf{x}, \mathbf{y}, t_r) \,. \tag{C.6}$$

2. with $h = 0$. In this case the eigenmodes with $\lambda_\mu = 0$ diverge and the remaining modes converge to $f_\mu(\mathbf{x}, t_r)/\lambda_\mu$. Hence,

$$\lim_{t \to -\infty} g(\mathbf{x}, \mathbf{y}, t) \Big|_{h=0} = L_1^{-1} f(\mathbf{x}, \mathbf{y}, t_r) \,, \tag{C.7}$$

   if $\mathcal{P} f = 0$.

Nevertheless, (C.6) and (C.7) do not provide an exact expression for both the projection operator onto $\ker L_1$ and the generalized inverse L_1^{-1}. For those we need to rearrange (C.2) by noting that

$$h(\mathbf{x},\mathbf{y},t_r) = \int \mathrm{d}^F\tilde{\mathbf{y}}\delta(\mathbf{y}-\tilde{\mathbf{y}})h(\mathbf{x},\tilde{\mathbf{y}},t_r) \tag{C.8a}$$

$$f(\mathbf{x},\mathbf{y},t_r) = \int \mathrm{d}^F\tilde{\mathbf{y}}\delta(\mathbf{y}-\tilde{\mathbf{y}})f(\mathbf{x},\tilde{\mathbf{y}},t_r)\,. \tag{C.8b}$$

On substituting (C.8) in (C.2) we find, after some algebra,

$$g(\mathbf{x},\mathbf{y},t) = \int \left[e^{L_1 t}h(\mathbf{x},\tilde{\mathbf{y}},t_r) + \int\limits_0^{-t} e^{-L_1 s}f(\mathbf{x},\tilde{\mathbf{y}},t_r)\mathrm{d}s \right] \delta(\mathbf{y}-\tilde{\mathbf{y}})\mathrm{d}^F\tilde{\mathbf{y}}\,. \tag{C.9}$$

Thus, following (C.6), we have for the projection operator

$$\begin{aligned}\mathcal{P}h &= \lim_{t\to-\infty} g(\mathbf{x},\mathbf{y},t)\Big|_{f=0} \\ &= \int \mathrm{d}^F\tilde{\mathbf{y}} \lim_{t\to-\infty} e^{L_1 t}\delta(\mathbf{y}-\tilde{\mathbf{y}})h(\mathbf{x},\tilde{\mathbf{y}},t_r) \\ &= \int \mathrm{d}^F\mathbf{y}p_s(\mathbf{y})h(\mathbf{x},\mathbf{y},t_r) \equiv \mathbb{E}\left[h(\mathbf{x},\mathbf{y},t_r)\right]_{\mathrm{OU}}\;,\end{aligned} \tag{C.10}$$

where we renamed the integration variable $\mathbf{y}$ in the last step and $p_s(\mathbf{y})$ denotes the stationary distribution of the OU-process (C.13). Obviously, since the projection operator $\mathcal{P}$ eliminates the fast variable, $p^{(0)} \in \ker L_1$ has to be independent of $\mathbf{y}$.

Furthermore, for vanishing initial condition ($h = 0$) the generalized inverse reads

$$\begin{aligned}L_1^{-1}f &= \lim_{t\to-\infty} g(\mathbf{x},\mathbf{y},t)\Big|_{h=0} \\ &= \int\limits_0^\infty \int \mathrm{d}^F\tilde{\mathbf{y}} \lim_{s\to-\infty} e^{-L_1 s}\delta(\mathbf{y}-\tilde{\mathbf{y}})f(\mathbf{x},\tilde{\mathbf{y}},t_r)\mathrm{d}s \\ &= \int\limits_0^\infty \int \mathrm{d}^F\tilde{\mathbf{y}}p(\tilde{\mathbf{y}},s|\mathbf{y},0)f(\mathbf{x},\tilde{\mathbf{y}},t_r)\mathrm{d}s \equiv \int\limits_0^\infty \mathbb{E}\left[f(\mathbf{x},\tilde{\mathbf{y}}[s],t_r)|\tilde{\mathbf{y}}(0)=\mathbf{y}\right]_{\mathrm{OU}}\mathrm{d}s\,.\end{aligned} \tag{C.11}$$

From this follows

$$\begin{aligned}\mathcal{P}L_1^{-1}f &= \int\limits_0^\infty \int \mathrm{d}^F\mathbf{y} \int d^F\tilde{\mathbf{y}} p(\tilde{\mathbf{y}}, s|\mathbf{y}, 0) p_s(\mathbf{y}) f(\mathbf{x}, \tilde{\mathbf{y}}, t_r)\mathrm{d}s \\ &= \int\limits_0^\infty \mathbb{E}\left[f(\mathbf{x}, \tilde{\mathbf{y}}[s], t_r)\right]_{\mathrm{OU}} \mathrm{d}s\,. \end{aligned} \tag{C.12}$$

Since (C.2) with $f = 0$ describes a damped OU-process, its stationary distribution $p_s(\mathbf{y})$ is given by

$$p_s(\mathbf{y}) = \frac{1}{\sqrt{(2\pi)^F \det \mathsf{D}}} \exp\left[-\frac{1}{2}\mathbf{y}^{\mathrm{T}}\mathsf{D}^{-1}\mathbf{y}\right], \tag{C.13}$$

where the variance can be calculated by the Lyapunov equation

$$-\mathbf{\Lambda}\mathsf{D} - \mathsf{D}\mathbf{\Lambda}^{\mathrm{T}} = \boldsymbol{\sigma}^{\star y}(\boldsymbol{\sigma}^{\star y})^{\mathrm{T}}\,. \tag{C.14}$$

Before we solve for $\mathsf{D} \in \mathbb{R}^{F\times F}$ we first note that in general the drift term of the OU-process (i.e., $\mathbf{l}_{\mathrm{OU}}^{yy}$) has complex eigenvalues $\mu_j = -\hat{\gamma}_j \pm \imath\hat{\omega}_j$ that form a complex conjugate pair (i.e., $\exists \mu_j, \mu_k$ with $\mu_j^* = \mu_k$ and $j \neq k$). Thus, in section 6.2 we rearranged $\mathbf{\Lambda}$ into a block-diagonal matrix that consists either of 2-by-2 blocks given by

$$\begin{pmatrix} -\hat{\gamma}_j & \hat{\omega}_j \\ -\hat{\omega}_j & -\hat{\gamma}_j \end{pmatrix} \tag{C.15}$$

or of $-\hat{\gamma}_j$ on the main diagonal and 0 else. For the special case where $\mathbf{\Lambda}, \mathsf{D}, \mathbf{\Sigma} \in \mathbb{R}^{3\times 3}$ (i.e., $F = 3$) we solve the Lyapunov equation analytically:

Let $\boldsymbol{\gamma}, \boldsymbol{\omega} \in \mathbb{R}^3$ be the vectors of the real and imaginary part of the eigenvalues of $\mathbf{\Lambda}$, respectively, given by

$$\gamma_i = |\mathbf{\Lambda}_{ii}| \tag{C.16}$$

and

$$\omega_i = \begin{cases} \boldsymbol{\Lambda}_{ii+1}, & \text{if } \boldsymbol{\Lambda}_{ii+1} \neq 0 \\ \boldsymbol{\Lambda}_{ii-1}, & \text{if } \boldsymbol{\Lambda}_{ii-1} \neq 0 \\ 0, & \text{else} \end{cases} \tag{C.17}$$

(Dolaptchiev et al. 2013a). Then the variance reads

$$\mathsf{\mathbf{D}}_{ij} = \begin{cases} \frac{\boldsymbol{\Sigma}_{ii}}{2\gamma_i}, & \omega_i = 0, j = i \\ \frac{(\gamma_i+\gamma_{i+1})\boldsymbol{\Sigma}_{ii+1}+\omega_{i+1}\boldsymbol{\Sigma}_{ii+2}}{(\gamma_i+\gamma_{i+1})^2+\omega_{i+1}^2}, & \omega_i = 0, j = i+1, \omega_j > 0 \\ \frac{(\gamma_i+\gamma_{i+2})\boldsymbol{\Sigma}_{ii+2}+\omega_{i+2}\boldsymbol{\Sigma}_{ii+1}}{(\gamma_i+\gamma_{i+1})^2+\omega_{i+1}^2}, & \omega_i = 0, j = i+2, \omega_j < 0 \\ \frac{(2\gamma_i^2+\omega_i^2)\boldsymbol{\Sigma}_{ii}+\omega_i^2\boldsymbol{\Sigma}_{i+1i+1}+2\gamma_i\omega_i\boldsymbol{\Sigma}_{ii+1}}{4\gamma_i(\gamma_i^2+\omega_i^2)}, & \omega_i > 0, j = i \\ \frac{\omega_i(\boldsymbol{\Sigma}_{i+1i+1}-\boldsymbol{\Sigma}_{ii})+2\gamma_2\boldsymbol{\Sigma}_{ii+1}}{4(\gamma_i^2+\omega_i^2)}, & \omega_i > 0, j = i+1 \\ \frac{(2\gamma_i^2+\omega_i^2)\boldsymbol{\Sigma}_{ii}+\omega_i^2\boldsymbol{\Sigma}_{i-1i-1}+2\gamma_i\omega_i\boldsymbol{\Sigma}_{i-1i}}{4\gamma_i(\gamma_i^2+\omega_i^2)}, & \omega_i < 0, j = i\,, \end{cases} \tag{C.18}$$

where the remaining components are obtained by $\mathsf{\mathbf{D}} = \mathsf{\mathbf{D}}^{\mathrm{T}}$.

From (C.18) cases where $\boldsymbol{\Lambda}$ is either exact diagonal or only consisting of one 2-by-2 block can be easily derived. However for a general $\boldsymbol{\Lambda} \in \mathbb{R}^{F\times F}$, the analytic solution is more complex. In this case we first partition the matrices $\boldsymbol{\Lambda}, \mathsf{\mathbf{D}}$, and $\boldsymbol{\Sigma}$ into submatrices and write the Lyapunov equation as

$$-\begin{pmatrix} \boldsymbol{\Lambda}_{11} & 0 \\ 0 & \boldsymbol{\Lambda}_{22} \end{pmatrix} \begin{pmatrix} \mathsf{\mathbf{D}}_{11} & \mathsf{\mathbf{D}}_{12} \\ \mathsf{\mathbf{D}}_{12}^{\mathrm{T}} & \mathsf{\mathbf{D}}_{22} \end{pmatrix} - \begin{pmatrix} \mathsf{\mathbf{D}}_{11} & \mathsf{\mathbf{D}}_{12} \\ \mathsf{\mathbf{D}}_{12}^{\mathrm{T}} & \mathsf{\mathbf{D}}_{22} \end{pmatrix} \begin{pmatrix} \boldsymbol{\Lambda}_{11}^{\mathrm{T}} & 0 \\ 0 & \boldsymbol{\Lambda}_{22}^{\mathrm{T}} \end{pmatrix} = \begin{pmatrix} \boldsymbol{\Sigma}_{11} & \boldsymbol{\Sigma}_{12} \\ \boldsymbol{\Sigma}_{12}^{\mathrm{T}} & \boldsymbol{\Sigma}_{22} \end{pmatrix}. \tag{C.19}$$

From this follows for each submatrix (Chu 1989)

$$-\boldsymbol{\Lambda}_{11}\mathsf{\mathbf{D}}_{11} - \mathsf{\mathbf{D}}_{11}\boldsymbol{\Lambda}_{11}^{\mathrm{T}} = \boldsymbol{\Sigma}_{11} \tag{C.20a}$$

$$-\boldsymbol{\Lambda}_{11}\mathsf{\mathbf{D}}_{12} - \mathsf{\mathbf{D}}_{12}\boldsymbol{\Lambda}_{22}^{\mathrm{T}} = \boldsymbol{\Sigma}_{12} \tag{C.20b}$$

$$-\boldsymbol{\Lambda}_{22}\mathsf{\mathbf{D}}_{22} - \mathsf{\mathbf{D}}_{22}\boldsymbol{\Lambda}_{22}^{\mathrm{T}} = \boldsymbol{\Sigma}_{22}\,. \tag{C.20c}$$

Since $\boldsymbol{\Lambda}$ is of block-diagonal form, $\boldsymbol{\Lambda}_{11}$ and $\boldsymbol{\Lambda}_{22}$ are as well. Thus, so far we only reduced the dimension of the problem without solving the Lyapunov equation. However, the matrix partition can be applied recursively until $\bar{\mathbf{\Lambda}}_{11}$ [where $\bar{(\cdot)}$ indicates the last iteration] is either a scalar or a 2-by-2 block (C.15). In both cases, the corresponding $\bar{\mathbf{D}}$ is given by (C.18). From this we can recursively obtain the full variance of the OU-process $\mathbf{D}$. In practice we compute the solution of the Lyapunov equation (C.14) numerically with the NAG routine *f08qhf*.

C.2 Series Expansion of the Fokker-Planck Equation

The leading order FPE is given by

$$\partial_t p^{(0)} = L_3 p^{(0)} - \mathcal{P} L_2 L_1^{-1} L_2 p^{(0)} \,. \tag{C.21}$$

First we consider

$$\begin{aligned} L_1^{-1} L_2 p^{(0)} &= -L_1^{-1} [f_1(\mathbf{x},\mathbf{y}) \cdot \nabla_x + g_1(\mathbf{x},\mathbf{y}) \cdot \nabla_y] p^{(0)} \\ &= -L_1^{-1} f_1(\mathbf{x},\mathbf{y}) \cdot \nabla_x p^{(0)} \,, \end{aligned} \tag{C.22}$$

since $p^{(0)}$ depends only on the slow variable. Application of the generalized inverse (C.11) yields

$$L_1^{-1} L_2 p^{(0)} = -\int\limits_0^\infty \mathbb{E}\left[f_1(\mathbf{x},\tilde{\mathbf{y}}[\tau]) | \tilde{\mathbf{y}}(0) = \mathbf{y}\right]_{\mathrm{OU}} \mathrm{d}\tau \cdot \nabla_x p^{(0)} \,. \tag{C.23}$$

Hence,

$$\begin{aligned} &-\mathcal{P} L_2 L_1^{-1} L_2 p^{(0)} \\ &\quad = -\mathcal{P}[f_1(\mathbf{x},\mathbf{y}) \cdot \nabla_x + g_1(\mathbf{x},\mathbf{y}) \cdot \nabla_y] \int\limits_0^\infty \mathbb{E}\left[f_1(\mathbf{x},\tilde{\mathbf{y}}[\tau]) | \tilde{\mathbf{y}}(0) = \mathbf{y}\right]_{\mathrm{OU}} \mathrm{d}\tau \cdot \nabla_x p^{(0)} \\ &\quad = -\mathcal{P} f_1(\mathbf{x},\mathbf{y}) \otimes \int\limits_0^\infty \mathbb{E}\left[f_1(\mathbf{x},\tilde{\mathbf{y}}[\tau]) | \tilde{\mathbf{y}}(0) = \mathbf{y}\right]_{\mathrm{OU}} \mathrm{d}\tau : \nabla_x \nabla_x p^{(0)} \end{aligned}$$

$$
\begin{aligned}
&-\mathcal{P}\int_0^\infty [f_1(\mathbf{x},\mathbf{y})\cdot\nabla_x]\mathbb{E}\left[f_1(\mathbf{x},\tilde{\mathbf{y}}[\tau])|\tilde{\mathbf{y}}(0)=\mathbf{y}\right]_{\mathrm{OU}}\,\mathrm{d}\tau\cdot\nabla_x p^{(0)} \\
&-\mathcal{P}[g_1(\mathbf{x},\mathbf{y})\cdot\nabla_y]\int_0^\infty \mathbb{E}\left[f_1(\mathbf{x},\tilde{\mathbf{y}}[\tau])|\tilde{\mathbf{y}}(0)=\mathbf{y}\right]_{\mathrm{OU}}\,\mathrm{d}\tau\cdot\nabla_x p^{(0)} \qquad \text{(C.24)} \\
&\equiv\; I_1+I_2+I_3\,. \qquad \text{(C.25)}
\end{aligned}
$$

The first term can be further simplified to

$$
\begin{aligned}
I_1 &= -\mathcal{P}f_1(\mathbf{x},\mathbf{y})\otimes\int_0^\infty \mathbb{E}\left[f_1(\mathbf{x},\tilde{\mathbf{y}}[\tau])|\tilde{\mathbf{y}}(0)=\mathbf{y}\right]_{\mathrm{OU}}\,\mathrm{d}\tau : \nabla_x\nabla_x p^{(0)} \\
&= -\int_0^\infty \mathbb{E}\left[f_1(\mathbf{x},\mathbf{y})\otimes f_1(\mathbf{x},\mathbf{y}[\tau])\right]_{\mathrm{OU}}\,\mathrm{d}\tau : \nabla_x\nabla_x p^{(0)}\,. \qquad \text{(C.26)}
\end{aligned}
$$

The second term reads

$$
\begin{aligned}
I_2 &= -\mathcal{P}\int_0^\infty [f_1(\mathbf{x},\mathbf{y})\cdot\nabla_x]\mathbb{E}\left[f_1(\mathbf{x},\tilde{\mathbf{y}}[\tau])|\tilde{\mathbf{y}}(0)=\mathbf{y}\right]_{\mathrm{OU}}\,\mathrm{d}\tau\cdot\nabla_x p^{(0)} \\
&= -\int_0^\infty \mathbb{E}\left[\{f_1(\mathbf{x},\mathbf{y})\cdot\nabla_x\}f_1(\mathbf{x},\mathbf{y}[\tau])\right]_{\mathrm{OU}}\,\mathrm{d}\tau\cdot\nabla_x p^{(0)}\,. \qquad \text{(C.27)}
\end{aligned}
$$

The last term can, via partial integration with respect to the fast variable in the projection operator $\mathcal{P}$, be written as

$$
\begin{aligned}
I_3 &= -\mathcal{P}[g_1(\mathbf{x},\mathbf{y})\cdot\nabla_y]\int_0^\infty \mathbb{E}\left[f_1(\mathbf{x},\tilde{\mathbf{y}}[\tau])|\tilde{\mathbf{y}}(0)=\mathbf{y}\right]_{\mathrm{OU}}\,\mathrm{d}\tau\cdot\nabla_x p^{(0)} \qquad \text{(C.28)} \\
&= -\left[\int g_1(\mathbf{x},\mathbf{y})\cdot\nabla_y p_s(\mathbf{y})d^F y+\mathcal{P}\nabla_y\cdot g_1(\mathbf{x},\mathbf{y})\right] \\
&\quad\times\int_0^\infty \mathbb{E}\left[f_1(\mathbf{x},\tilde{\mathbf{y}}[\tau])|\tilde{\mathbf{y}}(0)=\mathbf{y}\right]_{\mathrm{OU}}\,\mathrm{d}\tau\cdot\nabla_x p^{(0)}\,. \qquad \text{(C.29)}
\end{aligned}
$$

With the definition of the stationary distribution (C.13) and the symmetry of $\mathbf{D}$

(C.18) this results in

$$I_3 = -\mathcal{P}[g_1(\mathbf{x},\mathbf{y}) \cdot \mathsf{D}^{-1}\mathbf{y} - \nabla_y \cdot g_1(\mathbf{x},\mathbf{y})] \tag{C.30}$$

$$\times \int_0^\infty \mathbb{E}\left[f_1(\mathbf{x},\tilde{\mathbf{y}}[\tau])|\tilde{\mathbf{y}}(0) = \mathbf{y}\right]_{\mathrm{OU}} \mathrm{d}\tau \cdot \nabla_x p^{(0)} \, . \tag{C.31}$$

Finally, the application of the projection operator yields

$$\begin{aligned} I_3 = -\Bigg\{ &\int_0^\infty \mathbb{E}\left[\{g_1(\mathbf{x},\mathbf{y}) \cdot \mathsf{D}^{-1}\mathbf{y}\} f_1(\mathbf{x},\mathbf{y}[\tau])\right]_{\mathrm{OU}} \mathrm{d}\tau \\ &- \int_0^\infty \mathbb{E}\left[\{\nabla_y \cdot g_1(\mathbf{x},\mathbf{y})\} f_1(\mathbf{x},\mathbf{y}[\tau])\right]_{\mathrm{OU}} \mathrm{d}\tau \Bigg\} \cdot \nabla_x p^{(0)} \, . \end{aligned} \tag{C.32}$$

Thus, in total the FPE (C.21) reads

$$\begin{aligned} \partial_t p^{(0)} = -\Bigg[f_0(\mathbf{x}) + \int_0^\infty \Big\{ &\mathbb{E}\left[(f_1(\mathbf{x},\mathbf{y}) \cdot \nabla_x) f_1(\mathbf{x},\mathbf{y}[\tau])\right]_{\mathrm{OU}} \\ &+ \mathbb{E}\left[\{g_1(\mathbf{x},\mathbf{y}) \cdot \mathsf{D}^{-1}\mathbf{y}\} f_1(\mathbf{x},\mathbf{y}[\tau])\right]_{\mathrm{OU}} \\ &- \mathbb{E}\left[\{\nabla_y \cdot g_1(\mathbf{x},\mathbf{y})\} f_1(\mathbf{x},\mathbf{y}[\tau])\right]_{\mathrm{OU}} \Big\} \mathrm{d}\tau \Bigg] \cdot \nabla_x p^{(0)} \\ &- \int_0^\infty \mathbb{E}\left[f_1(\mathbf{x},\mathbf{y}) \otimes f_1(\mathbf{x},\mathbf{y}[\tau])\right]_{\mathrm{OU}} \mathrm{d}\tau : \nabla_x \nabla_x p^{(0)} \, . \end{aligned} \tag{C.33}$$

C.3 Cholesky-Decomposition

The following proof is based on Pavliotis and Stuart (2008). First we write the last term in (6.32) as

$$\begin{aligned}\int_0^\infty \langle f_1(\mathbf{x},\mathbf{y})\otimes f_1[\mathbf{x},\mathbf{y}(\tau)]\rangle_{\mathrm{OU}}\mathrm{d}\tau : \nabla_x\nabla_x p^{(0)}&\\ &= \int p_s(\mathbf{y}) f_1(\mathbf{x},\mathbf{y}) \otimes L_1^{-1} f_1(\mathbf{x},\mathbf{y}) : \nabla_x\nabla_x p^{(0)}\mathrm{d}^F\mathbf{y} && \text{(C.34)}\\ &= \int p_s(\mathbf{y}) f_1(\mathbf{x},\mathbf{y}) \otimes \Phi(\mathbf{x},\mathbf{y})\mathrm{d}^F\mathbf{y} : \nabla_x\nabla_x p^{(0)} && \text{(C.35)}\\ &= \mathbf{B}_1(\mathbf{x}) : \nabla_x\nabla_x p^{(0)}\,. && \text{(C.36)}\end{aligned}$$

Furthermore, we note that (C.36) is equivalent to

$$\begin{aligned}\mathbf{B}_1(\mathbf{x}) : \nabla_x\nabla_x p^{(0)} &= \frac{1}{2}\left[\mathbf{B}_1(\mathbf{x}) + \mathbf{B}_1(\mathbf{x})^{\mathrm{T}}\right] : \nabla_x\nabla_x p^{(0)}\\ &\equiv \mathbf{B}(\mathbf{x}) : \nabla_x\nabla_x p^{(0)}\,, \qquad \text{(C.37)}\end{aligned}$$

as can be easily proven in component notation, since both indices of the inner matrix product indicate the same derivative of $p^{(0)}$. Obviously, $\mathbf{B} \in \mathbb{R}^{S\times S}$ is symmetric. Thus it remains to be shown that $\mathbf{B}$ is positive semi-definite, i.e. $\forall \zeta \in \mathbb{R}^S$

$$\zeta^{\mathrm{T}}\mathbf{B}\zeta \geq 0\,. \qquad \text{(C.38)}$$

Proof. For simplification we omit in the following some of the dependencies. We have

$$\begin{aligned}\zeta^{\mathrm{T}}\mathbf{B}_1\zeta &= \zeta^{\mathrm{T}}\left[\frac{1}{2}\left(\mathbf{B}_1 + \mathbf{B}_1^{\mathrm{T}}\right) + \frac{1}{2}\left(\mathbf{B}_1 - \mathbf{B}_1^{\mathrm{T}}\right)\right]\zeta\\ &= \zeta^{\mathrm{T}}\mathbf{B}\zeta\,, \qquad \text{(C.39)}\end{aligned}$$

since the latter term vanishes due to its anti-symmetric nature. Inserting the definition of $\mathbf{B}_1$ (C.36) and Φ (C.35) in (C.39) yields

$$\begin{aligned}\zeta^{\mathrm{T}}\mathbf{B}\zeta &= \int p_s(\mathbf{y})\zeta^{\mathrm{T}} f_1(\mathbf{x},\mathbf{y}) \otimes \Phi(\mathbf{x},\mathbf{y})\zeta \mathrm{d}^F\mathbf{y} \\ &= \int p_s(\mathbf{y})\zeta_i f_{1i}(\mathbf{x},\mathbf{y})\Phi_j(\mathbf{x},\mathbf{y})\zeta_j \mathrm{d}^F\mathbf{y} \\ &= \int p_s(\mathbf{y})\zeta_i [L_1\Phi_i(\mathbf{x},\mathbf{y})]\Phi_j(\mathbf{x},\mathbf{y})\zeta_j \mathrm{d}^F\mathbf{y}\,. \end{aligned} \tag{C.40}$$

This can be simplified to

$$\zeta^{\mathrm{T}}\mathbf{B}\zeta = \int p_s(\mathbf{y})[L_1\phi_i(\mathbf{x},\mathbf{y})]\phi_j(\mathbf{x},\mathbf{y})\mathrm{d}^F\mathbf{y}\,, \tag{C.41}$$

with $\phi = \zeta_i\Phi_i = \zeta \cdot \Phi$. The adjoint operator of L_1 (6.16) reads

$$L_1^\dagger \bullet = \nabla_y \cdot (g_2 \bullet) - \frac{1}{2}\nabla_y \cdot \nabla_y \cdot (\mathbf{\Sigma}\bullet) \tag{C.42}$$

and has a corresponding backward FPE given by

$$\partial_t p = L_1^\dagger p \tag{C.43}$$

(Gardiner 2009). This implies for the stationary PDF p_s

$$0 = \partial_t p_s = L_1^\dagger p_s\,. \tag{C.44}$$

Let $f(\mathbf{x},\mathbf{y})$ be an arbitrary, sufficiently differentiable, scalar field. Then

$$\begin{aligned} L_1^\dagger(p_s f) &= \nabla_y \cdot (g_2 p_s f) - \frac{1}{2}\nabla_y \cdot \nabla_y \cdot (\mathbf{\Sigma} p_s f) \\ &= [\nabla_y \cdot (g_2 p_s)]\, f + g_2 p_s \cdot \nabla_y f - \frac{1}{2}\Big[\partial_{y_j}\partial_{y_i}(\mathbf{\Sigma}_{ij}p_s) f + \mathbf{\Sigma}_{ij} p_s \partial_{y_j}\partial_{y_i} f \\ &\quad + \partial_{y_j}(\mathbf{\Sigma}_{ij}p_s)\partial_{y_i} f + \partial_{y_i}(\mathbf{\Sigma}_{ij}p_s)\partial_{y_j} f\Big]\,. \end{aligned} \tag{C.45}$$

Because of the diagonal form of $\mathbf{\Sigma}$ the last two terms can be summarized to

$$\begin{aligned} L_1^\dagger(p_s f) = \left(L_1^\dagger p_s\right) f - p_s \left[-g_2 p_s \cdot \nabla_y f - \frac{1}{2}\mathbf{\Sigma} : \nabla_y \nabla_y f\right] - p_s \mathbf{\Sigma} : \nabla_y \nabla_y f \\ - p_s \nabla_y \cdot \mathbf{\Sigma} \cdot \nabla_y f - (\nabla_y p_s)^{\mathrm{T}} \mathbf{\Sigma} \nabla_y f \,. \end{aligned} \tag{C.46}$$

According to (C.44) the first term vanishes and we can simplify (C.46) to

$$L_1^\dagger(p_s f) = -p_s L_1 f - p_s \mathbf{\Sigma} : \nabla_y \nabla_y f - p_s \nabla_y \cdot \mathbf{\Sigma} \cdot \nabla_y f - (\nabla_y p_s)^{\mathrm{T}} \mathbf{\Sigma} \nabla_y f \,. \tag{C.47}$$

Let $h(\mathbf{x}, \mathbf{y})$ be another arbitrary, sufficiently differentiable scalar field. Then

$$\begin{aligned} \int p_s (L_1 h) f \mathrm{d}^F \mathbf{y} &= \int h (L_1^\dagger p_s f) d^F \mathbf{y} \\ &= - \int h \left[p_s L_1 f + p_s \mathbf{\Sigma} : \nabla_y \nabla_y f \right. \\ &\quad \left. + p_s (\nabla_y \cdot \mathbf{\Sigma}) \cdot \nabla_y f + (\nabla_y p_s)^{\mathrm{T}} \mathbf{\Sigma} \nabla_y f\right] \mathrm{d}^F \mathbf{y} \,. \end{aligned} \tag{C.48}$$

Partial integration of the last integral yields

$$\begin{aligned} \int p_s (L_1 h) f \mathrm{d}^F \mathbf{y} &= - \int h p_s \left[L_1 f + \mathbf{\Sigma} : \nabla_y \nabla_y f + (\nabla_y \cdot \mathbf{\Sigma}) \cdot \nabla_y f\right] \mathrm{d}^F \mathbf{y} \\ &\quad + \int p_s \left[(\nabla_y h)^{\mathrm{T}} \mathbf{\Sigma} \nabla_y f + h \mathbf{\Sigma} : \nabla_y \nabla_y f + h (\nabla_y \cdot \mathbf{\Sigma}) \cdot \nabla_y f\right] \mathrm{d}^F \mathbf{y} \\ &= - \int p_s \left[h L_1 f - (\nabla_y h)^{\mathrm{T}} \mathbf{\Sigma} \nabla_y f\right] \mathrm{d}^F \mathbf{y} \,. \end{aligned} \tag{C.49}$$

Finally let $h = f = \phi$. Then we have

$$\int p_s (L_1 \phi) \phi \mathrm{d}^F \mathbf{y} = \frac{1}{2} \int p_s (\nabla_y \phi)^{\mathrm{T}} \mathbf{\Sigma} \nabla_y \phi \mathrm{d}^F \mathbf{y} \tag{C.50}$$

$$= \frac{1}{2} \int p_s (\nabla_y \phi)^{\mathrm{T}} \boldsymbol{\sigma}^{\star y} (\boldsymbol{\sigma}^{\star y})^{\mathrm{T}} \nabla_y \phi \mathrm{d}^F \mathbf{y} \tag{C.51}$$

$$= \frac{1}{2} \int p_s \left\|(\boldsymbol{\sigma}^{\star y})^{\mathrm{T}} \nabla_y \phi\right\|^2 \mathrm{d}^F \mathbf{y} \geq 0 \tag{C.52}$$

□

Appendix D

Total Energy Norm

The state vector of the QG3LM is defined by

$$\mathbf{x} = \begin{pmatrix} {}_{\nu}x^m_{n,1} \\ {}_{\nu}x^m_{n,2} \\ {}_{\nu}x^m_{n,3} \end{pmatrix} \equiv \begin{pmatrix} {}_{\nu}\psi^m_{n,i=1} \\ {}_{\nu}\psi^m_{n,i=2} \\ {}_{\nu}\psi^m_{n,i=3} \end{pmatrix} , \tag{D.1}$$

where ${}_{\nu}\psi^m_{n,i}$ is the spectral coefficient of the streamfunction, m is the zonal wavenumber, n is the total wavenumber, and $\nu = 1$ ($\nu = 2$) denotes the real (imaginary) part of the coefficient. The boundary conditions of the QG3LM lead to trivial components for $m = n = 0$ and vanishing imaginary components for $m = 0 \wedge n \geq 1$ (Ehrendorfer 2000). Therefore (D.1) reduces to

$$\mathbf{x} = \begin{pmatrix} x_1 \\ x_2 \\ \vdots \\ x_N \end{pmatrix} \equiv \begin{pmatrix} {}_1\psi^0_{1,1} \\ {}_1\psi^0_{1,2} \\ \vdots \\ {}_2\psi^{21}_{21,3} \end{pmatrix} , \tag{D.2}$$

because the QG3LM uses a spectral truncation of T21 (Marshall and Molteni 1993). From this Ehrendorfer (2000) defines the total energy norm as

$$\mathsf{M} = \begin{pmatrix} \widehat{\mathsf{M}}_{0,1} & & & 0 \\ & \widehat{\mathsf{M}}_{0,2} & & \\ & & \ddots & \\ 0 & & & \widehat{\mathsf{M}}_{21,21} \end{pmatrix}, \tag{D.3}$$

where the matrices on the diagonal are given by

$$\widehat{\mathsf{M}}_{m,n} = \frac{\delta_m}{3} \begin{pmatrix} n(n+1) + a^2 R_1^{-2} & -a^2 R_1^{-2} & 0 \\ -a^2 R_1^{-2} & n(n+1) + a^2 R_1^{-2} + a^2 R_2^{-2} & -a^2 R_2^{-2} \\ 0 & -a^2 R_2^{-2} & n(n+1) + a^2 R_2^{-2} \end{pmatrix}. \tag{D.4}$$

Here $\delta_m = 0.5$ for $m = 0$ and equal 1 else, $a = 6370\,\text{km}$ denotes Earth's radius, and $R_1^{-2} = 700\,\text{km}$ ($R_2^{-2} = 450\,\text{km}$) is the Rossby radius of deformation of the $200 - 500\,\text{hPa}$ ($500 - 800\,\text{hPa}$) layer. In combination with the state vector (D.2) this implies that

$$E = \mathbf{x}^{\mathrm{T}} \mathsf{M} \mathbf{x}\,, \tag{D.5}$$

is the total energy of the flow.

Appendix E

Explicit EOF Coefficients

This chapter is based on Keeß (2010). In general the QG3LM (3.1a) can be written as

$$\frac{\mathrm{d}\Psi_i}{\mathrm{d}t} = \tilde{F}_i + \tilde{\mathbf{L}}_{ij}\Psi_j + \tilde{\mathbf{N}}_{ijk}\Psi_j\Psi_k\,. \tag{E.1}$$

Applying the EOF transformation (3.5) results in

$$\Psi_i(t) = \mathbf{E}_{ij}a_j(t) + \langle\Psi_i\rangle\,, \tag{E.2}$$

where we neglected the energy metric for convenience. The time derivative of (E.2) yields

$$\frac{\mathrm{d}\Psi}{\mathrm{d}t} = \frac{\mathrm{d}}{\mathrm{d}t}\left[\mathbf{E}\mathbf{a} + \langle\Psi\rangle\right] = \mathbf{E}\frac{\mathrm{d}\mathbf{a}}{\mathrm{d}t} \tag{E.3}$$

so that (E.1) becomes

$$\mathbf{E}_{il}\frac{\mathrm{d}a_l}{\mathrm{d}t} = \tilde{F}_i + \tilde{\mathbf{L}}_{ij}\left[\mathbf{E}_{jl}a_l + \langle\Psi_j\rangle\right] + \tilde{\mathbf{N}}_{ijk}\left[\mathbf{E}_{jm}a_m + \langle\Psi_j\rangle\right]\left[\mathbf{E}_{kn}a_n + \langle\Psi_k\rangle\right]\,. \tag{E.4}$$

Thus,

$$\frac{\mathrm{d}a_l}{\mathrm{d}t} = \mathsf{E}_{li}^{-1}\left[\tilde{F}_i + \tilde{\mathsf{L}}_{ij}\langle\Psi_j\rangle + \tilde{\mathsf{N}}_{ijk}\langle\Psi_j\rangle\langle\Psi_k\rangle\right] \tag{E.5}$$

$$+\,\mathsf{E}_{li}^{-1}\left[\tilde{\mathsf{L}}_{ij}\mathsf{E}_{jl} + \left(\tilde{\mathsf{N}}_{ijk} + \tilde{\mathsf{N}}_{ikj}\right)\mathsf{E}_{jl}\langle\Psi_k\rangle\right]a_l + \mathsf{E}_{li}^{-1}\tilde{\mathsf{N}}_{ijk}\mathsf{E}_{jm}\mathsf{E}_{kn}a_m a_n$$

$$\equiv F_l + \mathsf{L}_{lm}a_m + \mathsf{N}^*_{lmn}a_m a_n\,. \tag{E.6}$$

In order to obtain the explicit EOF coefficients $\mathbf{F}, \mathsf{L}$, and N^* we calculate the tendency of the model for various $\mathbf{a}$. In particular, we consider the following

1.) Let $\mathbf{a} = 0$. Then (E.6) reduces to

$$\frac{\mathrm{d}a_l}{\mathrm{d}t} = F_l\,. \tag{E.7}$$

2.) Consider two principle component vectors $\mathbf{a}^1 = \delta_{mi}\mathbf{e}_i$ and $\mathbf{a}^2 = 2\delta_{mi}\mathbf{e}_i$, indicated by the superscript. Inserting both into (E.6) yields two equations

$$\frac{\mathrm{d}a_l^1}{\mathrm{d}t} = F_l + \mathsf{L}_{lm} + \mathsf{N}^*_{lmm} \tag{E.8a}$$

$$\frac{\mathrm{d}a_l^2}{\mathrm{d}t} = F_l + 2\mathsf{L}_{lm} + 4\mathsf{N}^*_{lmm}\,. \tag{E.8b}$$

From this we obtain, after some algebra,

$$\mathsf{L}_{lm} = \frac{1}{2}\left[4\frac{\mathrm{d}a_l^1}{\mathrm{d}t} - \frac{\mathrm{d}a_l^2}{\mathrm{d}t} - 3F_l\right] \tag{E.9a}$$

$$\mathsf{N}^*_{lmm} = \frac{\mathrm{d}a_l^1}{\mathrm{d}t} - F_l - \mathsf{L}_{lm}\,. \tag{E.9b}$$

3.) Consider an arbitrary vector with $\mathbf{a} \neq 0$. Then results from (E.6)

$$\frac{\mathrm{d}a_l}{\mathrm{d}t} = F_l + \mathsf{L}_{lm}a_m + \mathsf{L}_{ln}a_n + \mathsf{N}^*_{lmm}a_m a_m + \mathsf{N}^*_{lnn}a_n a_n$$

$$+\,\mathsf{N}^*_{lmn}a_m a_n + \mathsf{N}^*_{lmn}a_n a_m \tag{E.10}$$

$$= F_l + \mathsf{L}_{lm}a_m + \mathsf{L}_{ln}a_n + \mathsf{N}^*_{lmm}a_m a_m + \mathsf{N}^*_{lnn}a_n a_n$$

$$+\left(\mathsf{N}^*_{lmn} + \mathsf{N}^*_{lnm}\right)a_m a_n\,, \tag{E.11}$$

because of symmetry we have

$$\mathsf{N}^*_{lmn} a_m a_n = \mathsf{N}^*_{lnm} a_n a_m \,. \tag{E.12}$$

Let $\mathbf{a} = \mathbf{e}_m + 2\mathbf{e}_n$. Then follows from (E.11)

$$\mathsf{N}_{lmn} = \frac{1}{2}\left[\frac{\mathrm{d}a_l}{\mathrm{d}t} - F_l - \mathsf{L}_{lm} - 2\mathsf{L}_{ln} - \mathsf{N}^*_{lmm} - 4\mathsf{N}^*_{lnn}\right] , \tag{E.13}$$

where

$$\mathsf{N}_{lmn} = \begin{cases} 0, & m > n \\ \mathsf{N}^*_{lmm}, & m = n \\ \mathsf{N}^*_{lmn} + \mathsf{N}^*_{lnm}, & \text{else.} \end{cases} \tag{E.14}$$

Bibliography

Abramov, R. V., and A. J. Majda. 2007. Blended response algorithms for linear fluctuation-dissipation for complex nonlinear dynamical systems. *Nonlinearity* 20 (12): 2793–2821. doi:`10.1088/0951-7715/20/12/004`.

———. 2008. New Approximations and Tests of Linear Fluctuation-Response for Chaotic Nonlinear Forced-Dissipative Dynamical Systems. *Journal of Nonlinear Science* 18 (3): 303–341. doi:`10.1007/s00332-007-9011-9`.

———. 2009. A New Algorithm for Low-Frequency Climate Response. *J. Atmos. Sci.* 66 (2): 286–309. doi:`10.1175/2008JAS2813.1`.

Achatz, U., and G. Branstator. 1999. A Two-Layer Model with Empirical Linear Corrections and Reduced Order for Studies of Internal Climate Variability. *J. Atmos. Sci.* 56 (17): 3140–3160. doi:`10.1175/1520-0469(1999)056<3140:ATLMWE>2.0.CO;2`.

Achatz, U., U. Löbl, S. I. Dolaptchiev, and A. Gritsun. 2013. Fluctuation-Dissipation Supplemented by Nonlinearity: A Climate-Dependent Subgrid-Scale Parameterization in Low-Order Climate Models. *J. Atmos. Sci.* 70 (6): 1833–1846. doi:`10.1175/JAS-D-12-0229.1`.

Achatz, U., and J. D. Opsteegh. 2003a. Primitive-Equation-Based Low-Order Models with Seasonal Cycle. Part I: Model Construction. *J. Atmos. Sci.* 60 (3): 465–477. doi:`10.1175/1520-0469(2003)060<0465:PEBLOM>2.0.CO;2`.

Achatz, U., and J. D. Opsteegh. 2003b. Primitive-Equation-Based Low-Order Models with Seasonal Cycle. Part II: Application to Complexity and Nonlinearity of Large-Scale Atmosphere Dynamics. *J. Atmos. Sci.* 60 (3): 478–490. doi:`10.1175/1520-0469(2003)060<0478:PEBLOM>2.0.CO;2`.

Baiesi, M., and C. Maes. 2013. An update on the nonequilibrium linear response. *New Journal of Physics* 15 (1): 013004. doi:`10.1088/1367-2630/15/1/013004`.

Bell, T. L. 1980. Climate Sensitivity from Fluctuation Dissipation: Some Simple Model Tests. *J. Atmos. Sci.* 37 (8): 1700–1707. doi:`10.1175/1520-0469(1980)037<1700:CSFFDS>2.0.CO;2`.

Branstator, G., and S. E. Haupt. 1998. An Empirical Model of Barotropic Atmospheric Dynamics and Its Response to Tropical Forcing. *J. Climate* 11 (10): 2645–2667. doi:`10.1175/1520-0442(1998)011<2645:AEMOBA>2.0.CO;2`.

Chu, K. E. 1989. Symmetric Solutions of Linear Matrix Equations by Matrix Decompositions. *Linear Algebra and Its Applications* 119 (C): 35–50. doi:`10.1016/0024-3795(89)90067-0`.

Cooper, F. C., and P. H. Haynes. 2011. Climate Sensitivity via a Nonparametric Fluctuation-Dissipation Theorem. *J. Atmos. Sci.* 68 (5): 937–953. doi:`10.1175/2010JAS3633.1`.

Demaeyer, J., and S. Vannitsem. 2017. Stochastic parametrization of subgrid-scale processes in coupled ocean-atmosphere systems: benefits and limitations of response theory. *Quart. J. Roy. Meteor. Soc.* 143 (703): 881–896. doi:`10.1002/qj.2973`.

———. 2018. Comparison of stochastic parameterizations in the framework of a coupled ocean–atmosphere model. *Nonlinear Processes in Geophysics* 25 (3): 605–631. doi:`10.5194/npg-25-605-2018`.

Dolaptchiev, S. I., U. Achatz, and I. Timofeyev. 2013a. Stochastic closure for local averages in the finite-difference discretization of the forced Burgers equation. *Theoretical and Computational Fluid Dynamics* 27 (3-4): 297–317. doi:`10.1007/s00162-012-0270-1`.

Dolaptchiev, S. I., I. Timofeyev, and U. Achatz. 2013b. Subgrid-scale closure for the inviscid Burgers-Hopf equation. *Communications in Mathematical Sciences* 11 (3): 757–777. doi:`10.4310/CMS.2013.v11.n3.a5`.

Doms, G., J. Förstner, E. Heise, H.-J. Herzog, D. Mironov, M Raschendorfer, T. Reinhardt, B. Ritter, R. Schrodin, J.-P. Schulz, and G. Vogel. 2011. *Consortium for Small-Scale Modelling A Description of the Nonhydrostatic Regional COSMO Model Part II : Physical Parameterization.* Technical report. Offenbach am Main: Deutscher Wetterdienst.

Ehrendorfer, M. 2000. The Total Energy Norm in a Quasigeostrophic Model. *J. Atmos. Sci.* 57 (20): 3443–3451. doi:`10.1175/1520-0469(2000)057<3443:NACTEN>2.0.CO;2`.

Einstein, A. 1905. Über die von der molekularkinetischen Theorie der Wärme geforderte Bewegung von in ruhenden Flüssigkeiten suspendierten Teilchen. *Annalen der Physik* 322 (8): 549–560. doi:`10.1002/andp.19053220806`.

Field, C. B., V. R. Barros, K. J. Mach, M. D. Mastrandrea, M. van Aalst, W. N. Adger, D. J. Arent, J. Barnett, R. Betts, T. E. Bilir, J. Birkmann, J. Carmin, D. D. Chadee, A. J. Challinor, M. Chatterjee, W. Cramer, D. J. Davidson, Y. O. Estrada, J.-P. Gattuso, Y. Hijioka, O. Hoegh-Guldberg, H. Q. Huang, G. E. Insarov, R. N. Jones, R. S. Kovats, P. Romero-Lankao, J. N. Larsen, I. J. Losada, J. A. Marengo, R. F. McLean, L. O. Mearns, R. Mechler, J. F. Morton, I. Niang, T. Oki, J. M. Olwoch, M. Opondo, E. S. Poloczanska, H.-O. Pörtner, M. H. Redsteer, A. Reisinger, A. Revi, D. N. Schmidt, M. R. Shaw, W. Solecki, D. A. Stone, J. M. R. Stone, K. M. Strzepek, A. G. Suarez, P. Tschakert, R. Valentini, S. Vicuña, A. Villamizar, K. E. Vincent, R. Warren, L. L. White, T. J. Wilbanks, P. P. Wong, and G. W. Yohe. 2014. Technical summary. In *Climate Change 2014: Impacts, Adaptation, and Vulnerability. Part A: Global and Sectoral Aspects. Contribution of Working Group II to the Fifth*

Assessment Report of the Intergovernmental Panel on Climate Change, edited by C. B. Field, V. R. Barros, D. J. Dokken, K. J. Mach, M. D. Mastrandrea, T. E. Bilir, M. Chatterjee, K. L. Ebi, Y. O. Estrada, R. C. Genova, B. Girma, E. S. Kissel, A. N. Levy, S. MacCracken, P. R. Mastrandrea, and L. L. White, 35–94. Cambridge, United Kingdom and New York, NY, USA: Cambridge University Press.

Flato, G., J. Marotzke, B. Abiodun, P. Braconnot, S. C. Chou, W. Collins, P. Cox, F. Driouech, S. Emori, V. Eyring, C. Forest, P. Gleckler, E. Guilyardi, C. Jakob, V. Kattsov, Reason C., and M. Rummukainen. 2013. Evaluation of Climate Models. In *Climate Change 2013: The Physical Science Basis. Contribution of Working Group I to the Fifth Assessment Report of the Intergovernmental Panel on Climate Change,* edited by T. F. Stocker, D. Qin, G.-K. Plattner, M. Tignor, S. K. Allen, J. Boschung, A. Nauels, Y. Xia, V. Bex, and P. M. Midgley. Cambridge, United Kingdom and New York, NY, USA: Cambridge University Press.

Franzke, C. 2013. Predictions of critical transitions with non-stationary reduced order models. *Physica D* 262:35–47. doi:`10.1016/j.physd.2013.07.013`.

Franzke, C., and A. J. Majda. 2006. Low-Order Stochastic Mode Reduction for a Prototype Atmospheric GCM. *J. Atmos. Sci.* 63 (2): 457–479. doi:`10.1175/JAS3633.1`.

Franzke, C., A. J. Majda, and E. Vanden-Eijnden. 2005. Low-Order Stochastic Mode Reduction for a Realistic Barotropic Model Climate. *J. Atmos. Sci.* 62 (6): 1722–1745. doi:`10.1175/JAS3438.1`.

Fuchs, D., S. Sherwood, and D. Hernandez. 2015. An Exploration of Multivariate Fluctuation Dissipation Operators and Their Response to Sea Surface Temperature Perturbations. *J. Atmos. Sci.* 72 (1): 472–486. doi:`10.1175/JAS-D-14-0077.1`.

Gardiner, C. W. 2009. *Stochastic Methods.* Springer.

Gershgorin, B., and A. J. Majda. 2010. A test model for fluctuation-dissipation theorems with time-periodic statistics. *Physica D* 239 (17): 1741–1757. doi:`10.1016/j.physd.2010.05.009`.

Gottwald, G. A., J. P. Wormell, and J. Wouters. 2016. On spurious detection of linear response and misuse of the fluctuation-dissipation theorem in finite time series. *Physica D* 331:89–101. doi:`10.1016/j.physd.2016.05.010`.

Gritsoun, A. S., and V. P. Dymnikov. 1999. Barotropic atmosphere response to small external action: Theory and numerical experiments. *Izvestiya, Atmospheric and Oceanic Physics* 35 (5): 511–525.

Gritsun, A. 2010. Construction of Response Operators to Small External Forcings for Atmospheric General Circulation Models with Time Periodic Right-Hand Sides. *Izvestiya, Atmospheric and Oceanic Physics* 46 (6): 748–756. doi:`10.1134/S000143381006006X`.

Gritsun, A., and G. Branstator. 2007. Climate Response Using a Three-Dimensional Operator Based on the Fluctuation-Dissipation Theorem. *J. Atmos. Sci.* 64 (7): 2558–2575. doi:`10.1175/JAS3943.1`.

———. 2016. Numerical aspects of applying the fluctuation dissipation theorem to study climate system sensitivity to external forcings. *Russian Journal of Numerical Analysis and Mathematical Modelling* 31 (6): 339–354. doi:`10.1515/rnam-2016-0032`.

Gritsun, A., G. Branstator, and A. Majda. 2008. Climate Response of Linear and Quadratic Functionals Using the Fluctuation-Dissipation Theorem. *J. Atmos. Sci.* 65 (9): 2824–2841. doi:`10.1175/2007JAS2496.1`.

Gritsun, A., and V. Lucarini. 2017. Fluctuations, Response, and Resonances in a Simple Atmospheric Model. *Physica D* 349:62–76. doi:`10.1016/j.physd.2017.02.015`.

Hassanzadeh, P., and Z. Kuang. 2016. The Linear Response Function of an Idealized Atmosphere. Part II: Implications for the Practical Use of the Fluctuation-Dissipation Theorem and the Role of Operator's Nonnormality. *J. Atmos. Sci.* 73 (9): 3441–3452. doi:`10.1175/JAS-D-16-0099.1`.

Hines, C. O. 1997. Doppler-spread parameterization of gravity-wave momentum deposition in the middle atmosphere. Part 1: Basic formulation. *Journal of Atmospheric and Solar-Terrestrial Physics* 59 (4): 371–386. doi:`10.1016/S1364-6826(96)00079-X`.

Honerkamp, J. 1994. *Stochastic dynamical systems: concepts, numerical methods, data analysis.* Wiley-VCH.

Keeß, U. 2010. Anomalie-Experimente mit einem reduzierten barotropen Klimamodell. Diplomarbeit, Goethe Universität Frankfurt/Main.

Kirk-Davidoff, D. 2008. On the diagnosis of climate sensitivity using observations of fluctuations. *Atmospheric Chemistry and Physics Discussions* 8 (3): 12409–12434. doi:`10.5194/acpd-8-12409-2008`.

Leith, C. E. 1975. Climate Response and Fluctuation Dissipation. *J. Atmos. Sci.* 32 (10): 2022–2026. doi:`10.1175/1520-0469(1975)032<2022:CRAFD>2.0.CO;2`.

———. 1978. Predictability of climate. *Nature* 276 (5686): 352–355. doi:`10.1038/276352a0`.

Liu, Q., and T. Opsteegh. 1995. Interannual and decadal variations of blocking activity in a quasi-geostrophic model. *Tellus A* 47 (5): 941–954. doi:`10.1034/j.1600-0870.1995.00202.x`.

Lorenz, D. J., and E. T. DeWeaver. 2007. Tropopause height and zonal wind response to global warming in the IPCC scenario integrations. *Journal of Geophysical Research Atmospheres* 112 (10): 1–11. doi:`10.1029/2006JD008087`.

Lucarini, V., and S. Sarno. 2011. A statistical mechanical approach for the computation of the climatic response to general forcings. *Nonlinear Processes in Geophysics* 18 (1): 7–28. doi:`10.5194/npg-18-7-2011`.

Lutsko, N. J., I. M. Held, and P. Zurita-Gotor. 2015. Applying the Fluctuation-Dissipation Theorem to a Two-Layer Model of Quasigeostrophic Turbulence. *J. Atmos. Sci.* 72 (8): 3161–3177. doi:`10.1175/JAS-D-14-0356.1`.

Majda, A. J., R. V. Abramov, and M. J. Grote. 2005. *Information Theory and Stochastics for Multiscale Nonlinear Systems.* 25:133. CRM Monograph Series. American Mathematical Society.

Majda, A. J., I. Timofeyev, and E. Vanden-Eijnden. 2001. A Mathematical Framework for Stochastic Climate Models. *Communications on Pure and Applied Mathematics* 54 (8): 891–974. doi:`10.1002/cpa.1014`.

———. 2002. A priori tests of a stochastic mode reduction strategy. *Physica D* 170 (3-4): 206–252. doi:`10.1016/S0167-2789(02)00578-X`.

———. 2003. Systematic Strategies for Stochastic Mode Reduction in Climate. *J. Atmos. Sci.* 60 (14): 1705–1722. doi:`10.1175/1520-0469(2003)060<1705:SSFSMR>2.0.CO;2`.

Majda, A. J., and X. Wang. 2010. Linear response theory for statistical ensembles in complex systems with time-periodic forcing. *Communications in Mathematical Sciences* 8 (1): 145–172. doi:`10.4310/CMS.2010.v8.n1.a8`.

Marconi, U. M. B., A. Puglisi, L. Rondoni, and A. Vulpiani. 2008. Fluctuation-dissipation: Response theory in statistical physics. *Physics Reports* 461 (4-6): 111–195. doi:`10.1016/j.physrep.2008.02.002`.

Marshall, J., and F. Molteni. 1993. Toward a Dynamical Understanding of Planetary-Scale Flow Regimes. *J. Atmos. Sci.* 50 (12): 1792–1818. doi:`10.1175/1520-0469(1993)050<1792:TADUOP>2.0.CO;2`.

Mauritsen, T., B. Stevens, E. Roeckner, T. Crueger, M. Esch, M. Giorgetta, H. Haak, J. Jungclaus, D. Klocke, D. Matei, U. Mikolajewicz, D. Notz, R. Pincus, H. Schmidt, and L. Tomassini. 2012. Tuning the climate of a global model. *Journal of Advances in Modeling Earth Systems* 4 (3): M00A01. doi:`10.1029/2012MS000154`.

North, G. R., R. E. Bell, and J. W. Hardin. 1993. Fluctuation dissipation in a general circulation model. *Climate Dyn.* 8 (6): 259–264. doi:`10.1007/BF00209665`.

Papanicolaou, G. C. 1976. Some probabilistic problems and methods in singular perturbations. *Rocky Mountain Journal of Mathematics* 6 (4): 653–674.

Pavliotis, G., and A. Stuart. 2008. *Multiscale Methods.* Springer New York.

Peixoto, J. P., and A. H. Oort. 1992. *Physics of Climate.* Springer-Verlag.

Pieroth, M., S. I. Dolaptchiev, M. Zacharuk, T. Heppelmann, A. Gritsun, and U. Achatz. 2018. Climate Dependence in Empirical Parameters of Subgrid-Scale Parameterizations using the Fluctuation-Dissipation Theorem. *J. Atmos. Sci.* 75 (11): 3843–3860. doi:`10.1175/JAS-D-18-0022.1`.

Preisendorfer, R. W. 1988. *Principal component analysis in meteorology and oceanography.* Elsevier.

Ragone, F., V. Lucarini, and F. Lunkeit. 2016. A new framework for climate sensitivity and prediction: a modelling perspective. *Climate Dyn.* 46 (5-6): 1459–1471. doi:`10.1007/s00382-015-2657-3`.

Reinert, D., F. Prill, H. Frank, M. Denhard, and G. Zängl. 2019. *Database Reference Manual for ICON and ICON-EPS.* Technical report. Offenbach am Main: Deutscher Wetterdienst. doi:`10.5676/DWD_pub/nwv`.

Ring, M. J., and R. A. Plumb. 2008. The Response of a Simplified GCM to Axisymmetric Forcings: Applicability of the Fluctuation-Dissipation Theorem. *J. Atmos. Sci.* 65 (12): 3880–3898. doi:`10.1175/2008JAS2773.1`.

Risken, H. 1984. *The fokker-planck equation: methods of solution and applications.* 454. Springer-Verlag.

Rockel, B., and B. Geyer. 2008. The performance of the regional climate model CLM in different climate regions, based on the example of precipitation. *Meteor. Z.* 17 (4): 487–498. doi:`10.1127/0941-2948/2008/0297`.

Schättler, U., G. Doms, and C. Schraff. 2018. *Consortium for Small-Scale Modelling A Description of the Nonhydrostatic Regional COSMO-Model Part VII : User's Guide.* Technical report. Offenbach am Main: Deutscher Wetterdienst.

Schirber, S., E. Manzini, T. Krismer, and M. Giorgetta. 2015. The quasi-biennial oscillation in a warmer climate: sensitivity to different gravity wave parameterizations. *Climate Dyn.* 45 (3-4): 825–836. doi:`10.1007/s00382-014-2314-2`.

Stevens, B., M. Giorgetta, M. Esch, T. Mauritsen, T. Crueger, S. Rast, M. Salzmann, H. Schmidt, J. Bader, K. Block, R. Brokopf, I. Fast, S. Kinne, L. Kornblueh, U. Lohmann, R. Pincus, T. Reichler, and E. Roeckner. 2013. Atmospheric component of the MPI-M earth system model: ECHAM6. *Journal of Advances in Modeling Earth Systems* 5 (2): 146–172. doi:`10.1002/jame.20015`.

Verkley, W. T. M., P. C. Kalverla, and C. A. Severijns. 2016. A maximum entropy approach to the parametrization of subgrid processes in two-dimensional flow. *Quart. J. Roy. Meteor. Soc.* 142 (699): 2273–2283. doi:`10.1002/qj.2817`.

Verkley, W. T. M., and C. A. Severijns. 2014. The maximum entropy principle applied to a dynamical system proposed by Lorenz. *The European Physical Journal B* 87 (1): 7. doi:`10.1140/epjb/e2013-40681-2`.

Wouters, J., S. I. Dolaptchiev, V. Lucarini, and U. Achatz. 2016. Parameterization of stochastic multiscale triads. *Nonlinear Processes in Geophysics* 23 (6): 435–445. doi:`10.5194/npg-23-435-2016`.

Wouters, J., and G. A. Gottwald. 2018. Stochastic model reduction for slow-fast systems with moderate time-scale separation. *arXiv:1804.09537 [cond-mat.stat-mech].* eprint: `arXiv:1804.09537`. `http://arxiv.org/abs/1804.09537`.

———. 2019. Edgeworth expansions for slow–fast systems with finite time-scale separation. *Proceedings of the Royal Society A: Mathematical, Physical and Engineering Sciences* 475 (2223): 20180358. doi:`10.1098/rspa.2018.0358`.

Wouters, J., and V. Lucarini. 2012. Disentangling multi-level systems: averaging, correlations and memory. *Journal of Statistical Mechanics: Theory and Experiment* 2012 (03): P03003. doi:`10.1088/1742-5468/2012/03/P03003`.

Zacharuk, M., S. I. Dolaptchiev, U. Achatz, and I. Timofeyev. 2018. Stochastic subgrid-scale parametrization for one-dimensional shallow-water dynamics using stochastic mode reduction. *Quart. J. Roy. Meteor. Soc.* 144 (715): 1975–1990. doi:`10.1002/qj.3396`.

Zeeman, E C. 1988. Stability of dynamical systems. *Nonlinearity* 1 (1): 115–155. doi:`10.1088/0951-7715/1/1/005`.